The Characterisation of AGATA High Purity Germanium Detectors for Pulse Shape Analysis

Thesis submitted in accordance with the requirements of the University of Liverpool for the degree of Doctor in Philosophy

by

Samantha Jean Colosimo

Oliver Lodge Laboratory

2013

Abstract

Gamma-ray spectroscopy is an essential tool in the study of nuclear phenomenon. The study of exotic nuclei and nuclear states have been used to expand the nuclear chart as well as understand the origin of the universe. Large volume high purity germanium arrays, very high beam intensities and more recently exotic beams have lead to new understanding of nuclear physics. The Advanced Gamma Tracking Array (AGATA) aims to utilise high purity germanium (HPGe) detectors in order to achieve a dramatic increase in efficiency over current spectrometers.

The work detailed in this thesis shows a highly detailed characterisation of two AGATA asymmetric capsules of the same shape in order to test and compare performances. Detector A004 was acceptance tested and scanned at the University of Liverpool in February 2010. Detector A006 was scanned between April and September 2010. Resolution, efficiency and charge collection parameters have been studied, comparing these two detector. The results of the comparison show an excellent agreement between the performance of the two detectors. The depletion rate of the detectors has also been compared quantitatively indicating the dependence of depletion on impurity concentration of the capsules.

An experimental pulse shape database was generated for detector A006. The sensitivity of the detector response was quantified indicating the regions of the detector of high variation in pulse shape response. The *AGATA detector library*, which used to simulate the detector response for pulse shape analysis, is compared with this database. The position resolution achieved between the two data sets has been calculated.

The combination of the detailed comparison and characterisation of the detector with the study of the simulate database will provide the AGATA collaboration with useful information to improve detector simulations in the further for pulse shape analysis.

For my parents, who always believe in me.

It is impossible to enjoy idling thoroughly unless one has plenty of work to do.

- Jerome K. Jerome

Acknowledgements

Sincere thanks to Dr. Andrew Boston, Dr. Helen Boston and Professor Paul Nolan for providing me with the great opportunity to pursue my PhD studies at the University of Liverpool.

I would also like to thank those who read this thesis and offered invaluable feedback, including Dr. Daniel Judson, Dr. Laura Harkness, Dr. Bart Bruyneel and Dr. Andrew Boston.

Thank you to my colleagues within the AGATA collaboration for valuable discussions and the opportunity to learn so much.

Thanks to Dr. John Cresswell and Janet Sampson for computer support throughout my studies. As well, to Tom Stanios and Mark Norman for the help in the lab as well as the comic relief.

Many thanks in particular to Dr. Steven Moon for his hard work and long hours on the detector setup and data acquisition.

Thank you to all my fellow students, past and present, in the Nuclear Physics group for making the past 4 years so much fun. I wouldn't want to leave anyone out by listing names, but in particular, to Liliana Donosa for offering mutual support and joining me for many afternoon coffee trips.

The experience of studying in the UK for the last 4 years has been incredible and full of so many adventures, academic and otherwise. It would not have been possible without the help and support of the many people I have met here who contributed to the experience. To all of my wonderful friends who made me feel at home in the UK, especially Alyssa Drake, Danielle Rostron, Paul Goodall, Laura Nelson, Alex Grint, Heidi Watkins, Suzanne Wong, Dave Eden and Rossella Romita, thank you all for being so funny, brilliant and truly great people.

Thank you to my friends and family in Canada, in Halifax, Toronto and beyond. I always appreciate your encouragement and support from afar. To my professors at Saint Mary's University in Halifax, Nova Scotia, Canada, particularly Dr. Roby Austin, Dr. Adam Sarty and Dr. Gary Welch. Without the

support of the many great instructors during my undergraduate study, I would have never have gotten this far.

To Gerard Turk, I could never put properly into words the encouragement and love that you have given me. You understood what I was going through and helped me all the way, even when I thought I knew better. Thanks for letting me know that all the worries and effort were going to be worth it.

At many times during my PhD I was discouraged and could never imagine actually finishing, however, my family always believed I would be able to accomplish it. To my mother Beverley Colosimo, my father Raymond Colosimo Sr., and my brother Raymond, thank you for constantly believing in and supporting me while I pursue my dreams and ambitions.

Table of Contents

List of Figures

List of Tables

Chapter 1

Introduction

The work presented in this thesis details the characterisation of two AGATA position sensitive high-purity germanium crystals. The first aim is to compare the performance of two detectors in order to verify the similarity of their response. The second part of the analysis details the study of an experimental database compared with an electric field simulation, the AGATA detector library (ADL), in order validate the simulation. A discussion of the ADL simulation is also included.

1.1 Gamma-Ray Spectroscopy

For over 50 years high resolution γ-ray spectroscopy with high purity germanium detectors has been a vital tool in furthering the understanding of nuclear systems and pushing the boundaries of the nuclear chart [1,2]. The behaviour of these many-bodied systems is determined by both microscopic and macroscopic features. Nuclear states are investigated through spectroscopy of de-exciting nuclei. The in-depth study of observables, including excitation energy, isospin, parity and shape, enables an understanding of the nucleus and the nuclear models used to describe it.

1.1.1 High-Purity Germanium Arrays

The most powerful tools currently used for γ-ray spectroscopy are the large hyper-pure germanium (HPGe) escape suppression shielded (ESS) arrays including among others, EUROGAM and EUROBALL in Europe [3,4] and GAMMASPHERE in the United States [5]. These arrays have proven to be invaluable

devices, providing an effective compromise between energy resolution and photopeak efficiency while maintaining a good peak-to-total (P/T) ratio through the utilisation of bismuth germanate (BGO) shields surrounding HPGe detectors, depicted in Fig. 1.1 [6]. High P/T is achieved through the veto of events that undergo incomplete energy deposition.

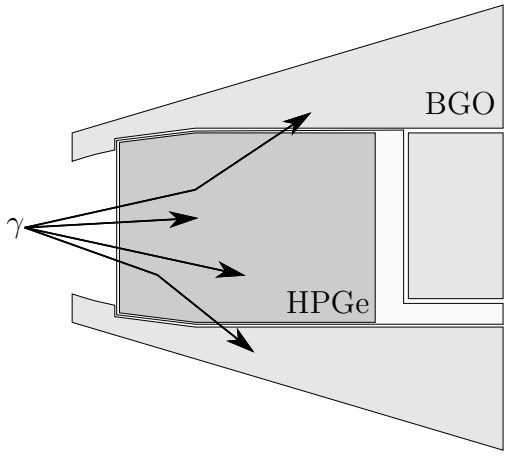

Figure 1.1: HPGe crystal with bismuth germanate shielding, the standard detection unit for large escape suppression arrays. The γ-rays which scatter from the germanium to the BGO shields are vetoed. This detector configuration reduced the background counts, which greatly increases the peak-to-Compton ratio of HPGe detector arrays [7].

This anti-Compton scattering BGO shielding of individual HPGe detectors results in a loss of spatial coverage by HPGe material. This intrinsically limits the efficiency of these types of arrays due to the loss of coverage of detecting material. The development of position sensitive detectors as adopted for the arrays TIGRESS at TRIUMF-ISAC in Vancouver, Canada [8], EXOGAM at Spiral 2, GANIL in Caen, France [9], and Miniball at REX-ISOLDE, CERN in Geneva, Switzerland [10] provides more precise identification of interaction positions (≤ 5 mm) within the detectors. This precision allows for better Doppler correction and therefore better energy resolution. The accuracy of the position determination within these detectors has led to the concept of γ-ray tracking (GRT) in order to recover energy loss through scattering by accurately identifying interaction positions within the detector [11]. The advancement of digital sampling electronics for accurate recording of time and energy signals allows for the development of pulse shape analysis (PSA) and therefore provide excellent efficiency for these arrays.

1.1.2 Radioactive Ion Beam Facilities

The development of radioactive ion beam (RIB) facilities, including RIBF (Japan), TRIUMF-ISAC (Canada), SPIRAL2 (France), HIE-ISOLDE (Switzerland), FAIR (GSI) and SPES (Italy), allows the study of nuclei far from stability [12]. These facilities provide beams with a broad range of exotic proton- and neutron-rich nuclei. Greater experimental challenges including large background, high Doppler broadening and low count rate require more efficient detector arrays. Highly sensitive γ-ray spectroscopy tools are necessary to deal with these challenges. The goal of the next stage of development is to create spectrometers strictly from HPGe material with the goal of identification of interactions within a few millimetre throughout the detectors.

1.2 The AGATA Spectrometer

The AGATA, or Advanced GAmma Tracking Array, will be composed fully of HPGe crystals [13]. A 4π germanium shell provides an angular resolution ideally suited for high energy spectroscopy at recoil velocities up to v/c = 50%. The proposed AGATA ball and the AGATA detection unit, the AGATA triple cluster, are depicted in Fig. 1.2.

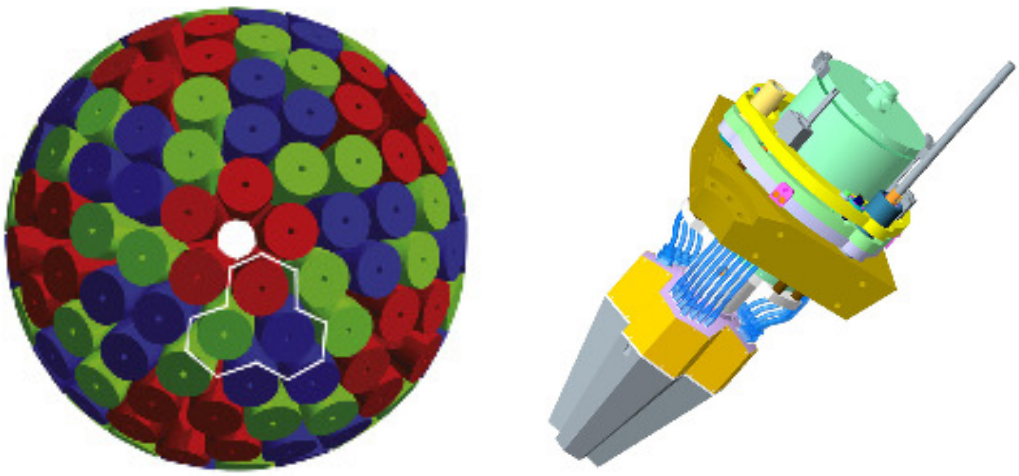

(a) (b)

Figure 1.2: The full 4π AGATA array consisting of 180 AGATA capsules within 60 triple cryostats (right). The AGATA triple cluster is shown on the left. This idealised configuration will achieve solid angular coverage of 82 % [13].

AGATA is currently being developed in Europe in order to address these experimental challenges. The AGATA detection units will consist of triple clusters of three 36 fold segmented HPGe crystals coupled together within one cryostat, depicted in Fig. 1.2(b). The goal of AGATA is to have a full HPGe spectrometer, approaching 4π coverage of detecting material. 60 AGATA triple clusters (ATCs) will form a 180 detector array.

In order to tile properly in a spherical formation, the hexagonal front faces of the AGATA HPGe crystals are asymmetric. Three different shapes of crystals have been developed, referred to as A-type (Red), B-type (Green) and C-type (Blue) as shown in 1.2(a). These detectors only differ in the slightly different hexagonal front faces. The position sensitive detectors will be used to track photon interactions throughout the crystals.

1.2.1 Gamma-Ray Tracking

Gamma-ray tracking utilises highly segmented detectors as well as digital electronics to identify the location and energy of photon interactions within the array illustrated in Fig. 1.3.

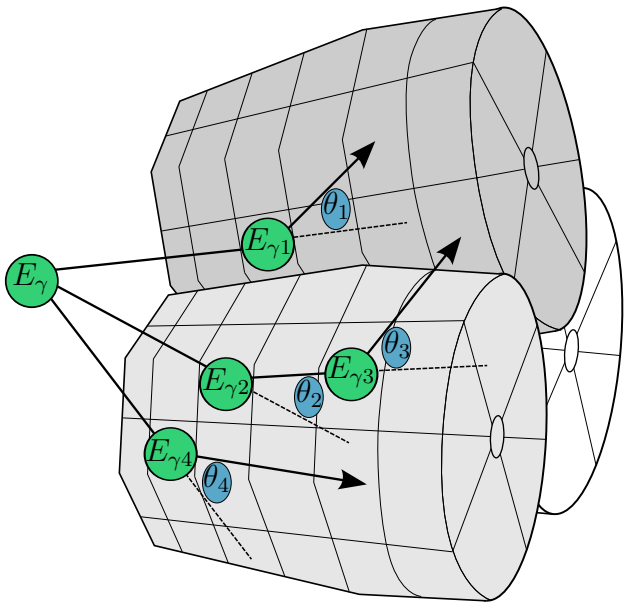

Figure 1.3: An illustration of scattering γ-rays tracked through the a segmented HPGe crystal. The scatters can be summed to calculate the initial full energy of the γ-ray photon. Scattering between adjacent crystals are also reconstructed.

Scattering γ-rays are tracked through the array and reconstructed to calcu-

late the full energy events. The tracked interactions will increase the efficiency and performance of the array far beyond current escape suppressed arrays. The removal of the BGO shielding allows for a greater geometric efficiency and higher performance of these detectors. Several algorithms have been developed by the AGATA collaboration in order to calculate tracks of interactions within the array [14].

The improvement of expected performance of the photopeak efficiency, ϵ_{FEP}, at multiplicities, M_γ, 1 and 30 of the AGATA spectrometer over current arrays is detailed in Table 1.1. Through realistic GEANT4 simulations of the detector, the expected performance of the full array over current large HPGe arrays is given, as well as the performance of the AGATA demonstrator [15].

HPGe Array	# Detectors (crystals)	Granularity	$\epsilon_{\mathrm{FEP}} M_\gamma = 1$ (P/T %)	$\epsilon_{\mathrm{FEP}} M_\gamma = 30$ (P/T %)
EUROBALL III	71 (239)	239	9 (56)	6 (37)
GAMMASPHERE	110 (110)	110	9 (63)	
AGATA 4π	60 (180)	6480	43 (58)	24 (44)
Demonstrator	5 (15)	540	7 (7)	

Table 1.1: A summary of the performance of the most efficient HPGe arrays as well as the expected efficiency and photo peak performance of the AGATA 4π Array and AGATA Demonstrator as calculated by realistic GEANT4 simulations [7, 16, 17].

1.2.2 The AGATA Demonstrator

For the first stage of the AGATA project, the AGATA Demonstrator, Fig. 1.4(a), has been commissioned in order to show the feasibility of the position sensitive γ-ray detection.

Five triple clusters that make up the demonstrator were in use in the array at INFN, Legnaro, Italy which was completed in early 2011. The demonstrator has undertaken several experimental campaigns and been successful in matching the performance of arrays of many more detectors. The HPGe detectors characterised within this work were used within the 5 AGATA triple clusters.

The next phase currently being commissioned is for the AGATA demonstrator to be paired with five 'double clusters' consisting of units of two HPGe crystals mounted within single cryostats at the PRESPEC setup at GSI. The

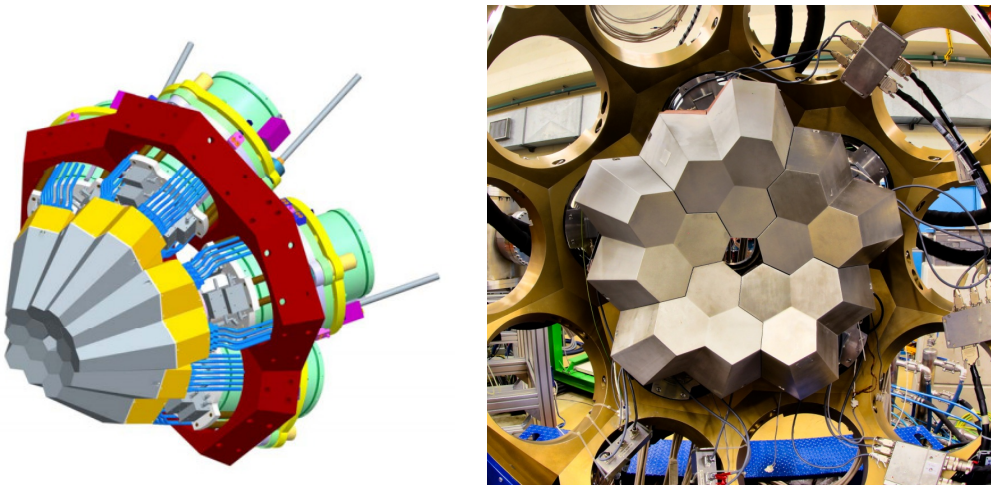

Figure 1.4: The AGATA Demonstrator consisting of 5 triple cluster detectors. 15 HPGe crystal are included in this setup in total.

utility of the AGATA array is that it can be used dynamically within different setups and with the ability to couple with anciliary detectors.

1.3 Pulse Shape Analysis

Gamma-ray tracking reconstructs the paths of γ-ray Compton scattering interactions throughout a segmented HPGe crystal using very accurate energy, position and time information. Initial position information is extracted through the segmentation. Accuracy within a few mm^3 is achieved through pulse shape analysis (PSA), which uses the shape of the charge collecting signal as well as the intensity of the transient signals in neighbouring segments in order to determine the x, y, and z positions [18].

A database of pulse shapes is generated from a simulation of the crystal. These simulations incorporate the physical details of the germanium crystal and apply the signal generation properties in order to generate libraries of pulse shapes which can be compared to the digitally recorded detector signals. In this way, the position of each interaction is identified.

There are several algorithms within the AGATA collaboration that utilise pulse shape databases to identify hit locations. Once the geometric locations of the interactions are identified, gamma-ray tracking can be used.

1.4 Detector Characterisation

The success of tracking arrays such as AGATA depends upon the ability to reconstruct the paths of γ-ray scatters within the germanium detectors. Currently simulated databases of pulses are used within experimental pulse shape analysis.

It is necessary to validate these experimental databases with real pulse shapes generated by the detector. The pulse shape response is determined by the properties of the HPGe crystal, the voltages supplied by the detector as well as the preamplifier characteristics. The process of detector characterisation is performed to a detailed analysis of the response function of the AGATA detectors. Simulated databases of pulse shapes can be validated with experimental data, allowing for improved PSA.

1.5 Aims of this Thesis

The goal of this work is to present the characterisation and study of the AGATA A-type capsules. The first part of this work is to compare directly the response and performance of two AGATA A-type crystals. A study of the operating performance has been undertaken examining the signal response. The performance at reduced bias voltages has been examined in order to study the depletion behaviour of the crystals. In the experimental operation of the AGATA arrays, detector electric field simulations are used to generate pulse shape libraries. The AGATA detector library (ADL) simulation code is introduced and a database of pulses is generated to study the simulation performance. The last part of this thesis is the validation of the ADL simulation with an experimentally generated database of pulse shapes. This work, in combination with other AGATA characterisation work, will aid the understanding of the AGATA asymmetric crystals.

Chapter 2

Principles of γ-Ray Detection

In this chapter the physical processes important to high resolution γ-ray spectroscopy will be described. The production of the charge carriers within the detection medium determines the performance of the detector. The photon interactions discussed below will produce free electrons-hole pairs in γ-ray detectors, which can be collected and transformed into a signal. Basic semiconductor physics as well as signal processing are discussed in Chapter 3. Fundamental to the more complex study of pulse shape analysis are the underlying processes which form the signals of the detector, defined by the structure of the semiconductors as well as the electronics used to generate the detector signal.

2.1 Photon Interactions with Matter

There are several mechanisms in which photon radiation interacts with matter. Photon energy is not degraded but only attenuated as it passes through matter [19]. This attenuation results from the scattering and absorption of the photons and is described by Equation 2.1:

$$I(x) = I_0(x)^{-\mu t} \tag{2.1}$$

where $I_0(x)$ is the incident number of photons, μ is the absorption coefficient characteristic of the material and t is the thickness of the absorber. The absorption coefficient is determined by Equation 2.2:

$$\mu = \Big(\frac{N_A \rho}{A}\Big)\sigma_{TOT} \tag{2.2}$$

where ρ is the material density, N_A is Avogadro's number (6.022 mol^{-1}), A is

the atomic mass and σ_{TOT} is the total cross-section of photon interactions.

In the energy regime of interest, 50 keV - 10 MeV, the dominant mechanisms of interaction are photoelectric absorption, Compton scattering and pair production. The cross sections for each of these interactions determines σ_{TOT},

$$\sigma_{TOT} = \sigma_{PhotoAbsorb} + \sigma_{Compton} + \sigma_{PairProd} \tag{2.3}$$

The relative probabilities of those processes in the energy regime of interest are illustrated in Fig. 2.1.

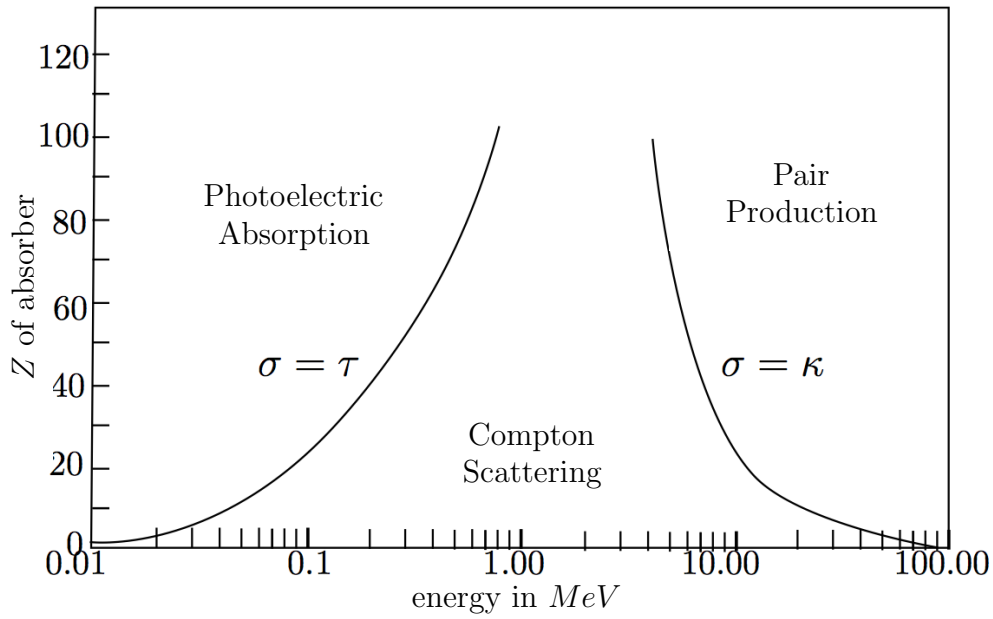

Figure 2.1: The three dominant types of γ-ray interactions. The values $\sigma = \tau$ and $\sigma = \kappa$ lines are for values of Z and energy where each interaction type occurs in equal proportion. Adapted from [20].

The photoelectric absorption process is enhanced in higher Z material. The probability of Compton scattering depends on the number of electrons within a material and therefore increases linearity with Z.

2.1.1 Photoelectric Absorption

Photoelectric absorption is the dominating photon interaction at γ-ray energies below 200 keV. In this process, a photon is absorbed by an atomic electron and the electron is subsequently ejected from the atom. The electron will be ejected if its energy, E_{e-}, is greater than the binding energy of the electron, E_b:

$$E_\gamma = E_{e-} - E_b \tag{2.4}$$

where E_γ is the energy of the incoming photon, illustrated in Fig. 2.2.

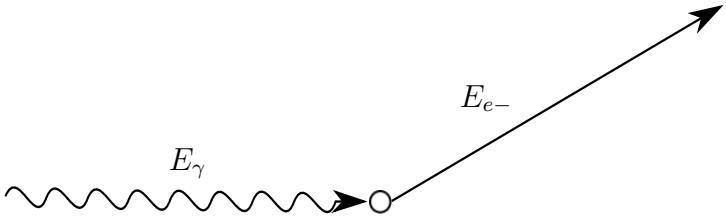

Figure 2.2: A schematic illustration of photoelectric absorption.

The most probable source of this photoelectron is from the most tightly bound K shell of the atom. This interaction only occurs with bound electrons, as free electrons cannot absorb the energy of the photon and conserve momentum. The nucleus of the bound electron will absorb the recoil momentum. This interaction will leave an ionised absorber atom which will be filled by either the capture of a neighbouring free electron or the rearrangements of electrons from other shells. Characteristic X-rays will then also be emitted through the rearrangement of electrons which fill the vacant shell.

2.1.2 Compton Scattering

Compton scattering occurs when through the deflection of a γ-ray by the outer shell electron of an atom within the absorbing material, illustrated in Fig. 2.3.

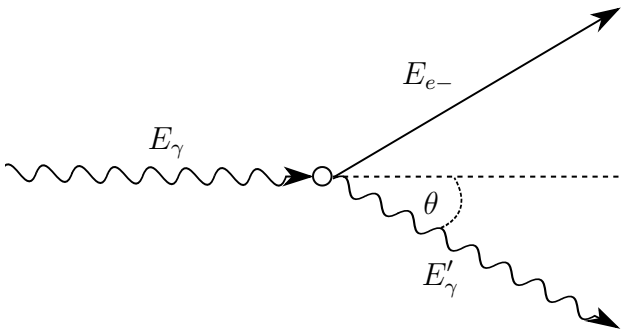

Figure 2.3: A schematic illustration of the Compton Scattering process.

The photon scatters at an angle dependent upon the incident γ-ray energy, where the energy of the γ-ray is much greater than the electron binding energy, $E_\gamma >> E_b$, partial energy from the γ-ray will be transferred to the electron.

Assuming the electron is at rest, the energy of the deflected γ-ray, E'_γ, is determined by the scattering angle, θ, through the conservation of momentum, and is given by the Compton scattering formula, Equation 2.5:

$$E'_\gamma = \frac{E_\gamma}{1 + \frac{h\nu}{m_0c^2}(1 - cos\theta)} \tag{2.5}$$

where m_0c^2 is the rest-mass energy of the electron, 0.511 MeV. For greater θ, more energy is deposited resulting in a lower E'_γ value. For lower scattering angles, less energy is deposited. This interaction process is the dominant interaction within the energy regime of 0.2 MeV $\leq E_\gamma \leq$ 7 MeV . The γ-ray will continue to scatter until it undergoes photoelectric absorption.

The Klein-Nishina formula

The Klein-Nishina formula, equation 2.6, indicates the differential cross section for Compton scattering as a function of scattering angle [21].

$$\frac{d\sigma}{d\Omega} = Zr_0^2\left(\frac{1}{1+\alpha(1-cos\theta)}\right)^2\left(\frac{1+cos^2\theta}{2}\right)\left(1+\frac{\alpha^2(1-cos\theta)^2}{(1+cos^2\theta)(1+\alpha(1-cos\theta))}\right) \tag{2.6}$$

$\alpha = hv/(m_0c^2)$ and r_0 is the classical electron radius. Higher energy photons scatter forward and lower energy photons scatter isotropically, depicted in the polar plot of the angular distribution of photon scatters, Fig. 2.4.

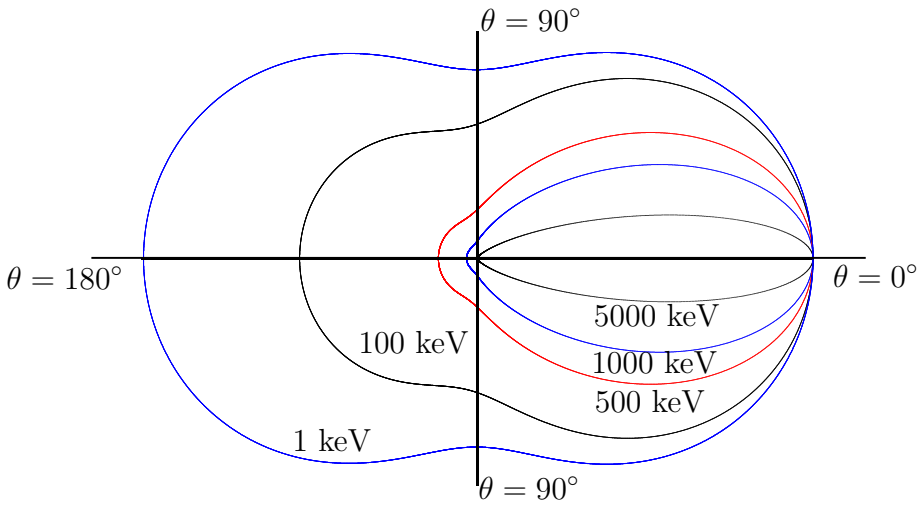

Figure 2.4: A polar plot of the angular distribution of photons incident from the left for germanium described by the Klein-Nishina formula.

2.1.3 Pair Production

Pair production occurs at photon energies, $E_\gamma \geq 1022$ keV. The γ-ray will interact with the Coulomb field of an atom and produce an electron and a positron pair, depicted in Fig. 2.5.

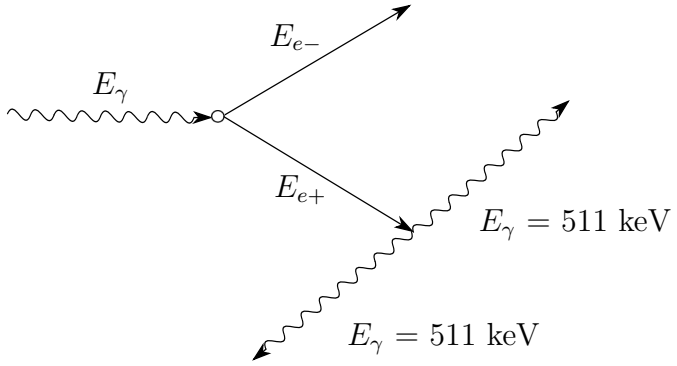

Figure 2.5: A schematic illustration of the pair production process. This process will only occur for photons of energies above 1022 keV.

A short distance later this positron will annihilate and produce two back to back photons of energy 511 keV. This process is the least likely to occur in the region of interest for γ-ray spectroscopy with HPGe detectors.

2.2 High Purity Germanium Spectrometers

The nuclear structure studies that can be performed depend on the properties of the spectrometer [7]. The performance of large HPGe spectrometers and the constituent detectors is quantifiable through determination of the efficiency, resolving power and energy resolution. These parameters are defined for the large escape suppressed spectrometers (ESS) arrays as well as the proposed AGATA array in Table 1.1.

2.2.1 Detection Efficiency

The ratio of the detector γ-rays versus those emitted from a radiation source is defined as the *absolute efficiency*, ϵ_{abs}. The *intrinsic efficiency*, ϵ_{int}, is the ratio of γ-rays incident on the detection volume which are detected. An important consideration for designing a HPGe spectrometer is the spectral quality. The

spectral quality is determined by the photo peak energy peak efficiency, ϵ_{phot}, of counts occurring in the spectral photo peak and the ratio between counts in the photo-peak to the total spectral counts, the peak-to-total ratio. The absolute efficiency of an array of N detectors which subtend the angle Ω, is

$$\epsilon_{abs} = \frac{N\Omega}{4\pi}\epsilon_{int} \tag{2.7}$$

where ϵ_{int} is the intrinsic efficiency for each detector. For a spherical array of N detectors the total efficiency, ϵ_Tot, is then given by Equation 2.8:

$$\epsilon_{Tot} = \frac{1}{4\pi}\sum_{N} R_{P/T}\Omega\epsilon_{int} \tag{2.8}$$

where $R_{P/T}$, is the peak-to-total ratio. The peak-to-total ratio determines what proportion of events are in the photopeak of interest, Equation 2.9:

$$R_{P/T} = \frac{\epsilon_{phot}}{\epsilon_{Tot}} \tag{2.9}$$

where a ratio is taken between total events detected, ϵ_{Tot}, and those counts occurring in the photopeak, ϵ_{phot}.

The most likely interaction in the energy range of interest is through Compton scattering. This mechanism highly affects the $R_{P/T}$ value, resulting in a loss of efficiency for nuclear physics studies. For standard ESS arrays, the efficiency achieved is sufficient for stable beam facilities as the Compton background counts are vetoed. However, the ESS arrays are not sensitive enough for the low beam intensity of radioactive ion beam (RIB) facilities, as discussed in Section 1.1.2. The development of tracking arrays allows for the summation of the energy deposited through multiple Compton scattering interactions and photoelectric absorption. This improves the efficiency of the arrays whilst maintaining the excellent peak-to-total values.

2.2.2 Spectrometer Energy Resolution

The energy resolution achieved in an energy spectrum, ΔE_γ (or the full width of the photopeak at half maximum, FWHM), is determined by the intrinsic energy resolution of the HPGe detector [7]. Germanium detectors have excellent energy resolution: 2 keV FWHM at 1 MeV (0.2 %) [22].

The intrinsic energy resolution is given by the sum of noise contributions due to statistical noise fluctuations, ΔE_S, incomplete charge collection ΔE_X,

and electronic noise resulting from the electronic components ΔE_E [22]. The intrinsic energy resolution, E_i, is given in Equation 2.14,

$$(\Delta E_i)^2 = (\Delta E_S)^2 + (\Delta E_X)^2 + (\Delta E_E)^2. \tag{2.10}$$

The value of the statistical noise is determined by the fluctuation in charge carriers (Section 3.1.1), which affects the energy, as shown in Equation 2.11:

$$\Delta E_S = \sqrt{(2.35)^2 F \epsilon_{pair} E_\gamma} \tag{2.11}$$

where F is the Fano factor. The Fano factor is related to the number of charge carriers produced, [23], described in Equation 2.12:

$$\langle \Delta N^2 \rangle = FN \tag{2.12}$$

For germanium, F $\sim$ 0.11. The Fano factor is defined as difference in the observed statistical fluctuations of the number of charge carriers versus that predicted by Poisson statistics [22].

Incomplete charge collection is the result of charge trapping in the Germanium material. Trapping rates are electric field dependant, and trapping occurs in low electric field strength, i.e. the detector corners.

Doppler Broadening

Doppler broadening contributes to a degraded energy resolution within the experimental setting. The energy of γ-rays produced by particles recoiling from nuclear interactions at high velocities (a large fraction of the speed of light, $\beta = v/c$) is shifted proportional to the source velocity. The energy shift is the Doppler shift and is given by:

$$E'_\gamma = E_\gamma \left(\frac{\sqrt{1-\beta^2}}{1-\beta cos\theta_\gamma} \right) \approx E_\gamma (1 + \beta cos\theta_\gamma) \tag{2.13}$$

for small β.

The final γ-ray energy resolution achieved is a combination of the intrinsic energy resolution, ΔE_i, the Doppler broadening due to the opening angle of the detectors, ΔE_D, the angular spread, ΔE_R, and the velocity variation, ΔE_v, of the recoil particles in the experiment.

$$\Delta E_\gamma = \sqrt{(\Delta E_i)^2 + (\Delta E_D)^2 + (\Delta E_R)^2 + (\Delta E_v)^2} \tag{2.14}$$

The energy resolution of an array therefore will depend upon the resolution of each detector as well as the overall array configuration. The development of segmented detectors, resulting in better position identification for first interactions, which reduces the effect of Doppler broadening.

2.2.3 Detection Sensitivity

The detection sensitivity of a γ-ray spectrometer is determined by its ability of resolve between two spectral γ-ray peaks of energy E_1 and E_2. The minimum value of the separation energy, $S_\gamma = E_2 - E_1$, that can be resolved determines the resolving power, R. The resolving power is also calculated by the energy resolution, ΔE_γ [3]. The resolving power of a spectrometer defined in relation to $R_{P/T}$ is given in Equation 2.15,

$$R = \frac{S_\gamma}{\Delta E_\gamma} R_{P/T}. \tag{2.15}$$

For ESS germanium arrays, this value was improved by the large peak-to-total through the suppression of background events. For the AGATA spectrometer, the high $R_{P/T}$ will be achieved through the summing of energy deposited by Compton scattered photons within multiple segments, as discussed in Section 1.2.1

Chapter 3

Basic Semiconductor Physics

Semiconductors are utilised across the field of radiation detection. Intrinsic semiconducting materials, including germanium and silicon, as well as compounds including cadmium zinc telluride (CdZnTe) have yielded many applications across research and medical fields. The use of semiconductors for radiation will be discussed in the following chapter.

3.1 Crystalline Structure of Semiconductors

Solids have an underlying structure in which outer atomic electrons are covalently bonded with neighbouring atoms in a *crystal lattice*. Germanium and silicon are both tetravalent semiconductors with four outer electrons forming covalent bonds to the neighbouring atoms. The atoms are arranged in a face centred cubic (fcc) arrangement, depicted in Fig. 3.1.

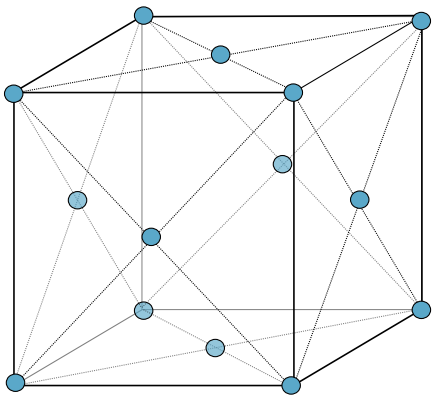

Figure 3.1: The face centred lattice structure of germanium and silicon. The four outer electrons of these tetravalent atoms form covalent bonds with neighbouring atoms.

3.1.1 Electron Energy Bands and Charge Carriers

Within crystalline solids electrons exist in discrete allowed energy bands. The conductivity of this material is defined by the configuration of the conducting band and the valence band. Within a conductor, there is no gap between the valence and conducting bands, allowing electrons to travel freely throughout the germanium crystal. In the case of an insulator, these two bands are separated by a large energy gap (6 eV or more), such that electrons are held within the conduction band are not free to move. The configuration of energy bands is depicted in Fig. 3.2.

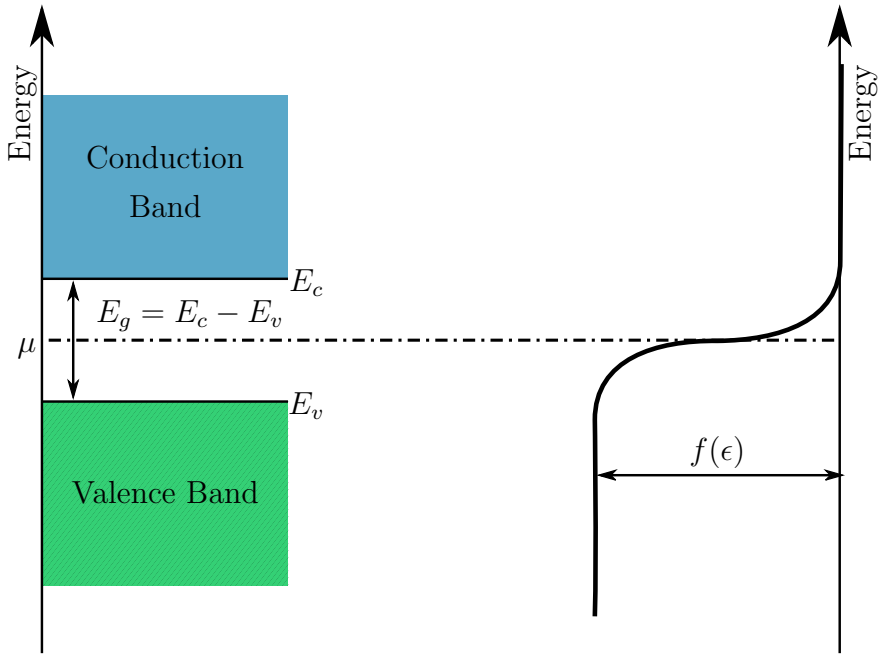

Figure 3.2: Band structure of solids. Within semiconductors the E_g value is such that the electrons may traverse the band gap. At $f(\epsilon) = 1/2$, the energy range is midway between the valence band ends and the conduction band edge. Adapted from [24].

Semiconductors possess energy band gaps, E_g, ~ 0.75 eV. At temperatures of 0 K, all electrons within a semiconductor are held within the non-conducting valence band. Electrons with energy ≥ 3 eV will cross the band gap and traverse the conduction band. At room temperature, thermally excited electrons will move and leave holes behind, creating an e-h pair, which are referred to as *intrinsic charge carriers*. An illustration of the covalent bonds and charge carriers is shown in Fig. 3.3.

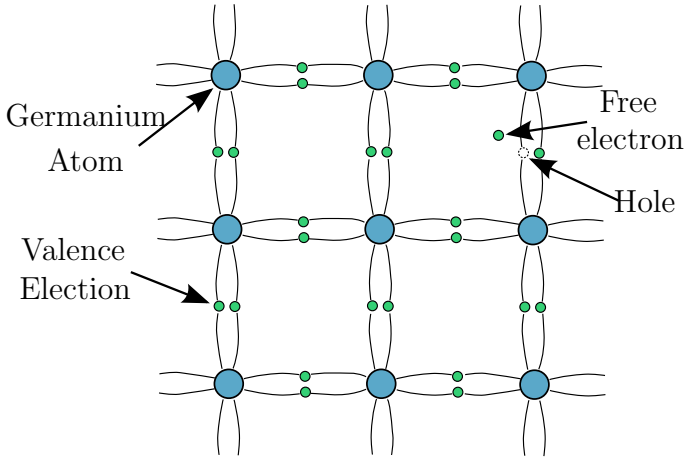

Figure 3.3: The covalent bonded electrons. At 0 K, all of the electrons occupy the crystal lattice. Above 0 K electrons can separate from their parent atoms and form e-h pairs, or charge carriers.

The intrinsic concentration of charge carriers can be determined as a function of temperature. The intrinsic concentration of charge carriers is described by Equation 3.1

$$np = n_i^2 = AT^3 exp\Big(\frac{-E_g}{k_B T}\Big) \tag{3.1}$$

where np is the number of charge carriers, T is the temperature, k_B is the Boltzman constant and A is a constant. This is the Fermi-Dirac probability, $f(\epsilon)$. To calculate the number of electrons excited to the conduction band at temperature, T, the chemical potential, μ, (the Fermi level) is used. The Fermi-Dirac distribution function gives the concentration of intrinsic charge carriers. For the conduction band, the energy, ϵ, of the electron is such that μ - $\epsilon \gg k_B T$. This results in the Fermi-Dirac equation reducing to:

$$f_e \simeq exp\left[\frac{\mu - \epsilon}{k_B T}\right] \tag{3.2}$$

where $k_B T$ is the thermal energy and f_e is the probability that a conduction electron orbital is occupied. This probability is illustrated in Fig. 3.2.

3.1.2 Crystal Doping

The behaviour of semiconductors can be manipulated with the addition of impurities through doping. When germanium, which possess 4 valence electrons, is doped with either a trivalent or pentavalent material, it will contain an excess

of charge carriers. Trivalent doping creates a p-type semiconductor through the introduction of more holes within the crystal lattice structure. Trivalent dopant such as lithium, with three valence electrons is commonly used. Negative, n-type impurities are introduced to produce more electrons. Phosphorous is commonly used in this case; the 5 valence electron atoms will replace the intrinsic atoms within the crystal lattice. The charge carriers introduced through this process will exist in energy levels close to the valence and conduction bands, respectively.

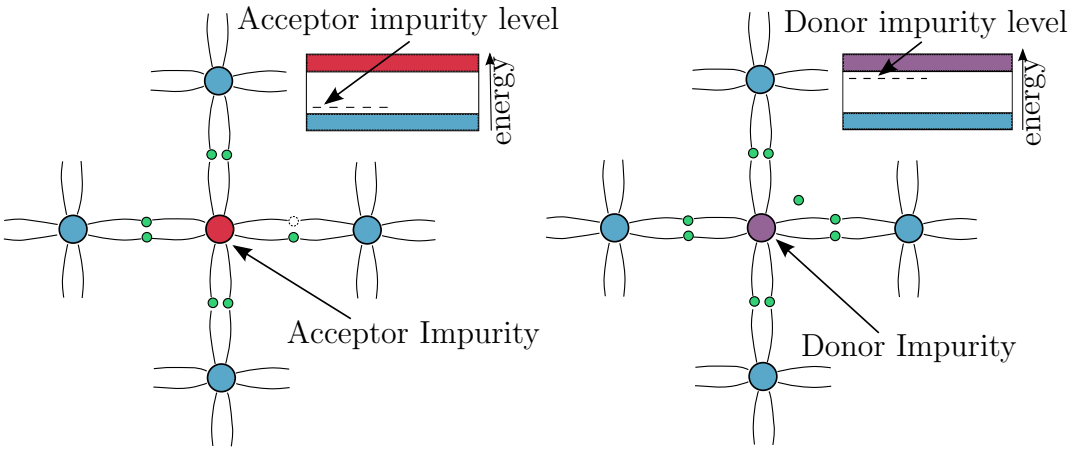

Figure 3.4: Donor and acceptor impurities with the donor energy level at which the excess charge carriers will occur. Adapted from [19].

A pure HPGe crystal contains an intrinsic equal amounts of electrons and holes. A typical zone refined HPGe crystal used for radiation detection is formed from a pure single Ge crystal, with a given net impurity concentration.

The AGATA crystals are formed from n-type germanium material such that they contain excess electrons, and possess a concentration of $\sim 10^{10}$ atoms/cm^3 impurities. The gradient of impurity concentration along the length of AGATA crystals is generated due to the crystal growing process.

3.2 Semiconductors for Radiation Detection

Semiconductor diodes can be utilised in order to detect radiation. For the detection of γ-rays, germanium is preferred over silicon due to the higher atomic number (Z = 32 for Ge over Z = 14 for Si) which increases the detection efficiency due to the higher stopping power. The band gap for germanium is also smaller than that of silicon, resulting in better energy resolution as

described in 2.2.2. Additionally, germanium detectors can be made from very pure materials, grown into large crystals. Si and CdZiTe material cannot be grown in a into large crystals with good resolution compared with germanium. Details of Ge and Si semiconducting materials are given in Table 3.1.

Property	Silicon	Germanium
Atomic Number, Z	14	32
Crystal structure	Diamond	Diamond
Density (g/cm^3)	2.33	5.32
Energy Gap, E_g (eV) (at 0 K)	1.165	0.746
Energy Gap, E_g (eV) (at 300 K)	1.115	0.665
Fano Factor	0.115	0.13
Energy per e-h pair (eV) (at 77 K)	3.76	2.96
Dielectric Constant	11.9	16.20

Table 3.1: Physical properties of silicon and germanium semiconductors relevant to radiation detection. This data was taken from [22, 25].

Germanium detectors must be cooled to liquid nitrogen temperatures (77 K) so that thermal energy will not contribute the production of charge carriers, whereas silicon detectors can be operated at room temperature due to the larger band gap energy which silicon posses.

3.2.1 The PN-Junction

When p-type and n-type materials are placed in close thermodynamic contact they form a diode. The excess electrons from the pentavalent material will diffuse towards the positive trivalent p-type material across the junction until the electrons and holes recombine. This creates a region depleted of free charge carriers, the *depletion region*, shown in Fig. 3.5.

An electric potential, V_0, is produced at the pn-junction by the recombination of the diffused charges. A net space charge distribution is formed which then produced the electric potential and associated electric field that limits further diffusion. This is referred to as the *depletion region* as it is depleted of free charge carriers. This is further discussed in Section 3.2.2.

For the AGATA array, n-type crystals are preferable over p-type crystals due to their resistance to neutron damage. Neutron damage causes germanium atoms to be dislocated from the lattice positions. Holes can become trapped and result in deteriorated charge collection. N-type crystals are less sensitive

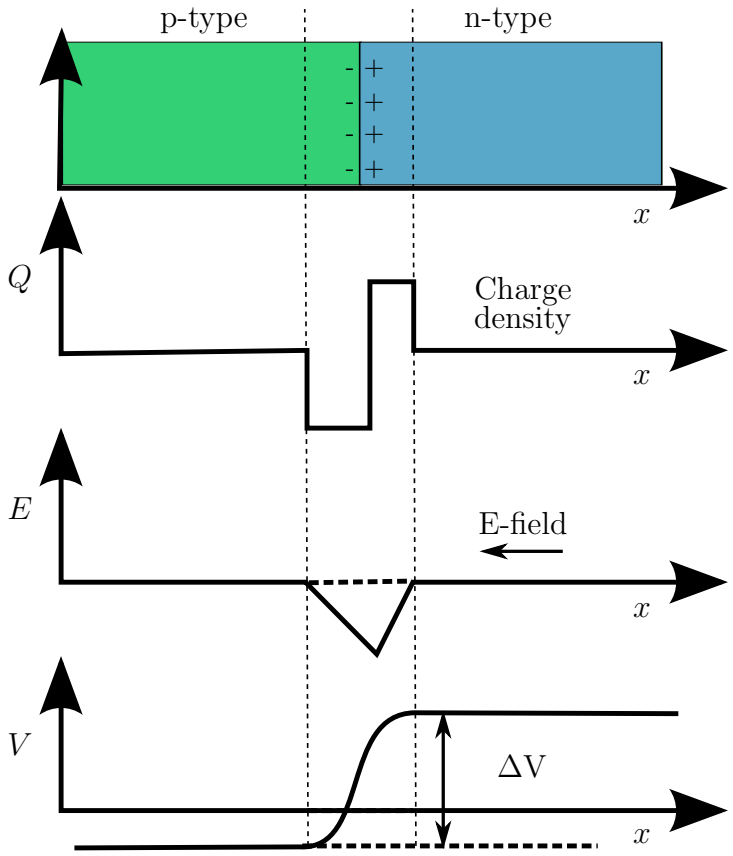

Figure 3.5: The equilibrium generated from the formation of the semiconductor junction. At the contact between the p-type and n-type material the free charge carriers recombine. An electric potential, ΔV is formed in this region which prevents further diffusion. Adapted from [19].

to neutron damage because holes are collected by the outer contact in these crystals. The holes travel a shorter distance on average due to γ-rays interacting on the outer region of the crystal.

Within the AGATA detectors, two contacts are applied to the detector. The outer contact which is implanted with a thin boron layer, 50 μm thick, of p-type material which creates the pn-junction. The inner contact is drifted with lithium which will form an ohmic junction. The rectifying contact of a coaxial detector is placed at the outer surface as this results in a lower field strength at the contacts when applying the depletion voltage.

3.2.2 Reverse-Biased Depletion Region

A semiconductor diode can be used as a detector through the collection of charge carriers produced by photon energy [22]. However, the small width of the depleted region will result in poor operational performance due to the small active volume. Therefore, under operation, a *reverse bias* is applied across the detector to extend the depletion region from the pn-junction. As this positive bias is applied at the pn-junction, the electrons are attracted towards the central contact. The depletion region will extend further toward the central contact of the crystal.

The applied voltage will enhance the depletion region. If the detector becomes fully depleted, the potential throughout the detector will be given by the *Poisson equation*, Equation 3.3. This can be solved to determine the potential, Φ, at any point within the crystal,

$$\nabla^2\Phi = -\rho/\epsilon_0 \tag{3.3}$$

where ρ is the net charge density (space charge) and ϵ_0 is the dielectric constant for the material. The electric field, E, can then also be calculated through:

$$E = -\nabla\Phi \tag{3.4}$$

Charge carriers excited in this region will be swept by the applied electric field to the contacts. The depth of the depletion region, d, can be calculated using the Poisson equation.

The depletion depth for a planar geometry is proportional to the applied bias, Equation 3.5,

$$d \cong \sqrt{\frac{2eV}{N}} \tag{3.5}$$

where e is the electric charge and N is the impurity concentration. High purity (low N) is required on one side of the pn-junction to create a large depletion region.

3.2.3 Applied Bias Voltage

The detector we are considering may be approximated to a coaxial detector. The Poisson Equation 3.3 can be written in cylindrical coordinates:

$$\frac{\mathrm{d}^2\Phi}{\mathrm{d}r^2} + \frac{1}{r}\frac{\mathrm{d}\Phi}{\mathrm{d}r} = -\frac{\rho}{\epsilon_0} \tag{3.6}$$

Solving this equation using Equation 3.4, with the potential difference equalling the applied bias voltage, the electric field can be described using:

$$-E(r) = -\frac{\rho}{2\epsilon_0}r + \frac{V + (\rho/4\epsilon_0)(r_2^2 - r_2^2)}{r\ln(r_2/r_1)} \tag{3.7}$$

where r_1 and r_2 are the inner and outer radii of the coaxial detector.

The electric field varies in the AGATA detectors. There is a passivating layer formed on the back of the crystal in order to limit surface leakage current. This layer must have high resistivity and be electrically passive. Additional problems can occur from the application of the passivating layer causing the electric field within the detector to bend away from the surface, resulting in low field strength and reduced charge collection in those regions [2].

The depletion region as discussed in 3.2.2 is the sensitive region of the detector. The voltage required to deplete the detector, V_d, is determined by setting $E(r_1) = 0$:

$$V_d = \frac{\rho}{2\epsilon_0}\left[r_1^2 \ln\frac{r_2}{r_1} - \frac{1}{2}(r_2^2 - r_1^2)\right] \tag{3.8}$$

where r_1 is the inner radius and r_2 is the outer radius of the coaxial detector.

The depletion region growth for a coaxial tapered HPGe detector is depicted in Fig. 3.6.

3.3 Signal Formation

As with many types of radiation detectors the number of freed charge carriers produced is proportionate to the energy introduced to the crystal, which is then converted into a current signal through several mechanisms. Within semiconductor detectors the charge carriers induce signals on electrical contacts. The mobility, μ, of these charge carriers determines the drift velocity and therefore the risetime of the signals.

3.3.1 Anisotropic Drift Velocity

The crystallographic axis orientation determines the path and drift velocity of the charge carriers. Miller indices define the lattice planes for crystal configu-

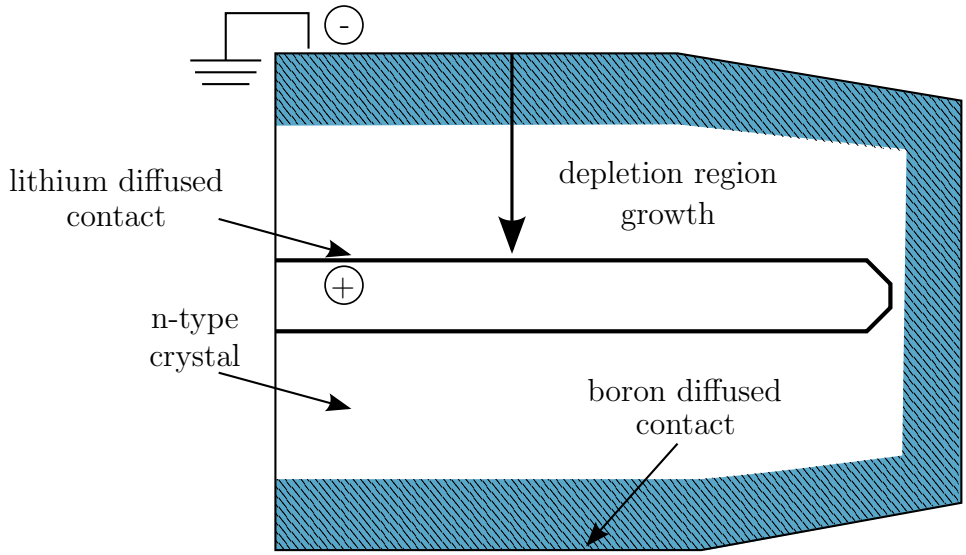

Figure 3.6: Depletion region growth from the pn-junction at the outer electrode. The reverse bias applied to the core contact allows for the depletion region growth.

rations [24]. For the face-centred cubic configuration of germanium, the Miller indices are (100), (110), and (111). These planes can be distinguished by the density of atoms which varies in each axis. The ⟨100⟩ direction has the highest density of atoms, whereas the ⟨111⟩ direction has the lowest density of atoms. The planes that the charge carriers travel across are indicated below in Fig. 3.7.

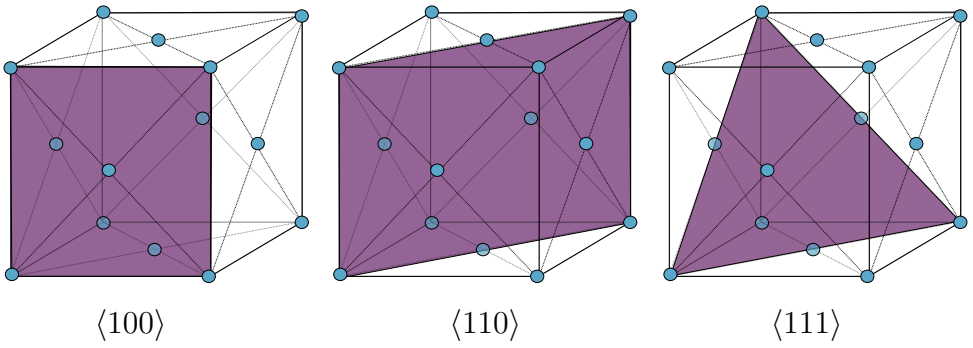

Figure 3.7: Germanium face-centred lattice structure, planes in which electrons will traverse with crystallographic directions ⟨100⟩, ⟨110⟩ and ⟨111⟩.

The drift velocity of the charge carriers, v_d, varies over these crystal directions as discussed within [26]. As the charge carriers traverse the crystal lattice their speed is dependant upon crystallographic directions, indicated in Fig. 3.8.

The electric field, E, also determines the drift velocity. The electric field

results in a net migration of charge carriers. The electron and hole velocity magnitude is proportional and in the direction of a crystallographic axis, parallel to the applied electric field. This charge carrier drift velocity, v, can be calculated using the charge carrier mobility, μ_0, from Equation 3.9, from [22]:

$$v = \frac{\mu_0 E}{[1 + (E/E_0)^\beta]^{1/\beta}}. \tag{3.9}$$

where E_0 and β are the modelling parameters. At high electric fields, μ is anisotropic and thus the drift velocities are anisotropic. The longitudinal anisotropy, v_l, can be defined for the principal crystallographic direction l, where Equation 3.9 becomes Equation 3.10,

$$v_l = \frac{\mu_0 E}{[1 + (E/E_0)^\beta]^{1/\beta}} + \mu_n E \tag{3.10}$$

where $\mu_n E$ accounts for effects at high field strength above 3 kV/cm at 80 K [27]. The electron drift velocity varying with crystal axis is depicted in Fig. 3.8.

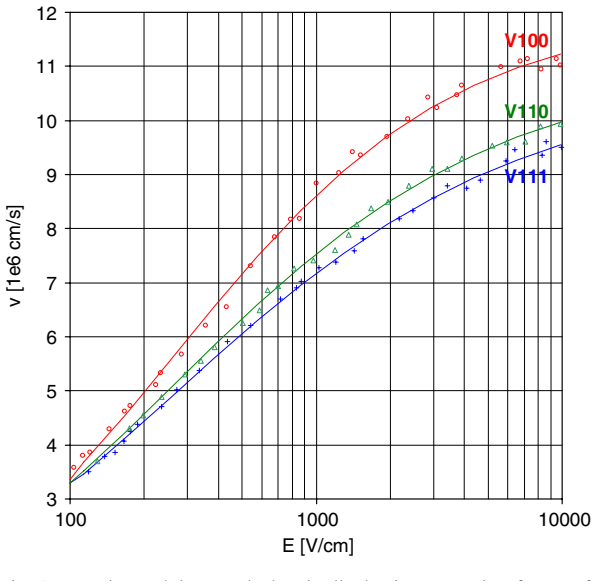

Figure 3.8: The electric field influence on the anisotropic electron drift velocity in germanium. The drift velocity varied over the three principle crystallographic axes. Figure from [27].

Values for the electron and hole mobilities were determined from [26–28]. The electron drift velocity increases first linearly with a applied electric field. At higher electric fields, the charge carriers travel with the highest velocity along

the ⟨100⟩-direction, where the atom density is lowest. The ⟨100⟩-direction is the *fast* axis, the ⟨111⟩ is the slow axis. This anisotropy of charge collection velocity is an important feature for pulse shape analysis, as the variation with crystallographic axes and the charge collection velocity as shown.

3.3.2 Signal Generation

Signal currents are induced on the crystal contacts through the movement of free charge, q, within detector. The charge is distributed in a localised manner such that the electrons and holes produced through a photon interaction can be considered as charge clouds of negligible size. As a charge cloud drifts towards an electrode, a charge is induced on the electrode. The current flowing towards this electrode is registered by the preamplifier which integrates it over a feedback capacitor; preamplifiers are discussed in length in Section 3.4.1. The output of the preamplifier yields a signal with amplitude through the field effective transistors (FETs) throughout the crystal from the Coulomb field of this charge cloud. The electric field throughout the volume also affects the Coulomb field. The time for the signal charges to reach the corresponding electrodes is the collection time t_C.

The signal charge, Q, induced on the electrode is given by Gauss' law, Equation 3.11:

$$Q = \oint_S \epsilon_0 E \cdot dS \tag{3.11}$$

where S is the surface of the electrode over which the charge, Q is calculated. The total charge induced is calculated by computing the electric field induced at each point over the surface of the electrode, described in Equation 3.12,

$$E \propto Q = \int_0^{T_c} i_{sig}(t) \cdot dt \tag{3.12}$$

where the charge is determined by, i_{sig}, the current of the feedback signal within time, t.

3.3.3 Weighting Potential

Solving Equation 3.11 is arduous due to the fact that the field must be recalculated at every point of the charge trajectory. The induced charge can be calculated from the current induced on the electrode as introduced in [29].

The Shockley-Ramo theorem can be used, which states that the instantaneous charge, Q, and induced current, i, can be calculated using Equation 3.13 and Equation 3.14, where v is the instantaneous velocity [30, 31],

$$Q = -q \cdot \Phi_w(x) \tag{3.13}$$

$$i = qv \cdot E_w(x) \tag{3.14}$$

where q is the electric charge in the detector at position x, $\Phi_w(x)$ is referred to as the weighting potential and E_w is the *weighting field*.

The weighting potentials are the solution to the Laplace equation with the boundary condition of $\Phi_w = 1$ on the electrode and $\Phi_w = 0$ on all other electrodes.

From the boundary conditions, a charge placed near the collection electrode will induce an image charge on the electrode, -q, while the charge induced on neighbouring electrodes will be 0. *Transient charges* are induced during the collection time on the neighbouring electrodes, which are proportional to the radial position of the charge carriers. This results in the ability to identify the radial position of the photon interaction.

The weighting potential makes calculation of the induced charge much simpler than Equation 3.11 by using the charge location and electrode configuration, which only require the weighting potentials to be evaluated once.

3.4 Detector Electronics

3.4.1 The Charge Sensitive Preamplifier

Preamplifiers are necessary in order to shape, amplify and convert the small amount of charge induced on the detector electrodes into a voltage signal. The capacitance of semiconductors will vary with temperature. Due to this effect, preamplifier must be *charge sensitive* rather than voltage sensitive [19].

In the first step of pre-amplification, induced charge is converted into a current discussed further in [25]. The preamplifier preserves the leading edge of the signal produced by the detector.

A schematic representation of a simple charge sensitive preamplifier is given in Fig. 3.9.

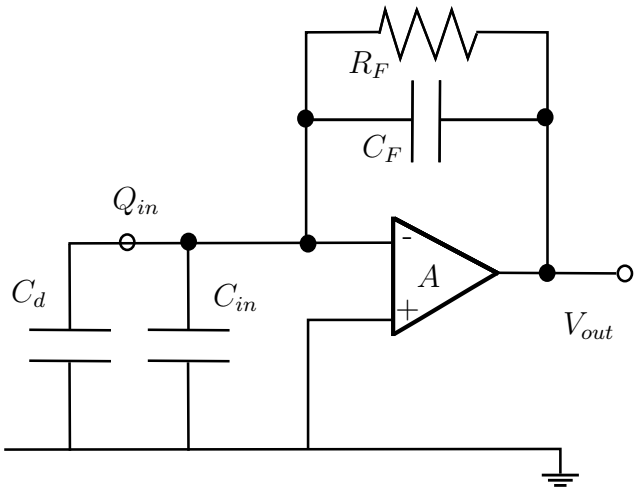

Figure 3.9: A schematic depiction of the components of a basic charge sensitive preamplifier.

The charge pulse is integrated over the contact capacitor, C_d. Within the preamplifier, the signal is amplified with an inverting amplifier with a feedback capacitance, C_f. The signal produced by a preamplifier, V_{out}, is

$$V_{out} = -\frac{Q_{in}}{C_f} \tag{3.15}$$

where the charge, Q_{in}, can be calculated to be,

$$Q_{in} = V_{in}(C_f + C_d + C_{in}) \tag{3.16}$$

The preamplifier applies a pulse decay according to the time constant given by C_f and R_f. The current discharges until the preamplifier output stage is brought back to the zero voltage floor with a decay constant of the feedback circuit ($\tau = R_F C_F \sim 1\ ms$), which is converted by the pole-zero cancellation network into $\tau = 50\ \mu s$ in a later stage of pre amplification. The preamplifier must be placed as close as possible to the detector to minimise noise induced by the resistivity of the wire between the electrode and preamplifier, as the noise on the components will also be amplified.

3.4.2 The AGATA Preamplifier

AGATA preamplifiers have been developed for use within the AGATA triple clusters. The preamplifier structure is divided into two parts, a cold FET component and a cold low noise transimpedance amplifier, pole-zero stage, dif-

ferential output buffer and a fast-reset. Two segment and one core AGATA preamplifiers have been designed by the collaboration in GANIL, The University of Milan and the University of Cologne, the details of which are discussed in [32]. The configuration of the AGATA preamplifier is shown in Fig. 3.10, adapted from [32].

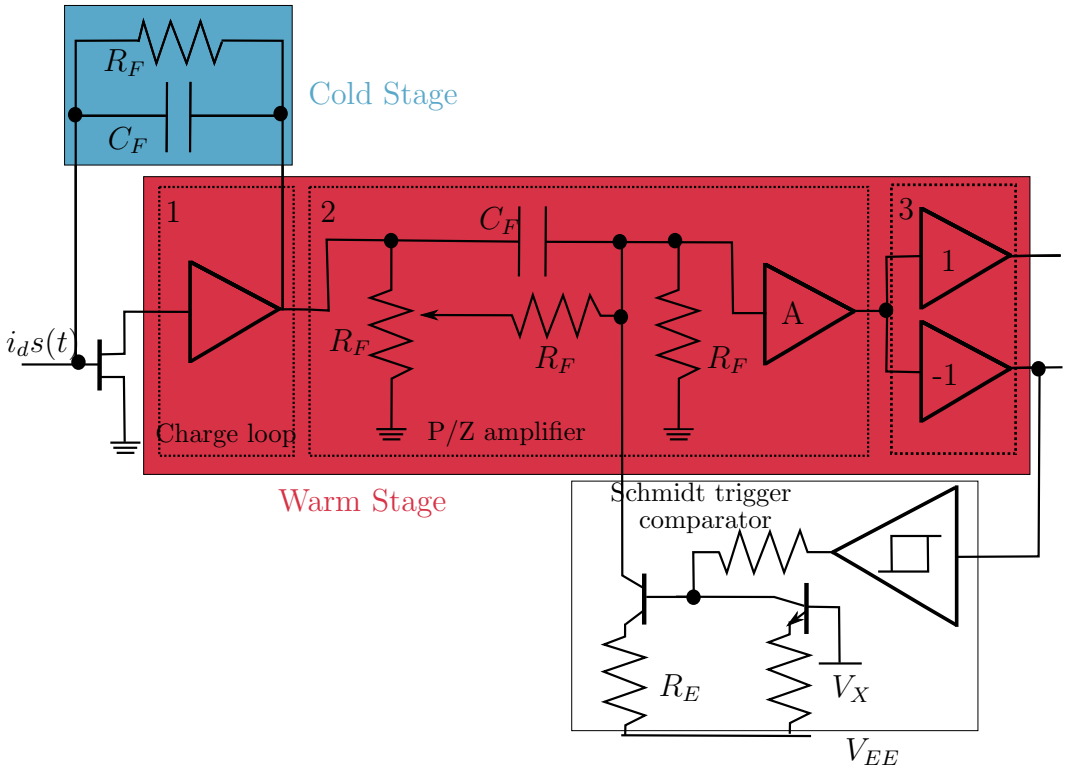

Figure 3.10: A simplified illustration of the AGATA hybrid preamplifier. The FET is located in the cold stage very close to the detector.

Each segmented AGATA capsule utilises 36 cold FETs for the segments and one for the core. These are placed within the cooling cryostat directly next to the capsule to minimise noise, as discussed above. Six warm segment preamplifier boards and one core preamplifier board provide the fast transfer functions for unperturbed traces which are necessary for pulses shape analysis. A high count rate capability is necessary to take advantage of the full efficiency of the array. The *fast reset* utilises a Schmitt trigger comparator to discharge the current. This component continuously senses the amplitude of the preamplifier output signal, which is then discharges so that the baseline returns to zero.

3.4.3 Crosstalk

Crosstalk occurs through the capacitive coupling between both the segments of a multifold detector and the connection of the segments with electronics [33]. Real charge signals induce transient signals and non-transient signals upon neighbouring components and segments through this process. This effect degrades the energy resolution as the signal is shared between multiple segments.

There are two components to the signal shape induced by crosstalk, proportional and differential. The proportional crosstalk is related to the magnitude of the charge signal. The derivative cross talk is the derivative of this real charge signal. Corrections can be applied to the detector output data that can account for the crosstalk [34].

Chapter 4

AGATA Asymmetric Capsule Performance

The AGATA triple cluster (ATC), depicted in Fig. 1.2(b), is the detection unit of the AGATA spectrometer. Each ATC is composed of three 36 segment asymmetric semi-hexagonal encapsulated HPGe crystals coupled within a single cryostat. The front face shape of the three unique crystals only varies in the differing angles of the asymmetric hexagonal shape [13]. Two AGATA encapsulated HPGe crystals, A004 and A006, have been studied and characterised in this work.

Energy resolution and efficiency measurements were made using several radiation sources in order to test the performance of the capsules. These measurements are used to ensure that the capsules are within the AGATA performance specifications. Highly collimated photon scans of each capsule were performed to study electrical response in detail. This scanning process and the results are discussed in detail in Section 4.3. Characterisation measurements were made to define the charge collection parameters as discussed within [28]. A detailed comparison between the two capsules, A004 and A006, is made within Sections 4.4.1, 4.7 and 4.8.

4.1 Capsule Details

The AGATA encapsulated crystals are manufactured by Canberra Eurysis in France. An agreement with the manufacturer restricts each capsule to several design criteria specified by the AGATA collaboration [35]. Each crystal has a asymmetric front face shape, tapered at an 8 $^\circ$ angle to an asymmetric hexagon

as shown in Fig. 4.1. Each crystal has a back diameter of 80 mm and a length of 90 ± 1 mm [13]. The centre contact bore hole where the *core* electrode is located has a 5 mm radius and extends to within 13 mm of the front face. Each AGATA HPGe crystal is electrically divided into 36 segments, shown in Fig. 4.1.

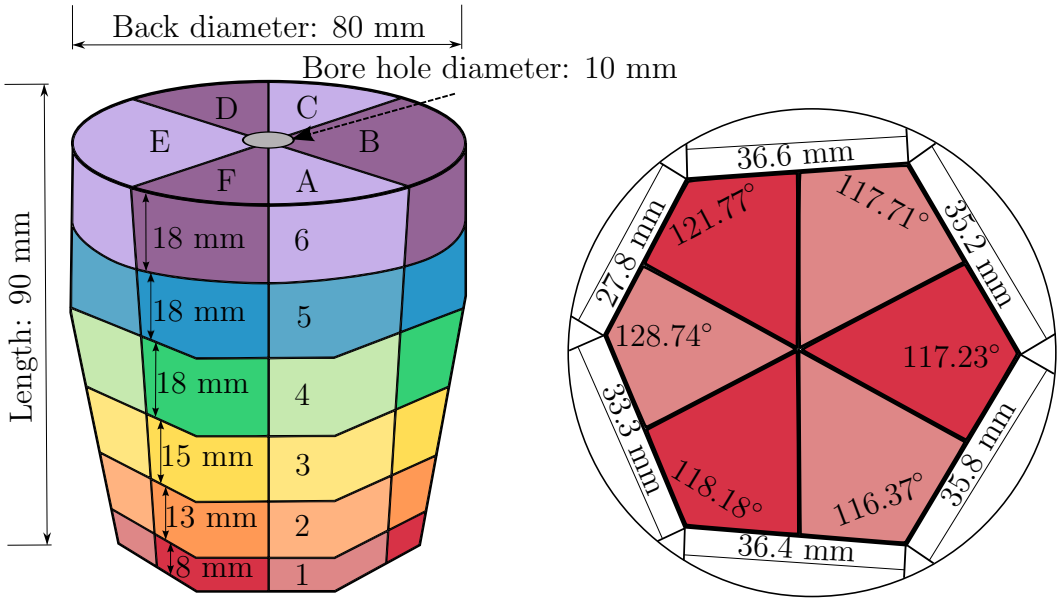

Figure 4.1: Electrical segmentation of AGATA A-type asymmetric detector. The labelling scheme of each segment is depicted as well as the crystal dimensions and ring depths and segment dimensions (right). The segment dimensions correspond only to the A-type crystal.

This hexagonal tapering is necessary for the close packing of the crystals which allows for the full AGATA array to achieve 82% solid angle coverage. The asymmetric shape is required for the geodesic tiling of the crystals. The segmentation of the detectors yields 6 rings of depths 8, 13, 15, 18 and18 mm from the front of the crystal. Each ring is also segmented into 6 sectors, which produces slightly differently size segments due to the asymmetry of the crystal shape. The segments are optimised in size and the rings optimised in width for uniform γ-ray distribution and pulse shape sensitivity through simulations [36].

Each crystal is encapsulated and hermetically sealed within an aluminium canister which has a thickness of 0.80 ± 0.05 mm and a spacing from the Ge crystal between 0.4 and 0.7 mm. The bare germanium crystal itself weighs approximately 2 kg. Six connector feedthroughs located at the back of the capsule access the 6 sectors and the 36 segmented outer contacts. A photograph of the A006 AGATA capsule is shown in Fig. 4.2. The capsules are designed

to fit together within liquid nitrogen cooled triple cryostats. It is these triple cryostats that make up the AGATA detection unit, depicted in Fig. 1.2 [37].

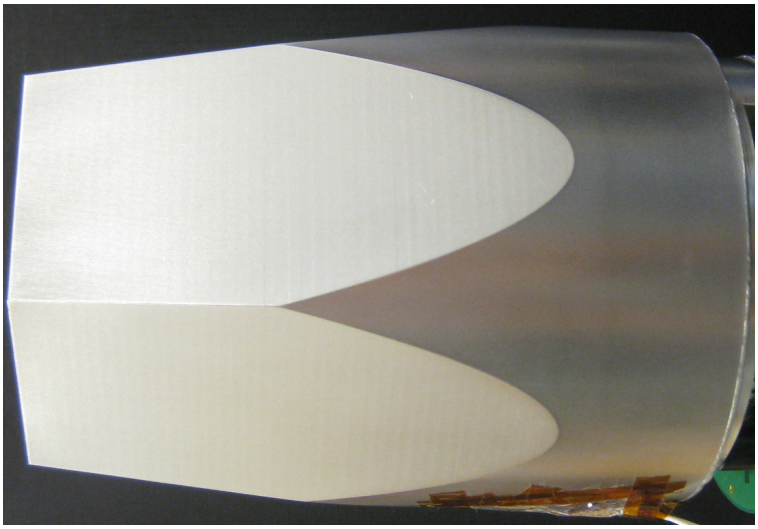

Figure 4.2: A photograph of the encapsulated A-type crystal, A006, before being mounted within the AGATA test cryostat. The aluminium canister is 0.8 mm thick. A PT-100 sensor is visible attached to the side of the detector which monitors the crystal temperature within a test cryostat.

4.1.1 Segment Labelling

The segments of an AGATA detector are also labelled numerically (1-36). For experimental purposes and algorithm construction, the alternative segmentation labelling scheme used to translate to the AGATA segment labelling is given in Table 4.1 where the number increases front to back from Ring 1 to 6 and from sectors A-F logically.

		Sector					
		A	**B**	**C**	**D**	**E**	**F**
Ring	**1**	1	7	13	19	25	31
	2	2	8	14	20	26	32
	3	3	9	15	21	27	33
	4	4	10	16	22	28	34
	5	5	11	17	23	29	35
	6	6	12	18	24	30	36

Table 4.1: Translation between the AGATA segment labels (A-F, 1-6) and the numerical labelling scheme used for convenience when testing single capsules.

The sector labels used in the details given by the manufacturer, Canberra, differ from those defined by the AGATA collaboration. Due to the positioning of the sector contacts, the construction of the test cryostat resulted in an additional labelling scheme. In this work, all results are given in the AGATA co-ordinates.

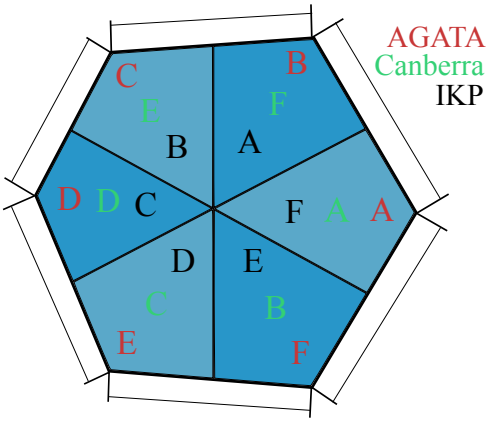

Figure 4.3: A translation between the AGATA, Canberra and IKP labelling system. In this work the results are all translated to the AGATA co-ordinates.

4.1.2 Impurity Concentration

Properties reported by Canberra for crystal capsules A004 and A006, are given in Table 4.2.

	A004	A006
Impurity Concentration at Front	1.16 x 10^{10} cm^{-3}	1.80 x 10^{10} cm^{-3}
Impurity Concentration at Back	0.49 x 10^{10} cm^{-3}	0.52 x 10^{10} cm^{-3}
Bias Voltage	+ 5000 V	+ 5000 V
Efficiency	82.2 %	79.0 %
FWHM at 1.33 MeV (^{60}Co)	2.25 keV	2.06 keV

Table 4.2: The properties and performance of the AGATA capsules as indicated by the capsule manufacturer Canberra [38, 39]. These properties are derived from the agreed AGATA specifications.

An important parameter for crystal performance is the impurity concentration. The impurity is not homogenous throughout the crystal volume due to the zone refining process, discussed in Section 3.1.2. The specified impurity concentration of the crystal is within 0.4 and 1.8 x $10^{10}$$cm^{-3}$. The highest impurity is located at the front of the crystal. Although this configuration has been agreed

upon with Canberra, some of the other AGATA capsules characterised at the University of Liverpool have possessed the opposite impurity gradient.

The reported impurity gradient for each capsule as a function of depth, as well as the AGATA specified impurity concentration limits are plotted in Fig. 4.4. The greatest impurity concentration is placed at the front of the crystal due to the dependance of the depletion thickness on impurity. The values plotted within Fig. 4.4 have been reported in the capsule manuals [38, 39]. The values for the intermediate depths do not indicate the *true* impurity concentration gradient, which is non-linear, as reported in [40]. The intermediate depths are likely reported by the manufacturer to give a linear depth-impurity relationship.

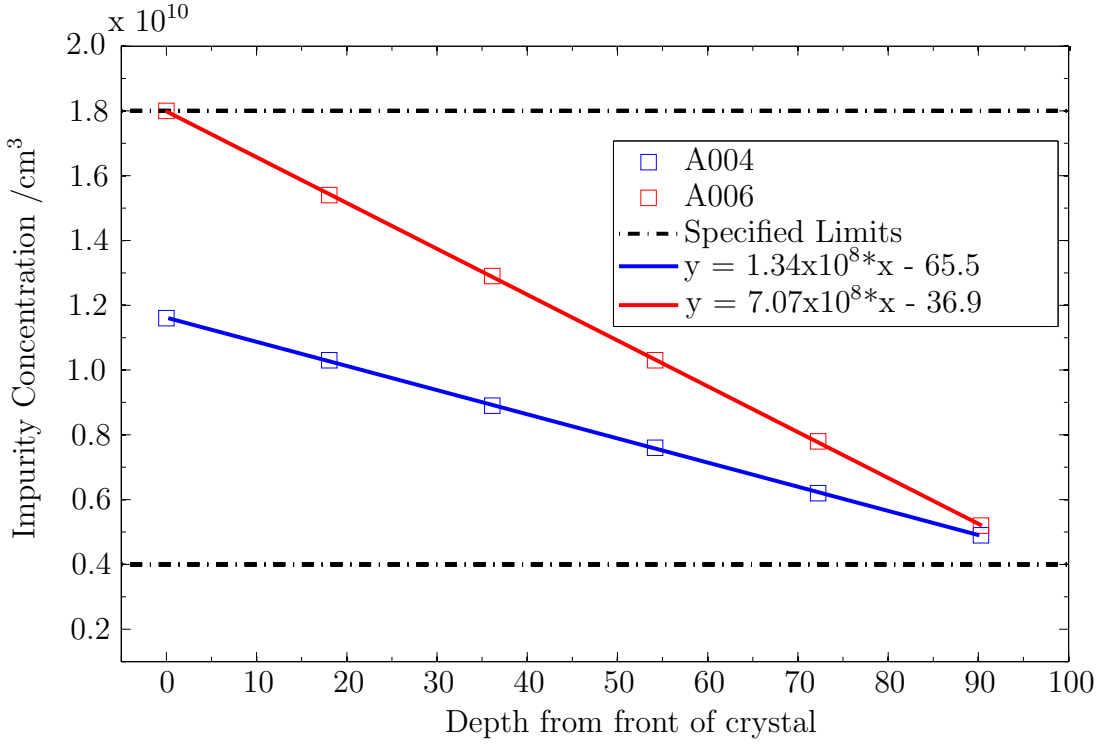

Figure 4.4: Impurity concentration as a function of depth for the A004 and A006 capsules as reported in the capsule manuals [38, 39]. These capsules are within the AGATA specifications.

4.2 Acceptance Testing

Each detector supplied by Canberra to the AGATA collaboration comes with a set of performance measurements made on the encapsulated crystals. The specification sheet from the capsule manual is in Appendix C. Energy resolution and efficiency measurements were required as part of a detector capsule acceptance tests required by the AGATA collaboration. It is the task of the acceptance testing groups, located in Liverpool, Köln and Saclay to verify that each capsule is working within the guaranteed specifications. Both energy resolution and efficiency were measured with analogue electronics used in the characterisation of the detectors. The crosstalk performance of each capsule has been measured for these detectors within the test cryostat and reported to the collaboration. Each capsule was mounted within a AGATA test cryostat, specially designed to test individual crystals with the AGATA preamplifiers and used to keep the detectors at operating temperature (∼77 K).

To perform these tests the differential signal from the detector preamplifier are converted into single-ended singles using CWC modules manufactured by TU Munich and IKP Köln. The detectors were biased to +5000 V using an ORTEC 659 bias supply in order to operate them. The converted single-ended signals were input into a ORTEC 671 spectroscopy amplifier with a 6 μs shaping time which was read into a PC based 16k Multi Channel Analyser and recorded using the Maestro programme [41].

4.2.1 Segment Energy Resolution

Segment energy resolution, E_{Res}, measurements were made by placing ^{241}Am and ^{60}Co sources directly next to the detecting segment. The E_{Res} FWHM measurement of analogue γ-ray spectra are made to verify the manufacturer specifications for the segment E_{Res}. The required FWHM values are to be within 1.3 keV for a 60 keV photopeak and 2.3 keV for a 1332 keV photopeak. The results of these measurements are given in Fig. 4.5 and Fig. 4.6. All of the segments for both detector measurements are within the guaranteed specifications. At the lower energy, 60 keV, the E_{Res} FWHM is effected mostly by signal noise on each segment. At higher energy, 1332 keV, the E_{Res} is dominated more so by statistical noise and less uniform.

The E_{Res} at both 60 keV and 1332 keV is determined by the detector ring in which the segment occurs. For the segmentation layout refer to Table 4.1.

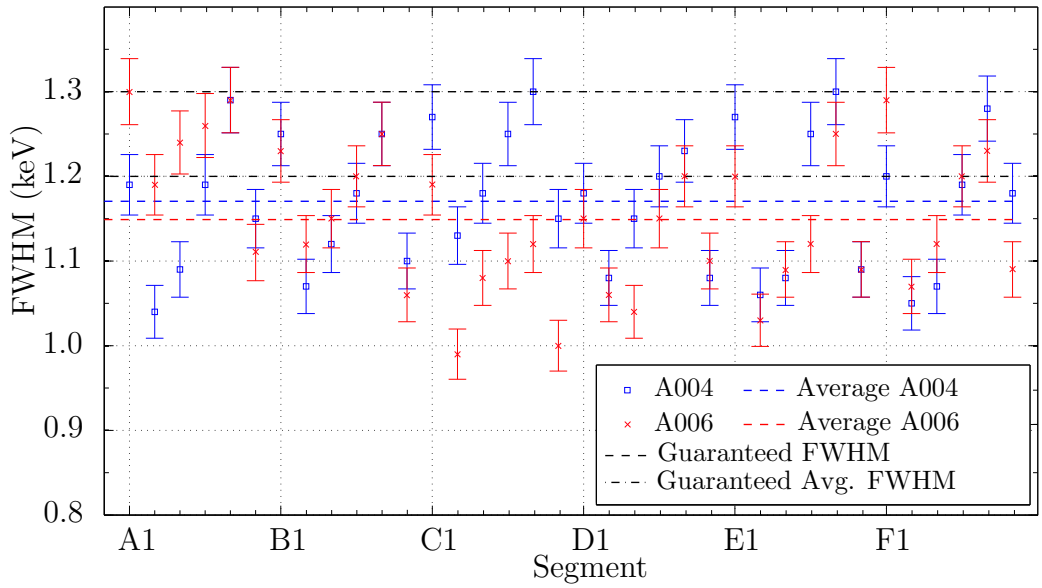

Figure 4.5: Performance of AGATA capsules A004 and A006 at 60 keV. The guaranteed energy resolution value for 60 keV γ-ray is up to 1.3 keV FWHM. The average energy resolution at 60 keV for A004 is 1.17 keV and for A006 is 1.15 keV. These values are within the guaranteed specifications for the average segment energy resolution. The trend in resolution within each detector sector is discussed within the text below.

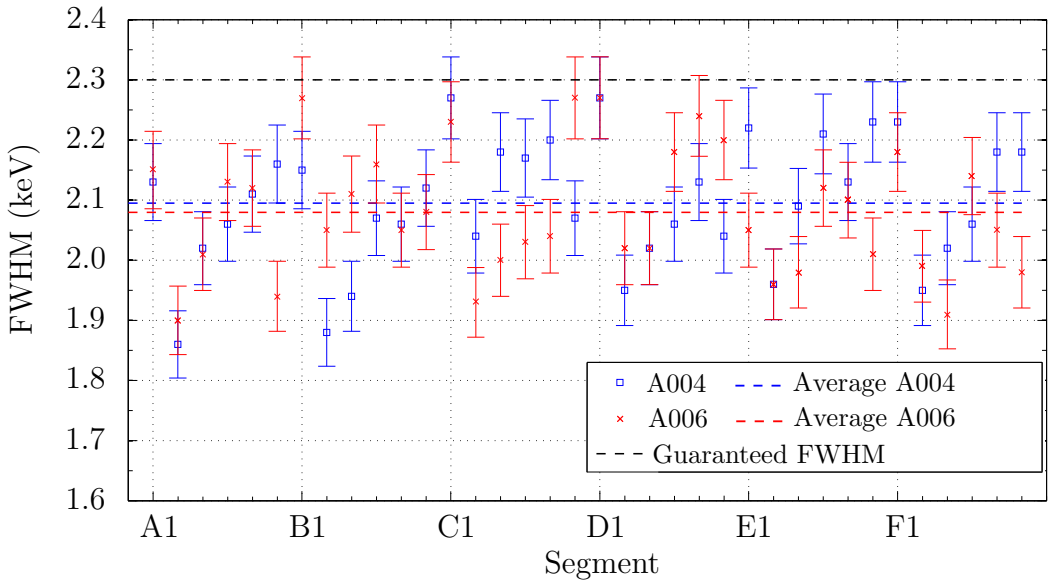

Figure 4.6: Performance of AGATA capsules A004 and A006 at 1332 keV. The guaranteed energy resolution value for 1332 keV γ-rays is up to 2.3 keV FWHM. The average energy resolution at 1332 keV for A004 is 2.10 keV and for A006 is 2.08 keV. These values are within the guaranteed specifications. The trend in resolution within each detector sector is discussed within the text below.

The observed trend is that the worst (higher) energy resolution is given in Ring 1 (A1 to F1). The resolution improves significantly within the Ring 2 segments (A2 - F2) for all sectors but then increasingly degrades from Rings 3-5 toward the back of the crystal. The resolution improves within of Ring 6 (A6 - F6).

Through each detector sector (A-F), the capacitance between the core and segments varies within the AGATA detectors as discussed in further detail in [40]. This ring capacitance determines the segment signal noise level, which is lower in Ring 2. The apparent physical size of the Ring 1 segmentation is smaller than Ring 2 due to the difference in ring depth (8 mm vs. 13 mm) and the taper of the detector. However, the *effective* segmentation of Ring 1 is larger than the other rings due to the electric field lines which travel from the front face to the central contact.

The Ring 1 segments have a reduced energy resolution compared to the Ring 2 segments due to the larger Ring 1 capacitance. On average the energy resolution is improved by 0.2 keV from Ring 1 to Ring 2. The second trend observed is the worsened energy resolution value from Ring 2-5. This is also explained by the larger segment size in Rings 3-5 due to the change in segment capacitance. The segment size within Ring 6 is reduced due to the *passivation layer* introduced at the back of the HPGe crystal [2]. Thus, the Ring 6 energy resolution is better than the Ring 5 segments in the 60 keV measurements.

4.2.2 Core Energy Resolution and Efficiency

The E_{Res} and efficiency of the core were measured using ^{57}Co and ^{60}Co sources placed at 25 cm from the front face of the detector with a count rate of approximately 1000 Hz in the core. The values for the core energy resolution measurements as compared to the manufacturer specified values are given in Table 4.3.

Spectral quality measurements which include the Peak-to-Total ratio, the FWTM/FWHM value and the E_{Res} were made on the capsule core signals. The relative and absolute efficiencies were also measured. The E_{Res} measurements of the core were within the guaranteed value; the Peak-to-Total ratio as well as the FWTM/FWHM values were within the value guaranteed by the manufacturer for both detectors.

The relative efficiency, ϵ_{FEP} values were lower than those reported by Canberra. However, they were within the estimated ± 8 % systematic and statistical error due to the uncertainty of capsule position within the cryostat. It was found

that the relative efficiency changes by a few percent with 1 cm differences in the source position. There is an uncertainty in the cryostat end cap position versus capsule position which would also contribute to the difference in measured value. The absolute efficiency of the core as a function of energy was also measured and the results of this study are presented in Fig. 4.7.

		A004	**A006**
ϵ_{FEP}	Canberra (%)	82.8	88.7
	Liverpool (%)	77.1 ± 8	78.2 ± 8
Peak-to-Total	Canberra	72.8	78.1
	Liverpool	50.1 ± 4.0	61.7 ± 4.9
E_{RES} (122 keV)	Canberra guaranteed	≤ 1.35 keV	
	Canberra meas. (keV)	1.10	1.02
	Liverpool (keV)	1.17 ± 0.09	1.17 ± 0.09
E_{RES} (1332 keV)	Canberra guaranteed	≤ 2.35 keV	
	Canberra meas. (keV)	2.25	2.06
	Liverpool (keV)	2.19 ± 0.18	2.09 ± 0.17
FWTM/FWHM (^{60}Co)	Canberra guaranteed	≤ 2.00	
	Canberra meas.	1.99	1.88
	Liverpool	1.91 ± 0.15	2.00 ± 0.16

Table 4.3: The capsule performance measurements for capsules A004 and A006. Values for the core Peak-to-Total, FWTM/FWHM and energy resolution at low and high energy values are within specification. The values for relative efficiency are reported, which are typical for these types of HPGe detector capsules.

The general higher efficiency observed for detector A006 can be explained by the uncertainty in the source to capsule distance. A source to capsule difference of a few millimetres can effect the absolute efficiency, as discussed above. The expected reduction in efficiency at very low energies is not observed in these measurements.

4.3 Photon Scanning

After the capsule performance is verified and accepted, collimated photon scans were made of the detectors in order to measure the average detector response as a function of position through capsule. This included a *Front Face Scan*, in which a highly collimated beam of single energy γ-radiation is moved across the front face of the detector in millimetre steps. Additional *Reduced Bias Scans* were made at reduced bias voltages in order to observe the detector bias voltage

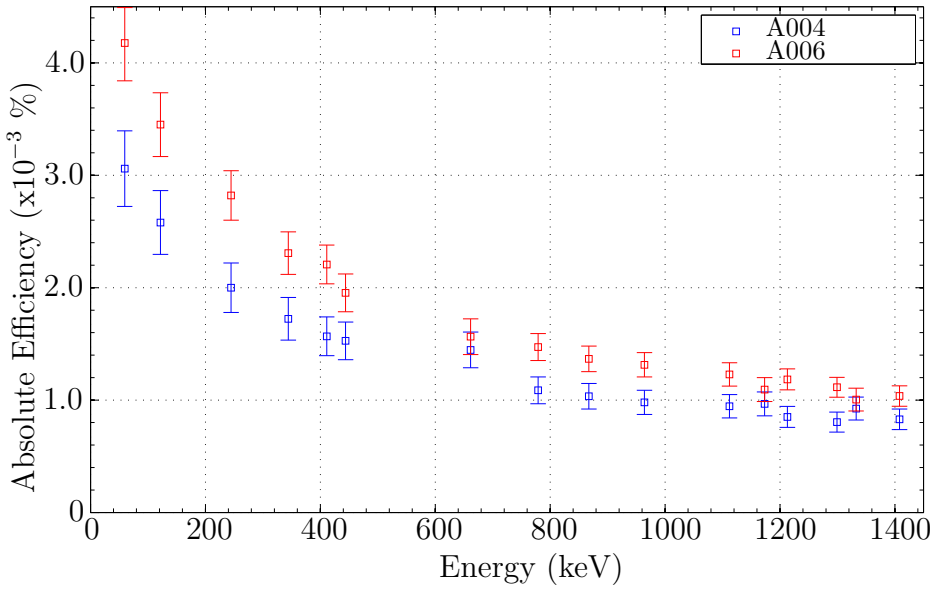

Figure 4.7: Absolute photopeak efficiency measurements versus γ-ray energy. These measurements were made using ^{241}Am and ^{152}Eu sources placed at 25 cm to the front face of the detector. Uncertainties are representative of the 3% statistical variance. Additional systematic error is also present due to the uncertainty of source position, estimated as $\pm$ 8% of the values.

depletion. Finally, each detector was scanned on its side for *Side Scans* at full and reduced bias voltages in order to observe depletion laterally along the crystal. Collectively these measurements form a basis to compare and understand each capsules' performance. Further details on scanning are described in [42]. The Liverpool scanning system has been used to characterise a number of different HPGe detectors for many applications including medical imaging, security as well as several other AGATA detectors, including symmetric detectors S001, S002, S003 and asymmetric AGATA detector C001 [43, 44].

4.3.1 Liverpool Scanning System

The AGATA test cryostat containing the capsule was mounted vertically with a storage dewar attached for LN_2, shown in Fig. 4.8. Both crystals A004 and A006 were scanned in 1 mm grid steps for 30 s and 60 s per step, respectively. The shorter scan time for A004 was chosen in order to perform these measurements more rapidly, as the detector was required for use within the AGATA demonstrator by the collaboration. The scans were made on a precision Parker scanning table [45] which provided the xy grid movement of the photon beam

with an accuracy of 100 μm and a 300 mm range in both directions. A ^{137}Cs γ-ray source of activity $\sim$ 1 GBq is collimated in two stages, which is depicted in Fig. 4.9.

Two tungsten collimators are used for the photon beam collimation: one 100 mm long x 5 mm diameter collimator followed by a second stage 80 mm x 1 mm diameter collimator. After the collimation, there is a divergence in the γ-ray beam resulting in a beam spot size of 1.1 mm diameter at the front face of the crystal and 1.6 mm at the back. This divergence and its affect on the position resolution is described within [46].

To discuss the details of this scan, several parameters must be defined related to data acquisition. An *event* is an interaction within the AGATA detector capsule. *Fold* refers to the number of segments in which a γ-photon interacts. A single photon may interact twice within a single segment and will still be considered a Fold-1 event. If a single photon interacts in two segments, it creates a Fold-2 event. The *Baseline Difference* (BD) energy is calculated from the difference in the maximum digitised traces and the baseline value. The *Moving Window Deconvolution* (MWD) energy is calculated by a moving window deconvolution algorithm [47].

The detectors were also scanned with a 5 GBq ^{241}Am source mounted in a lead block with a tungsten collimator. The lead block was placed at the same position as the ^{137}Cs collimator hole to be moved with precision using the scanning table.

4.3.2 Data Acquisition Electronics

Data was acquired for the 37 detector signals (36 segment and one core) using four 10 channel GRETINA digitisers [48] which were the only updated components to the scanning system described in reference [42]. Each digitiser card has 100 MHz flash ADCs (10 ns sample size). Data is acquired at a 128 sample trace length of 1.3 μs. The details of the card components are discussed in [49].

The GRETINA digitiser cards provide an accurate calculation of the energy deposited in the detector by applying a trapezoidal filter or *moving window deconvolution*. The MWD calculation accurately measures the integrated charge proportional to the energy deposited in the detector. The trace as well as MWD filtered energy were recorded for every event. The core signal is used to create an external trigger using a timing filter amplifier (TFA), constant fraction discriminator (CFD) set in leading edge (LE) mode and Gate and

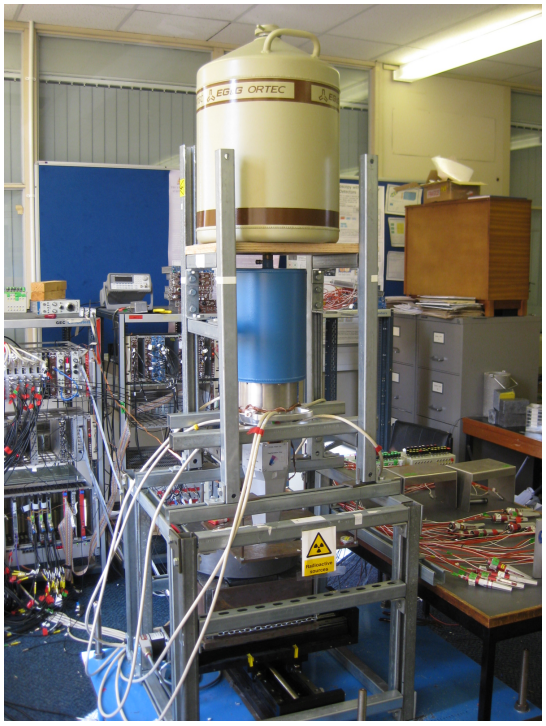

Figure 4.8: The AGATA test cryostat mounted above the Parker scanning table. The large storage dewar is connected to the cryostat to provide liquid nitrogen necessary in order to keep the detector within operating temperature of 77 K.

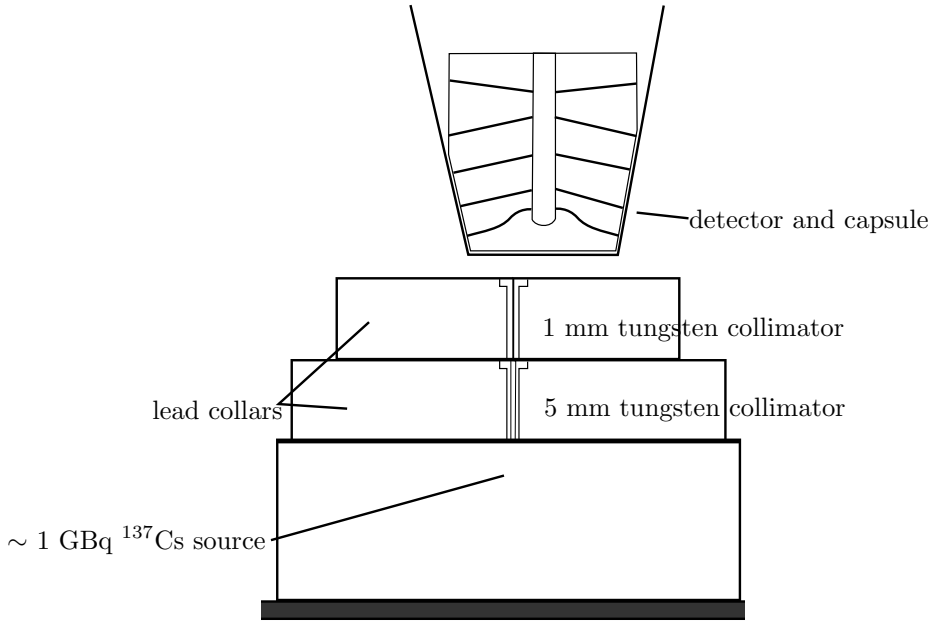

Figure 4.9: An illustration of the detector and collimator configuration for the front face singles scan. The two stage collimation is indicated.

Delay generator. A schematic diagram of data acquisition electronics is shown in Fig. 4.10.

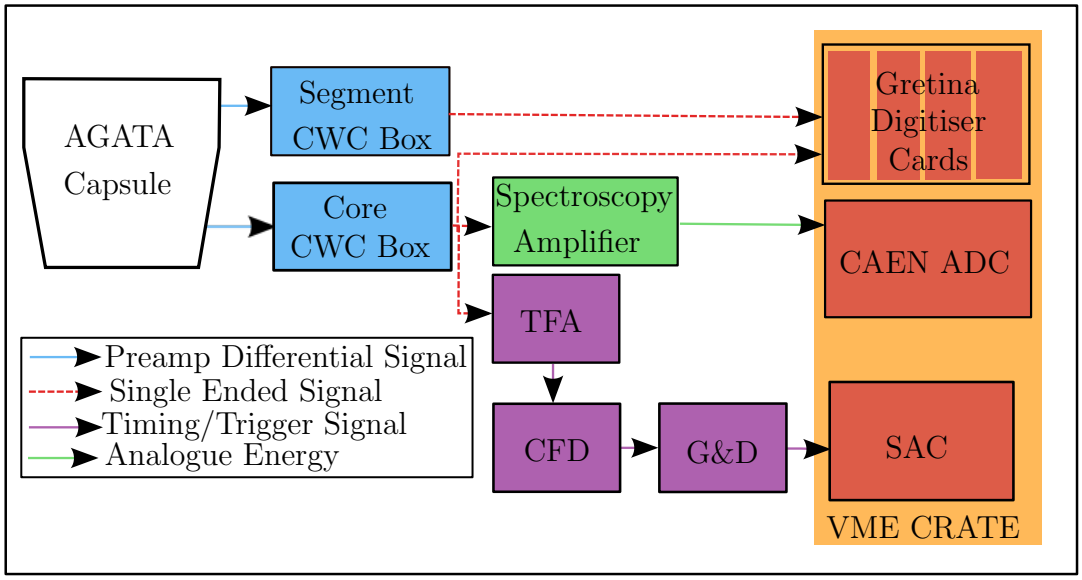

Figure 4.10: A schematic diagram of the electronics used to acquire *singles* data.

The LE threshold was set to reduce counts due to Compton scattering and noise for the ^{137}Cs scan and the ^{241}Am scan. This trigger signal is input to a Silena ADC controller (SAC) if the required photon energy was registered in singles mode. A common clock is shared among the 4 digitisers in order to maintain the time alignment. The accepted count rate was approximately 900 counts per second. An ORTEC 671 spectroscopy amplifier was used to shape the core signal with a 6 μs shaping time [50]. The height of the core signal was then measured and digitised with a CAEN V785 ADC. The scanning table position was also recorded. The SAC, CAEN ADC and GRETINA digitisers were all incorporated into a VME-X crate [51]. Data is acquired online using the MIDAS software package [52]. The data is output in Eurogam format.

The energy spectra calibration was performed with the MTSort package [53] using ^{152}Eu and ^{241}Am sources for each segment, which yield γ-rays between 59.5 keV and 1408 keV. GNUplot was used to determine the calibration parameters with a least-squares calculation. The BD energy is calculated from the recorded signal trace by taking the difference of the first and last 30 samples. Energy gates are set on the MWD core spectra and fold gates are set with the BD traces within the MTSort programme.

4.3.3 Summary of Singles Data

The data sets acquired for detectors A004 and A006 are listed in Table 4.4.

A004 ^{137}*Cs Front Scan*			**A006** ^{137}*Cs Front Scan*			^{137}*Cs Side Scan*		
Bias (V)	Grid	Step	Bias (V)	Grid	Step	Bias (V)	Grid	Step
5000	1 mm	30 s	5000	1 mm	60 s	5000	1 mm	30 s
2000	2 mm	30 s	4000	2 mm	40 s	1500	2 mm	40 s
1500	2 mm	30 s	3000	2 mm	40 s	1000	2 mm	40 s
1000	2 mm	30 s	2000	2 mm	40 s	500	2 mm	40 s
750	2 mm	30 s	1500	2 mm	40 s	250	2 mm	40 s
500	2 mm	30 s	1000	2 mm	40 s	100	2 mm	40 s
250	2 mm	30 s	750	2 mm	40 s			
100	2 mm	30 s	500	2 mm	40 s			
50	2 mm	30 s	250	2 mm	40 s			
			100	2 mm	40 s			
			50	2 mm	40 s			
^{241}*Am Front Scan*								
Bias (V)	Grid	Step	Bias (V)	Grid	Step			
5000	1 mm	10 s	5000	1 mm	5 s			

Table 4.4: The complete set of singles scan data acquired for both detector A004 and A006. The thorough scanning of these detectors allows for a study of depletion, crystal axis, charge collection and performance.

Both detectors were scanned on a grid of 80 mm^2, in 1 mm steps for the full bias front face measurement. Detector A004 was scanned with the ^{137}Cs beam in February 2010 and Detector A006 was scanned across the front face at full and reduced bias in April 2010 and scanned along the side of the detector at full and reduced bias in September 2010. Additional spectra not shown in the following sections are included in Appendix A. The side scan of A004 is not included due to a segment becoming disconnected in the side scan.

4.4 Front Face Singles Scan Results

This section details the results of a number of spectra generated from the ^{137}Cs and ^{241}Am front face scans of the detectors. Physical details, charge collection properties and the performance of detectors A004 and A006 will be discussed.

The sector positions of the detector results shown in the following sections are given in the AGATA coordinate scheme, shown in Fig. 4.11.

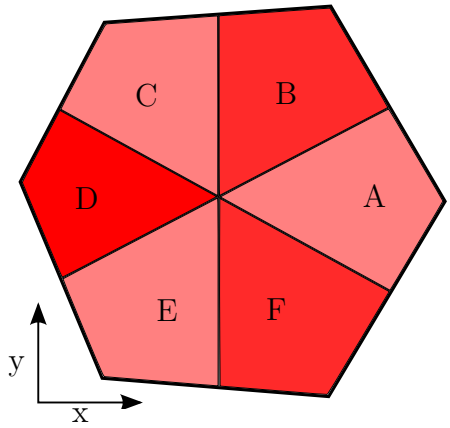

Figure 4.11: The detector position in the AGATA sector labelling system, viewed from the back of the detector. Shown to indicate the sector layout in the following results.

4.4.1 The ^{137}Cs Position Intensity

The primary interaction mechanism of a ^{137}Cs 662 keV γ-ray is Compton scattering which leads to position uncertainties. Therefore the front face singles measurements show the average detector response through depth. These measurements enable the investigation of detector response through the bulk of the crystal through the study of the charge collection. The detector is operated at the manufacturer specified bias voltage for the first front face scan. The lower bias voltage scans produced for detector A004 and A006 will be discussed in Section 4.7. Two dimensional matrices generated as a function of xy scanning table position are created from the MWD traces. For every event registered in the GRETINA digitisers per position, the matrices are incremented. The position intensity for detectors A004 and A006 are shown in Fig. 4.12.

The spectra produced for detectors A004 and A006 show a uniform performance. From this figure the rotation from scanning table coordinates to the AGATA coordinates is visible in the light rotated square background of each spectra. The position intensity of the A006 spectrum is approximately double the intensity of the A004 spectrum due to the difference in scanning time: 30 s for A004 and 60 s for detector A006. The intensity of detector A006 is also limited by the trigger rate on the GRETINA digitisers.

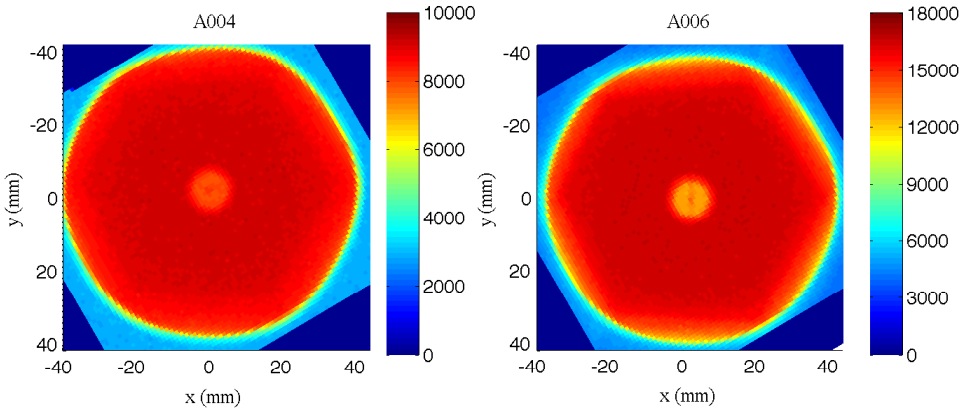

Figure 4.12: The counts as a function of position (intensity) for detector A004 and A006. These spectra are given from the traces output from the GRETINA digitisers. The intensity for detector A006 is greater than A004 due to the longer scanning time.

The highest intensity occurs in the central region of the spectra where the hexagonal front face of the detectors is observed and directly illuminated by the photon beam in this region. The outer region of the crystal has a lower region of intensity due to the less HPGe material in this region of the crystal. The central bore hole is visible in both spectra.

4.4.2 Fold-1 Gated Position Intensity

In order to examine the detector performance in detail several gates can be made on the position intensity spectra. A Fold-1 event requires that a single segment registers an event. By gating on single segment Fold-1 events when the 662 keV photon deposits its entire energy in one segment allows the detailed responses of the detectors to be observed and compared. The energy is determined by the MWD algorithm, whereas the fold is determined from the unfiltered trace.

There is a linear relationship between the BD energy and MWD energy. The position intensity response of the full detector gated on Fold-1 events is shown in Fig. 4.13.

Through gating on the Fold-1 events a large reduction in counts is observed from the ungated spectra resulting in roughly half the intensity. This indicates that Fold-1 events will be half of the maximum events for all folds. The A004 and A006 Fold-1 spectra show the good agreement in the response of the detectors. The fold gate also clearly indicates the segmentation boundaries within the two

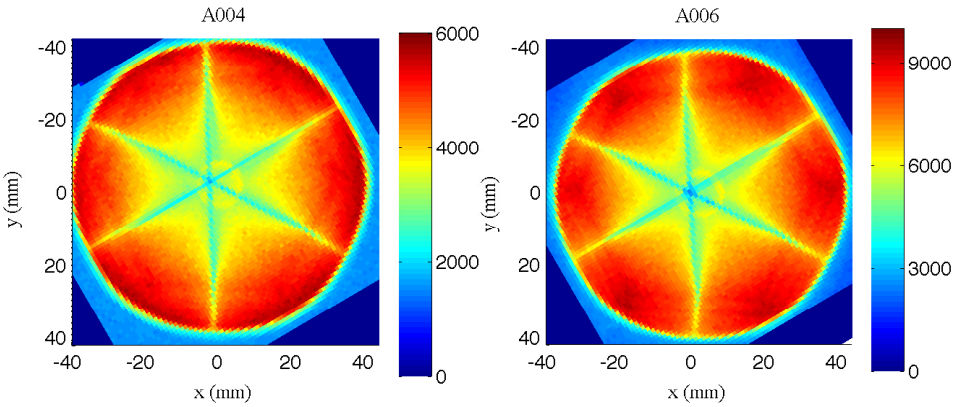

Figure 4.13: A004 and A006 front face intensity matrices as a function of xy scan position gated on Fold-1 events.

detectors. At segmentation boundaries and toward the centre of the capsule a reduction in Fold-1 events is observed. This indicates that in these regions the photons will Compton scatter between segments more readily.

4.4.3 Fold-1 662 keV Energy Gated Position Intensity

The position intensity spectra gated on Fold-1, 662 keV events are shown in Fig. 4.14. There is a further reduction of counts in this figure by gating on the photopeak energy as the maximum intensity reduces from 6000 counts to 1500 counts in the position spectra of detector A004 and 10000 counts to 3000 counts in the spectra of detector A006.

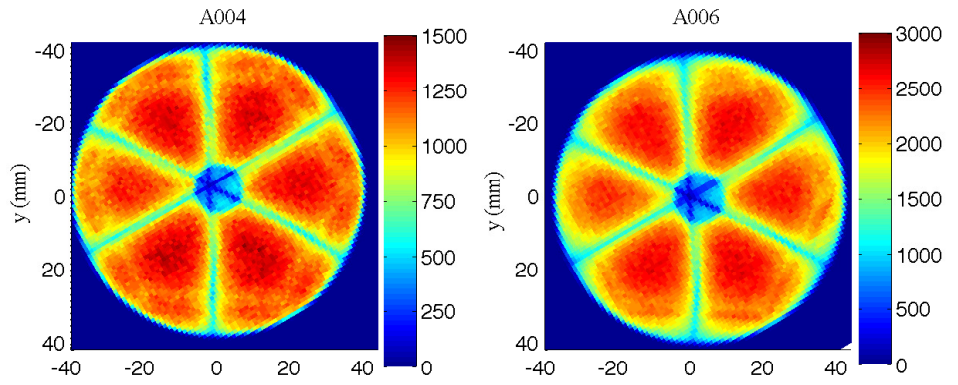

Figure 4.14: A004 and A006 front face intensity matrices as a function of xy scan position. The spectra are gated on segment Fold-1 events and the photon energy of 662 ± 2 keV photon energy.

The segmentation lines observed in the Fold-1 position intensity spectra are also observed in Fig. 4.14. The bore hole of the detector is observed in the spectra as a reduction in intensity. This reduction is due to the fact that the 662 keV γ-ray energy will not be fully deposited within the front ring segments. The asymmetry of the detector front face is also clearly observed. The position intensity spectra can also be gated on the detector rings in order to observe how the performance varies within each ring. Ring matrices indicating the intensity of counts as gated on the 662 $\pm$ 2 keV photon energy are shown in Fig. 4.15. Detector A004 at half the time per position, resulting in half of the maximum intensity for A004. The hexagonal profile of the front of the detector and the asymmetry of the front face shape is observed. The segmentation boundaries of the detectors is also observed. From Ring 3-6 the segmentation boundaries are not aligned across the centre of the crystal. This is due to the dominant anisotropy of drift velocity with respect to the crystal axis and will be further investigated in Section 4.6.

Within the ring spectra, the bore hole of the detector is easily observed in the back 2-6 rings. The segmentation crossing point is observed in Ring 1. The higher intensity of counts in the front ring indicates tendency of the photons to be absorbed or attenuated within a few mm's of HPGe material, concentrated at the front of the detector. This photon attenuation is described in Equation 2.1 as the intensity drops off exponentially with material thickness. The rings of high intensity around the back 4 rings are a result of the tapering of the crystal. From the intensity matrices of A004 and A006 it is observed that the detectors behave similarly and that the segmentation and bore holes radii are uniform. This comparison ensures the uniform capsule performance.

4.4.4 Compton Edge Gated Position Intensity

Single energy events can be utilised by gating on the MWD spectra Compton edge. The position intensity plot generated from gating on the Compton energy are shown in Fig. 4.16.

Rings 1-3 are shown for both detectors in order to indicate the areas of low energy charge collection within the detector. Single interactions show the uniform detector response through Ring 1. Due to photon attenuation, rings 2-3 only show intensity in the outer regions which are fully exposed to the photon beam. These intensity spectra differ from those generated from the photopeak gated spectra in several ways. The intensity on Ring 1 shows a more uniform

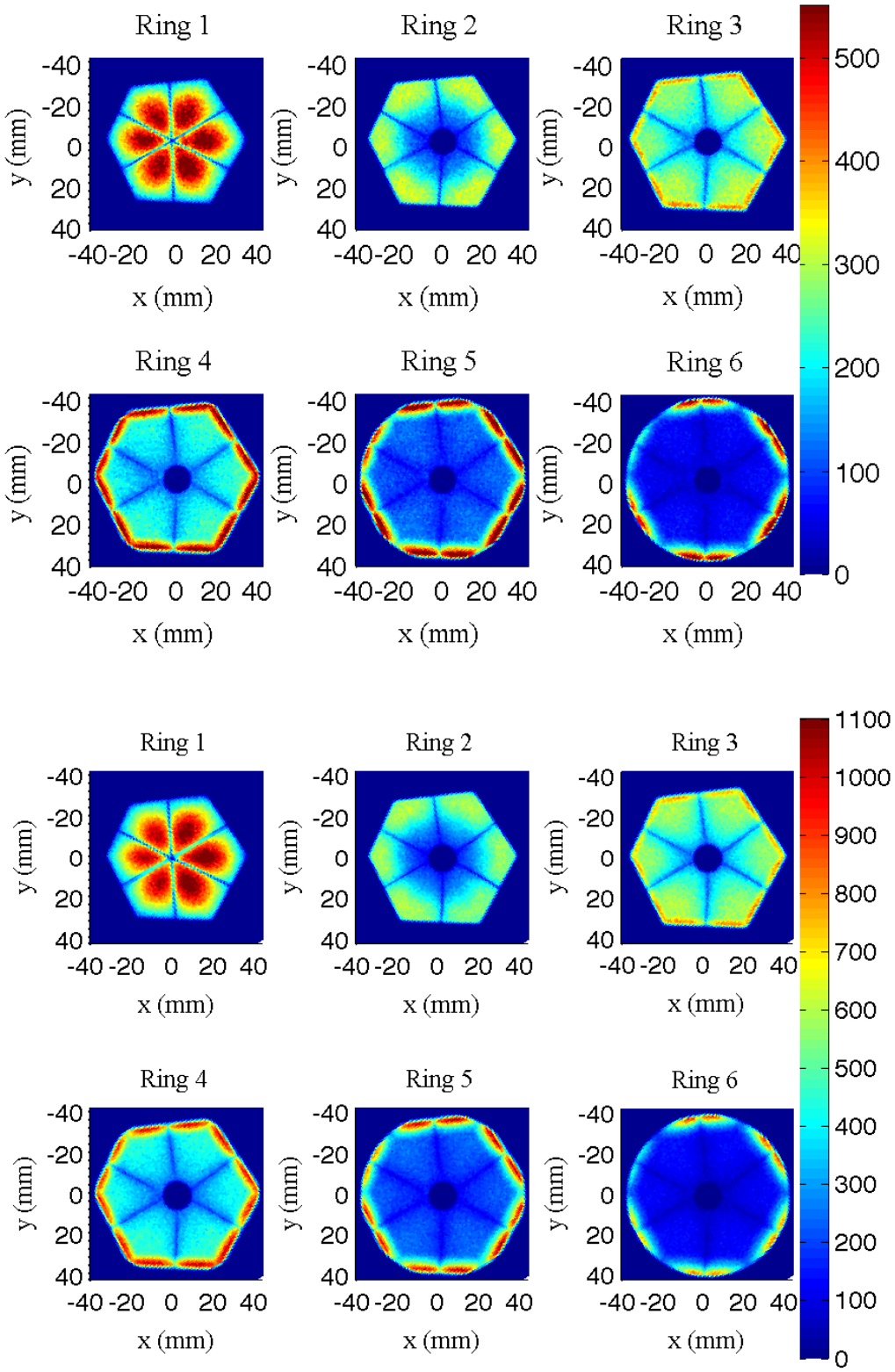

Figure 4.15: The ring gated A004 (top) and A006 (bottom) front face intensity matrices as a function of xy scan position. The spectra are gated on segment Fold-1 events and photon energy at 662 ± 2 keV photon energy and ring number.

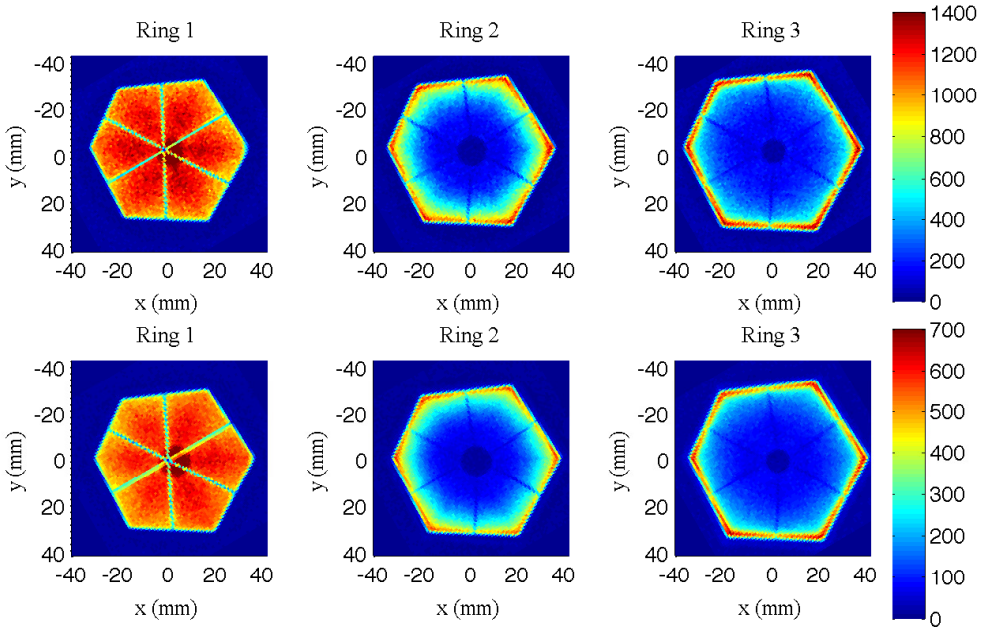

Figure 4.16: A004 Rings 1-3 (top), A006 Rings 1-3 (bottom). Intensity per position by ring. Gates are applied to Fold-1 events and the Compton edge energy. The central regions are less likely to be effected by low energy counts. The maximum intensity of A004 is half of the maximum intensity of A006 due to different scan times.

distribution of hits, rather than a clear distinction between segments occurring at the boundaries. This uniformity is due to the complete detection of the single interacting Compton scattering events. There is also a loss of intensity in the central region of the detector from the 2-3 ring due to the lower energy γ-ray. This is due to photon attenuation (Equation 2.1).

4.4.5 Transient Charge Asymmetry

During the process of charge collection, transient charges are induced on the neighbouring segments. These transient signals do not contribute to the net charge collected, but are utilised within pulse shape analysis. The magnitude of the image charges can be used to determine the azimuthal interaction position. An example of the transient signals produced by a real charge interaction in Segment C4 is given in Fig. 4.17.

In order to quantify the difference in image charge magnitude, the image charge asymmetry parameter, ICA, is defined as the absolute difference in the magnitude of the area of two adjacent transient signals. The image charge

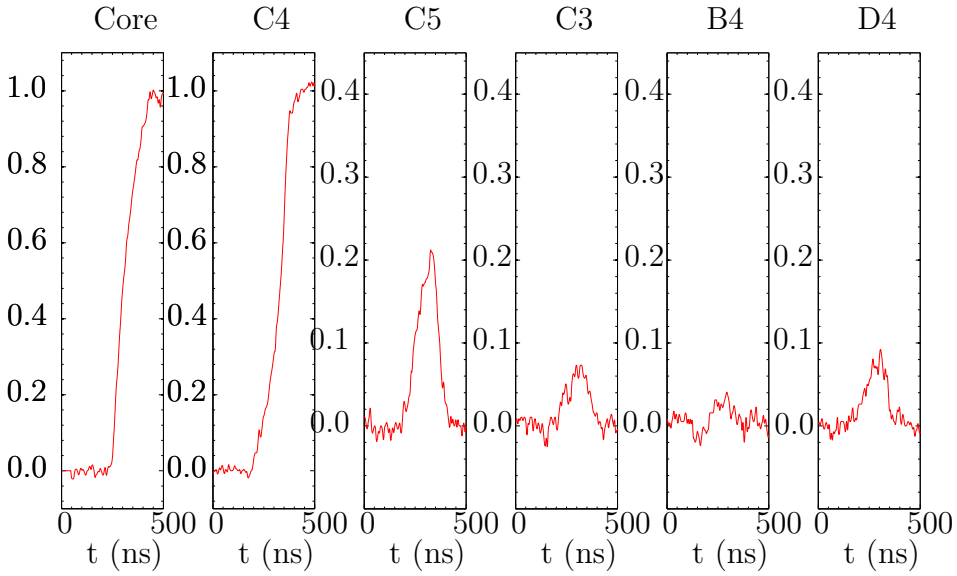

Figure 4.17: An example of the real and transient signals produced in a single interaction event in Segment C4.

asymmetry calculation is given in Equation 4.1,

$$ICA = \frac{(A_A - A_B)1000}{A_A + A_B} + 1000 \tag{4.1}$$

where A_A and A_B are the magnitudes of the two adjacent transient charges. Factors of 1000 are included to plot the ICA values. The magnitude of the induced transient signal is dependant upon the interaction location. An interaction occurring close to a segment boundary will result in a higher asymmetry. The average ICA as a function of xy position is given in Fig. 4.18.

Extreme high and low values of ICA indicate a strong asymmetry. The minimum asymmetry response is located at the centre of each segment. The ICA parameter indicates the change in the transient signal magnitudes as a function of xy interaction position. In order to calculate how the ICA changes with azimuthal angle a quantitative measurement of the ICA was made by tracing a 20 mm radius around the ICA spectra from the centre of Segment A1. The measurement of the ICA as a function of azimuthal angle is shown in Fig. 4.19.

The ICA parameter calculation has a large gradient through each sectors of the detector, showing the high sensitivity of the transient signal in azimuthal angle. This sensitivity of the transient signal magnitudes is vital to pulse shape analysis

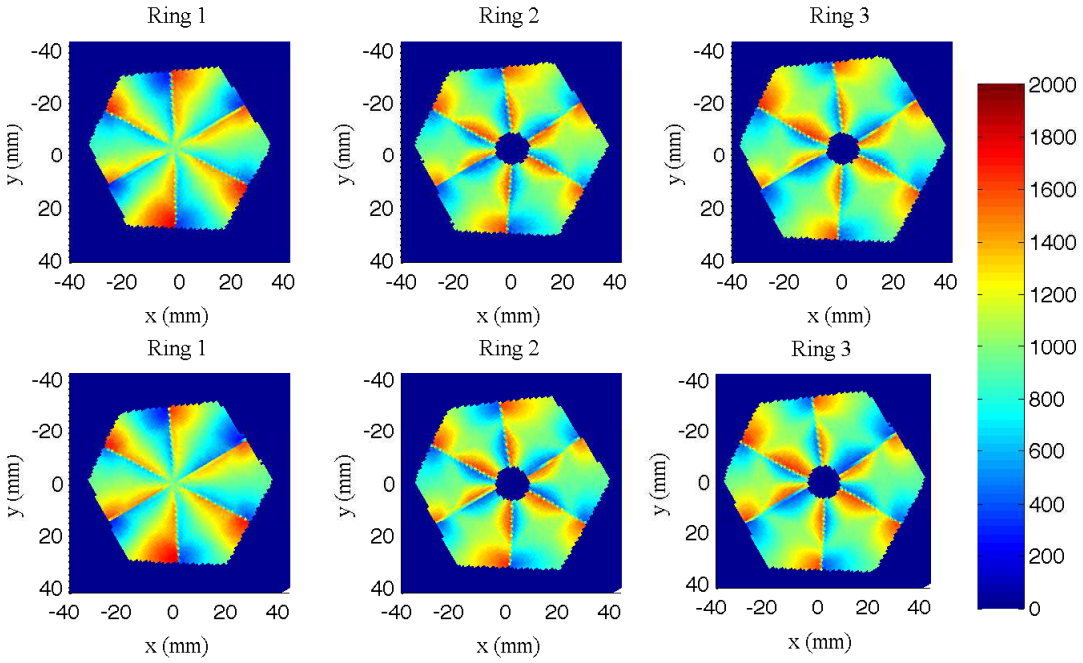

Figure 4.18: A004 rings 1-3 (top), A006 rings 1-3 (bottom). The image charge asymmetry clockwise and counterclockwise for rings 1-3. The colour scale is in arbitrary units. It can be noted that the transient signal sensitivity is the same for both detectors due to the identical segmentation.

The Ring 1 calculation shows a linear relationship between ICA and azimuthal angle, indicating that the response is linear in the area where the field is planar in configuration. The Rings 2 and 3 ICA indicates that in the coaxial region of the detector the response is slightly non-linear throughout the segments in that region of the detector. The ICA of both detectors A004 and A006 show a good agreement with respect to the transient charge sensitivity.

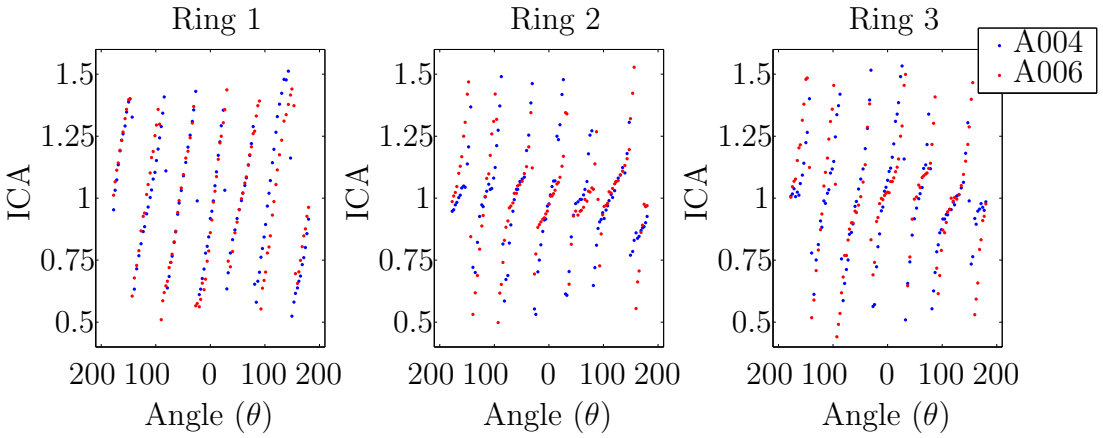

Figure 4.19: The image charge asymmetry as a function of azimuthal angle at radius = 20 mm. Each line represents the response through individual segments.

4.5 Signal Shape Risetime

The *risetime* refers to a measurement of the time it takes for the preamplifier signal to rise to a proportion of the maximum amplitude. It is useful to quantify the charge collection process for pulse shape analysis in this way to investigate details of the electron and hole collection process.

The T30 is the time required for the signal to rise from 10 % to 30 % of its maximum, the T90 is from 10 % to 90 % of its maximum:

$$\mathrm{T30} = \mathrm{t(30\%pulse)} - \mathrm{t(10\%pulse)} \tag{4.2}$$

$$\mathrm{T90} = \mathrm{t(90\%pulse)} - \mathrm{t(10\%pulse)} \tag{4.3}$$

The detector can be investigated based on the variation in signal shape across the bulk depletion region by using the risetime parameters. These risetime parameters are an essential ingredient for pulse shape analysis. The values given for the singles scan average over the depth of each segment per position.

The core and segment risetime maps quantify the charge collection of the detector using the same segment Fold-1 and 662 ± 2 keV energy gates used on the intensity matrices. The risetime values calculated are an average from all the events occurring at each xy position. A lower threshold of 20 counts per position was set in MTSort such that statistically insignificant counts were eliminated in the risetime calculation.

4.5.1 Core Risetime

The core T30 and T90 maps for Rings 1-3 are shown in Fig. 4.20. The core T30 maps show the dependance of electron and hole drift time with radial interaction position. The charge collection time increases as a function of interaction position with increasing distance from the core electrode, due to the increasing drift distance of the electron-hole pairs to the core.

The longest T30 risetime occurs at the detector corners which are furthest from the core electrode. There is a four fold symmetry in the T30 core maps which indicates the crystallographic axis. The T30 risetime dependance on the crystal axis is due to the anisotropic drift velocity discussed in detail in Section 3.3.1. A measurement of the crystallographic axis direction for the core T30 maps is performed in Section 4.6.

The core T90 maps illustrate the combination of electron and hole transport. Minimum charge collection time occurs at equal distance to the core and segment electrodes. Longer charge collection times occurs near the core and corners of the crystal The A004 T90 values are slightly longer than the A006 T90 across each ring. This indicates that the charge collection is slower towards the end of the collection. The radial variation in the T90 measurement indicates the effect of the weighting field on the charge collection. The initial charge near the segment electrode is collected quickly (T30), but the total charge collection (T90) is then slowed as the holes are collected at the longer distance at the segment electrodes. The four fold symmetry of the crystallographic axis observed in the T30 maps is also present in the T90 maps.

In order to compare the core risetime for every ring of each detector profiles are made from a cut through the centre of each ring, given in Fig. 4.21 for both the T30 and T90 risetime. The risetime is quantified for the T30 (lower risetime values) and T90 (greater risetime values) for both detectors.

These profiles are generated by making a cut along the central region of matrices with constant Y. The profiles show that the core risetime response of the detectors nearly identical. The radial dependance of the T30 risetime is clearly observed. The T90 charge collection time for A004 is slightly longer than for A006 indicating that there is a slight difference in the average charge collection time. The profiles for Rings 2-5 indicate the bore hole width of detector A004 and A006.

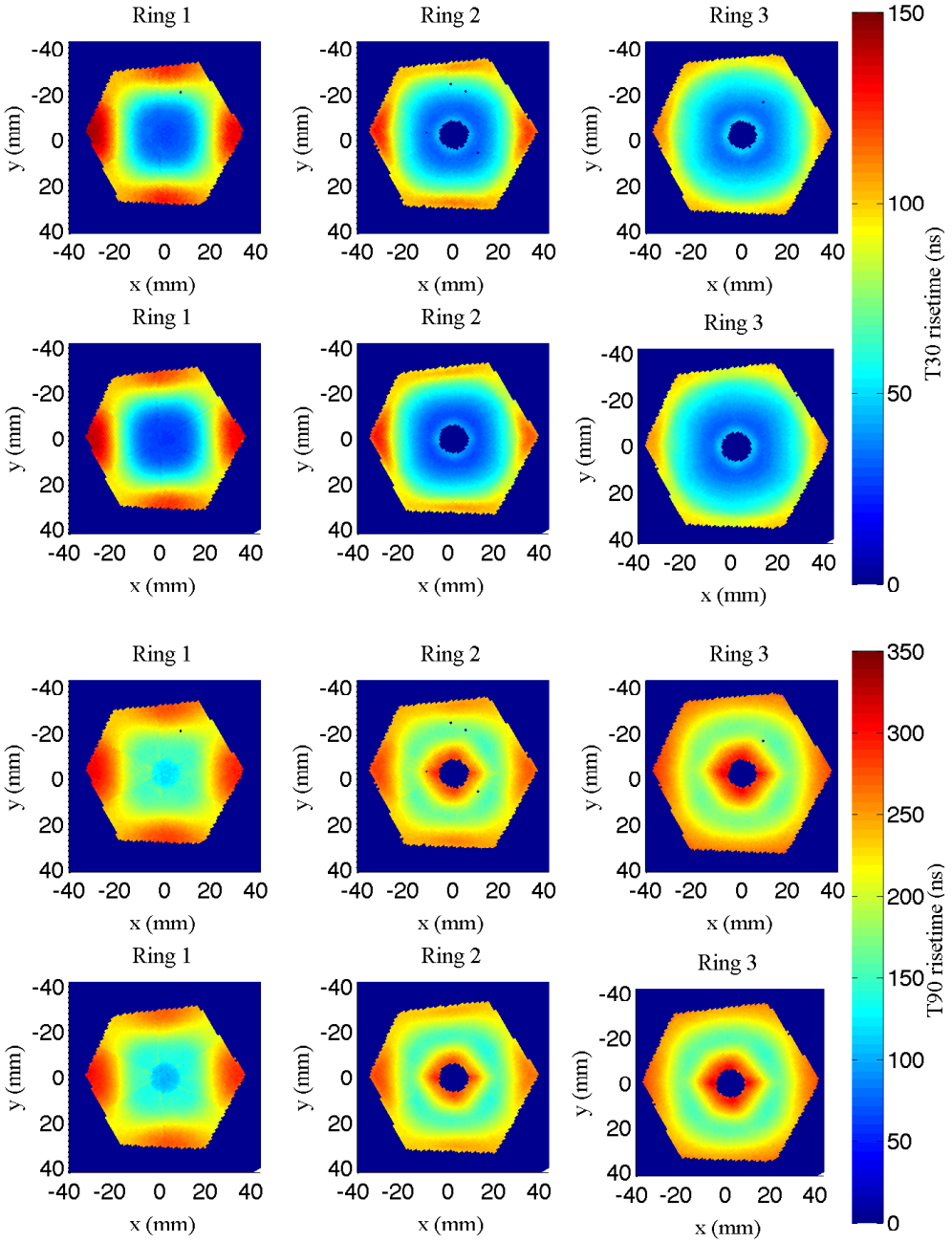

Figure 4.20: The average core T30 (top) and T90(bottom) for detectors A004 and A006 rings 1-3. From the T30 image the 4 fold symmetry of the charge risetime is obvious between the core and edge of the rings. Within the T90 risetime spectra, the central minimum is observed such that the electrons and holes have similar distances to travel during the later part of charge collection. Rings 1-3 are shown here in order to more clearly compare the detector. The full plot of these value over every ring is given in Appendix A.

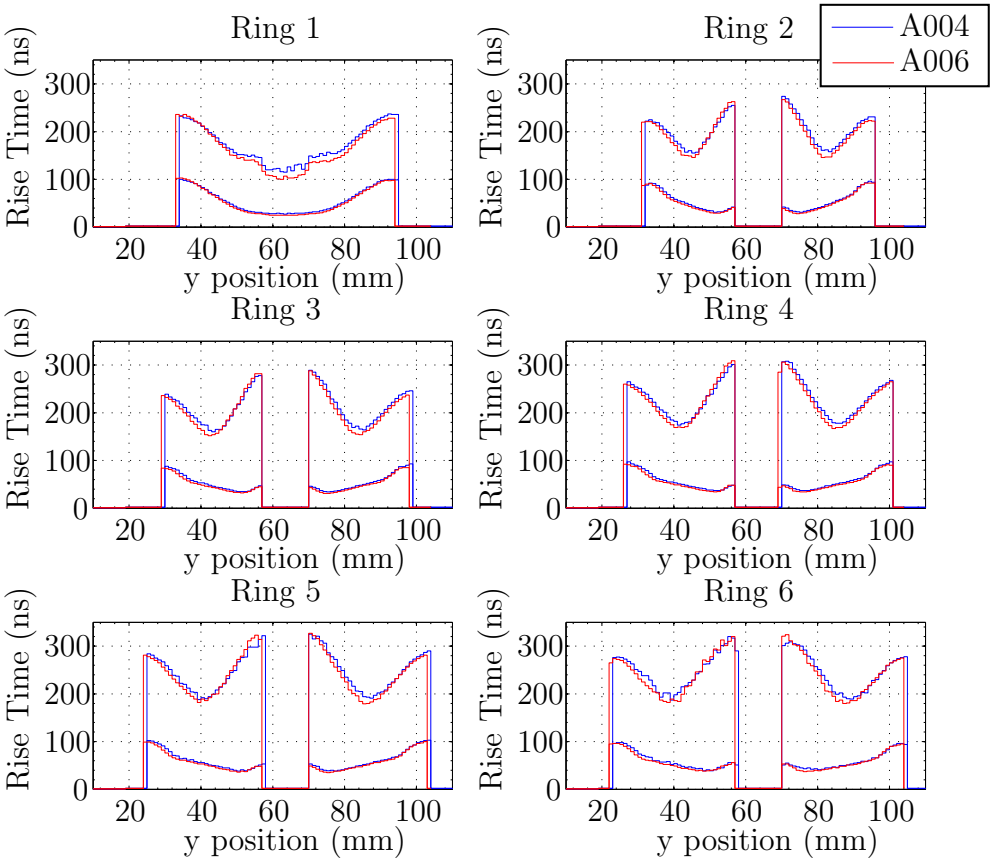

Figure 4.21: The profiles of the *core* risetime T30 and T90 risetimes of detectors A004 and A006. These profiles are generated by making a cut along the central region of risetime matrices. See figures in Appendix A. From the profiles it can be observed that the detectors behave in a very similar way. The A004 T90 risetime is, however, slightly longer than A006.

4.5.2 Segment Risetime

The hole collection process can be studied by examining segment electrode T30 and T90 risetimes produced by the preamplifier signals. The segment risetime maps for rings 1-3 are shown in Fig. 4.22. The dominant feature of the segment risetime maps is the 6 fold segmentation of the rings. There is also a very clear distinction between the risetime of Ring 1 and the other rings.

In the T30 maps for both A004 and A006, the Ring 1 maps show fast initial charge collection. The Ring 1 segment T90 maps indicate the segmentation as skewed borders. Also clear in the segment T90 maps is the four fold crystallographic axis. The behaviour of the Ring 1 maps is the result of the difference in electrode configuration and therefore charge collection in Ring 1 segments which starts off very steep in ring one due to the small distance to the segment electrodes. The T90 Ring 1 maps indicate that the crystallographic axis has noticeable effect on the hole charge collection within Ring 1.

The T30 rings 2 and 3 show a radial dependance of the T30 as it decreases from the central region toward the segment electrodes. The segment T90 risetime maps shows the combination of electron and hole transport similarly to the core T90 maps. The shortest hole charge collection is observed in the central region of the segments, with longer T90 risetime values in the centre of the rings and towards the outer detector corners.

These segment risetime maps generated for both A004 and A006 show a good agreement. In order to compare the segment risetime directly, profiles of the risetime maps are made from a cut through the centre of each ring and given in Fig. 4.23 for both the T30 and T90 risetime.

Ring 1 shows the uniform T30 risetime across the detectors. From the segment T30 risetime indicated in Fig.4.23, the inverse radial dependance on the risetime is shown than that calculated for the core T30 risetime as shown in Fig. 4.21. The T30 decreases with radius. The A004 T90 core risetime was slightly longer than that of A006, whereas the segment T90 is shorter. This indicates a difference in the segment response of each detector, but has not been investigated in more detail.

Both Fig. 4.20 and Fig. 4.22 show that for Rings 1-3 there is good agreement between detector A004 and A006 of the T30 and T90 risetime calculation. The additional T30 and T90 risetime maps for the core and segment contacts for all rings are included in Appendix A.

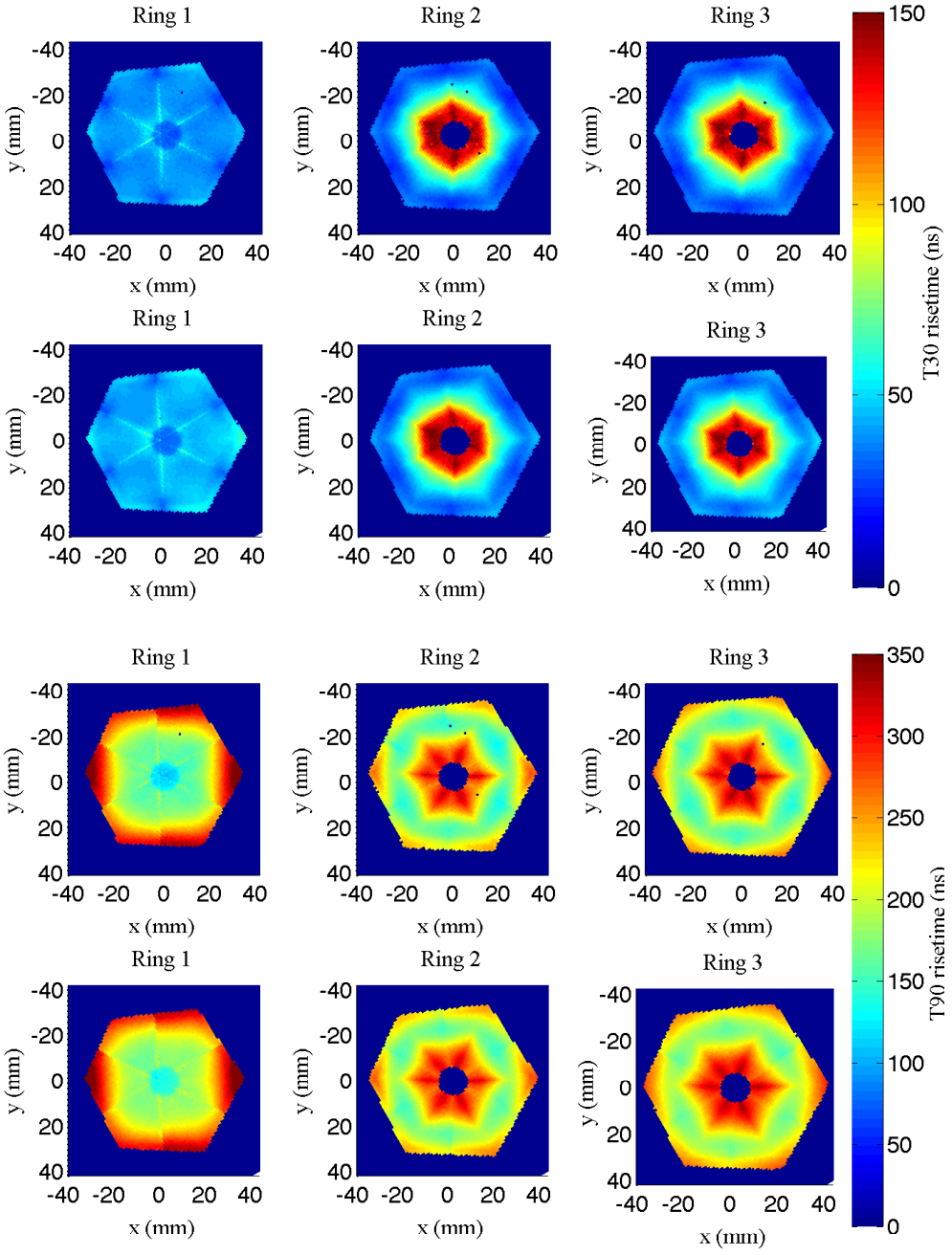

Figure 4.22: The average segment T30 (top) and T90 (bottom) for detectors A004 and A006 rings 1-3. Rings 1-3 are shown here in order to more clearly compare the detectors. The full plot of these values over every ring is given in Appendix A.

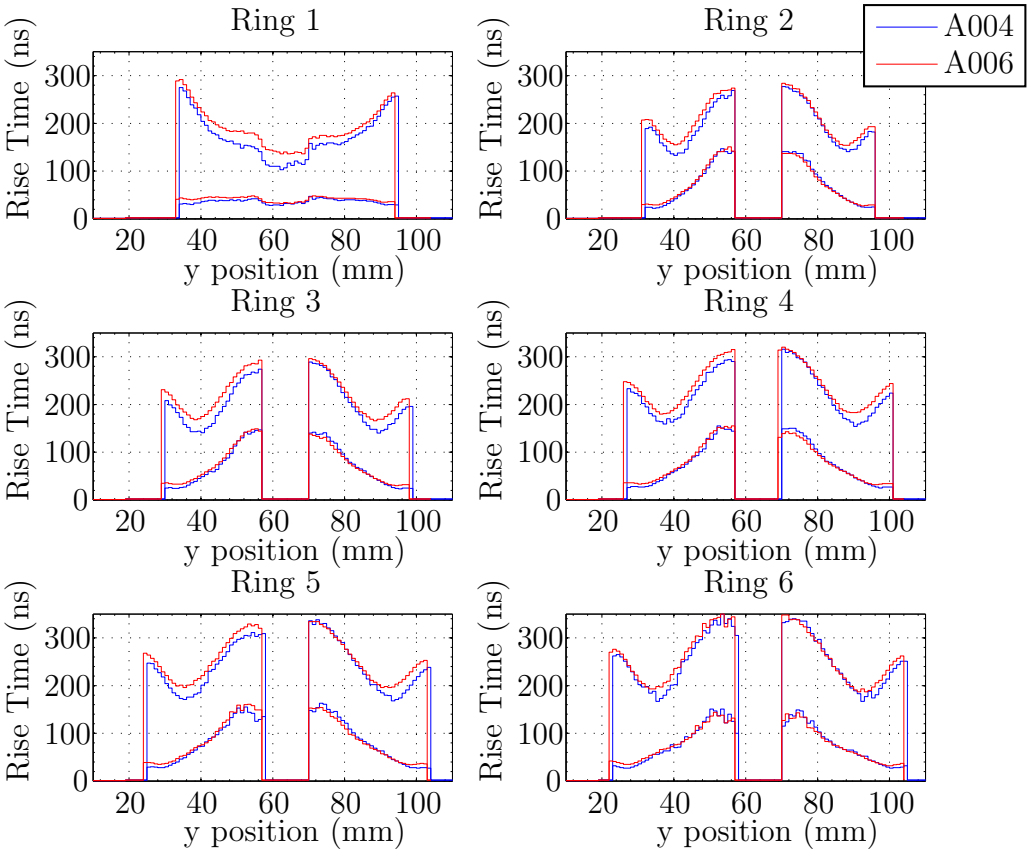

Figure 4.23: The profiles of the *segment* T30 and T90 risetimes of detectors A004 and A006. These profiles are generated by making a cut along the central region of risetime matrices. See figures in Appendix A. From the profiles it can be observed that the detectors behave in a very similar way. The T90 charge collection time for A004 is slightly longer than for A006 indicating that there is a slight difference in the average segment charge collection time.

4.6 Crystallographic Axis Calculation

The crystallographic axis direction can be calculated from the ^{137}Cs T30 risetime matrices. The four fold symmetry on the T30 maps due to the crystal lattice is shown in Fig. 4.20. Electrons and holes travel fastest along the $\langle 100 \rangle$ direction as discussed in Section 3.3.1. The charge collection velocity anisotropy with respect to axis direction becomes apparent when examining the ^{137}Cs T30 rings. The crystal axis can be measured by tracing a circle around each of the detector rings, shown in Fig. 4.24.

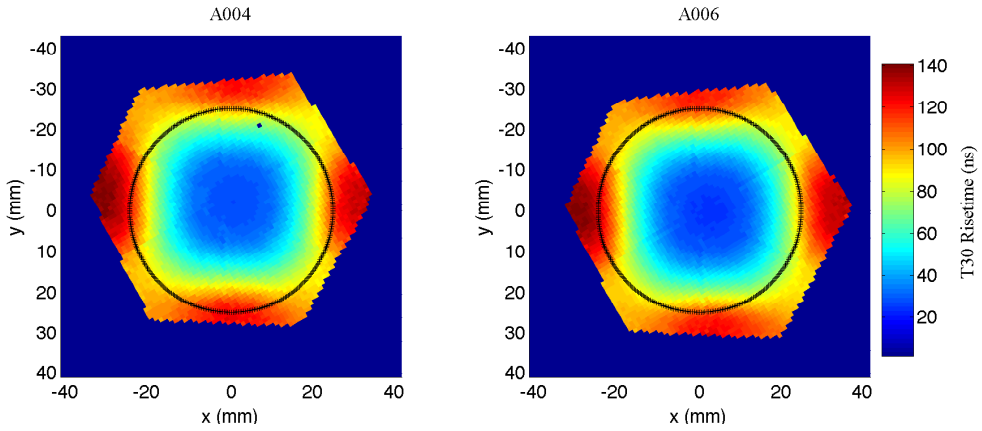

Figure 4.24: The front ring T30 plots for both the ^{137}Cs scans for detectors A004 and A006.

The risetime maps generated from the ^{137}Cs scan are the result of Fold-1 events in each segment. For a 662 keV γ-ray, the photon energy will most commonly be from multiple interactions due to Compton scattering. The crystal axis calculation will therefore not indicate the precise response of the detector in the ^{137}Cs measurement.

4.6.1 The ^{241}Am Front Face Scan

The A006 ^{241}Am scan is also used to determine the crystal axis. The photopeak gated Fold-1 position intensity are generated from the MWD spectra for this scan as well. Only the Ring 1 spectra show significant events from the ^{241}Am scan due to absorption of the lower energy γ-ray (60 keV). The position intensity generated from the ^{241}Am scan is shown in Fig. 4.25.

The position spectra generated from the A006 ^{241}Am scan are gated on the 60 keV photon energy. An additional feature observed are the regular

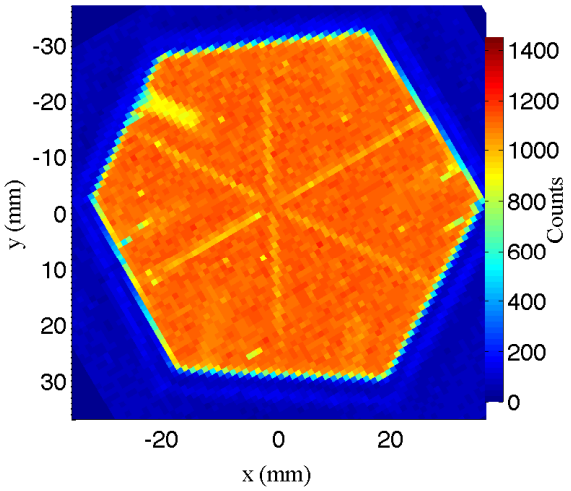

Figure 4.25: The position intensity of the ^{241}Am scan of capsule A006. This spectrum is gated on Fold-1, 60 ± 2 keV events.

rectangular features in each segment within the ring one position intensity. This is observed due to the absorption of the 60 keV γ-rays within the A006 capsule. It has been determined that this feature indicated a spacer between the crystal front face and encapsulation material.

T30 and T90 risetime maps can be produced for the ^{241}Am scan from the baseline difference calculation in the same way as well, shown in Fig. 4.26.

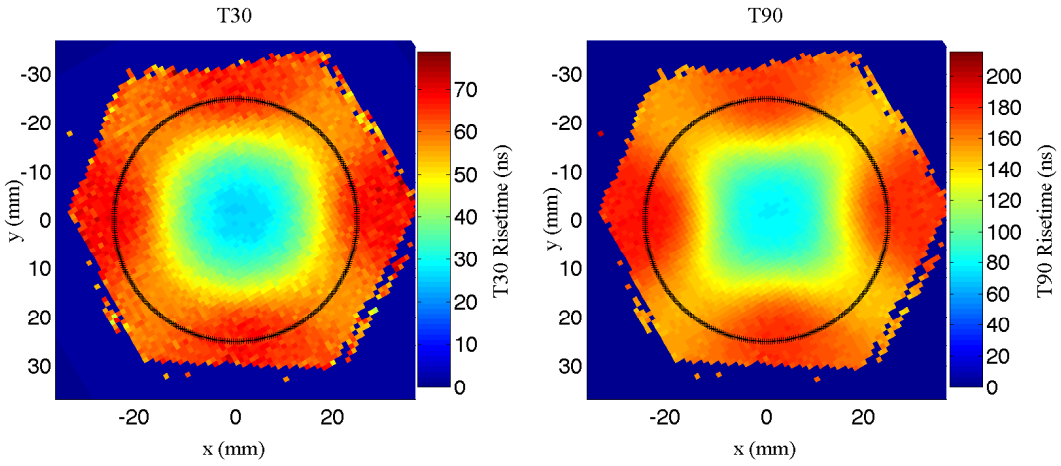

Figure 4.26: The T30 (left) and T90 (right) risetime maps generated from the ^{241}Am scan.

The ^{241}Am scan is useful due to the complete deposition of energy for the low energy γ-rays in ring 1. At 60 keV photoelectric absorption is the domi-

nant interaction process of photons within germanium as described in Fig. 2.1. Compton scattering, which leads to uncertainty in the ^{137}Cs measurement does not affect the ^{241}Am results. The spectra generated from this scan are the result of single site interactions, resulting in the uniform position intensity detector response. Both the T30 and T90 risetime are useful for the crystallographic axis calculation. The ^{241}Am T30 and T90 risetime maps for A006 Ring 1 show the same pattern of risetime as observed in the ^{137}Cs A006 Ring 1 map.

4.6.2 Crystal Axis Orientation Results

The crystal axis is measured quantitatively by plotting the T30 risetime as a function of azimuthal angle for 360 degrees as shown in Fig. 4.27. The crystal axis for crystals A004 and A006 show good agreement for the direction of the $\langle 100 \rangle$ axis. The A006 measurements on both the ^{137}Cs and ^{241}Am spectra show agreement with the curve maxima and minima. The T90 measurement shows a smooth curve indicating the strong effect of the crystal axis on the charge collection of the 60 keV γ-ray. The lower γ-ray energy in the ^{241}Am scan results that the spectra from this scan are more susceptible to noise effects indicated in the T30 risetime distribution.

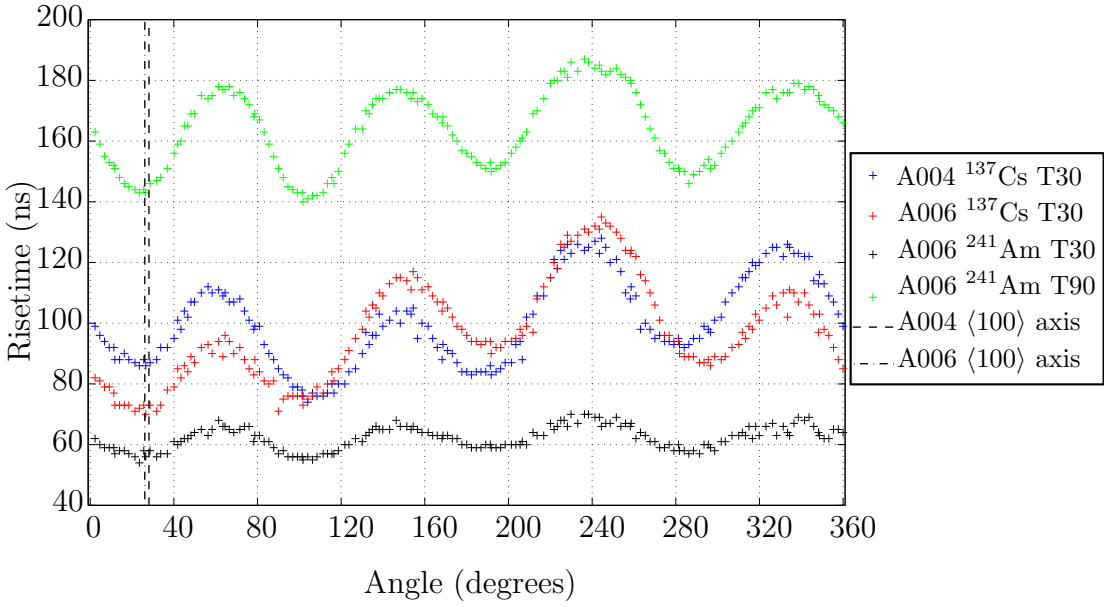

Figure 4.27: The crystallographic axis calculation for the A004 and A006 ^{137}Cs and the A006 ^{241}Am risetime measurements. The fast $\langle 100 \rangle$ axis is indicated along the minimum. The slow $\langle 110 \rangle$ axis lies along the maximum.

The agreement with the manufacturer, Canberra, is that the fast $\langle 100 \rangle$ axis direction lies along the corner of sector A (the centre of the triplet) with an accuracy of $\pm$ 3 degrees [35]. The sector A corner is at the centre right of the T30 risetime profiles (see Fig. 4.11 for sector orientation). The results shown in Fig. 4.27 indicate offsets of 25 and 27 degrees from corner A for capsule A004 and A006, respectively.

The fastest risetime occurs at the 25 and 27 degree angles, which is in the $\langle 100 \rangle$ axis direction. The slowest risetime occurs in the $\langle 111 \rangle$ axis direction which is offset from the $\langle 100 \rangle$ by 30 degrees. Although detector crystals A004 and A006 are closely matched, they do not agree with the specification.

4.7 Reduced Bias Voltage Scans

Photon scans were made at voltages less than the operating voltage (+ 5000 V) in order to study the detector performance at these reduced voltages using the 137Cs source. These scans were performed for a shorter time per position, 30 s, and on a 2 mm xy grid in order to acquire data more rapidly, reducing the collection time from ∼4 days for full bias to ∼20 hours acquisition time. The scans are useful for determining the rate at which the depletion surface (the detection region) grows as applied bias voltage is increased. Also studied in detail is the change in energy resolution and shift in peak position (gain) at reduced bias voltages. The energy resolution and peak shift are indicators of detector performance.

Detector A004 was scanned with 8 reduced bias voltage values. Detector A006 was scanned with 10 reduced bias voltage values. As the bias voltage decreased the preamplifier signal amplitude decreased such that the CFD threshold was lowered for each bias. To produce the reduced bias intensity matrices the core MWD energy gate had to be adjusted for each bias voltage. The effects of the bias voltage on the photo peak centroid position are discussed in Section 4.7.2.

In order to present uniform data for the depiction of the depletion surface growth a coaxial part of the detector, Ring 4, is plotted in Fig. 4.28 and Fig. 4.29 for all voltages. The active area of the detector at each voltage is indicated by an intensity of counts greater than ∼200 counts per position. At very low voltages (50 - 250 V) the outer ring of the detector is slightly depleted. This depletion at the pn-junction is discussed within Section 3.2.2. As the voltage is increased the sensitive region also grows, dependant upon Equation 3.5 where the depletion depth is proportional to the voltage, as described in Equation 3.8. The detector is most sensitive to changes in voltage at lower biases (from 0 to + 2000 V). At + 3000 V the detector is nearly completely depleted through its volume. The intensity, however, is lower due to the lack of electric field uniformity throughout the volume at the lower voltages.

A measurement of the proportion of the detector depleted at each voltage for each ring is made in the next section, Section 4.7.1. The performance of the detector at the voltage between + 50 and + 5000 V is studied in Section 4.7.2.

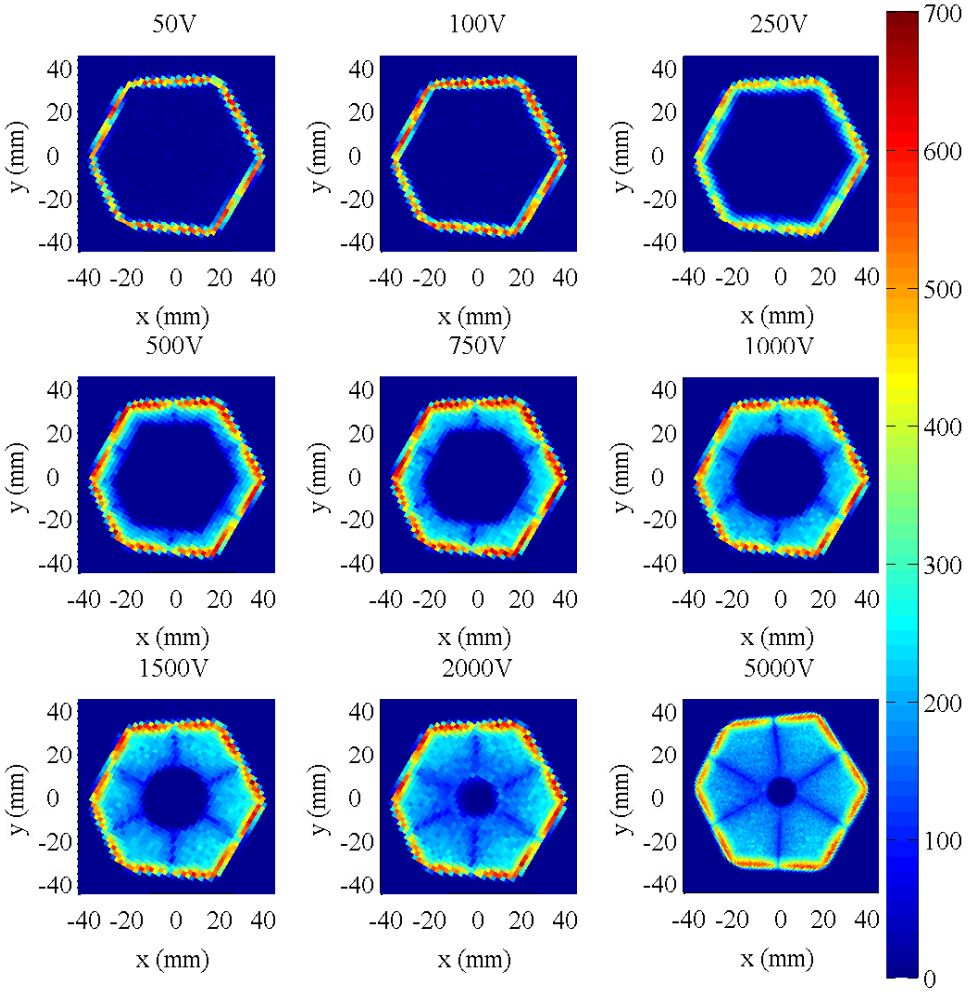

Figure 4.28: Intensity matrices for the A004 detector at full bias and reduced bias voltages gated on segment Fold-1 events and ^{137}Cs 662 keV photo peak energy. The key feature of these images is the growth of the depletion region from the outer contact to the core at this depth.

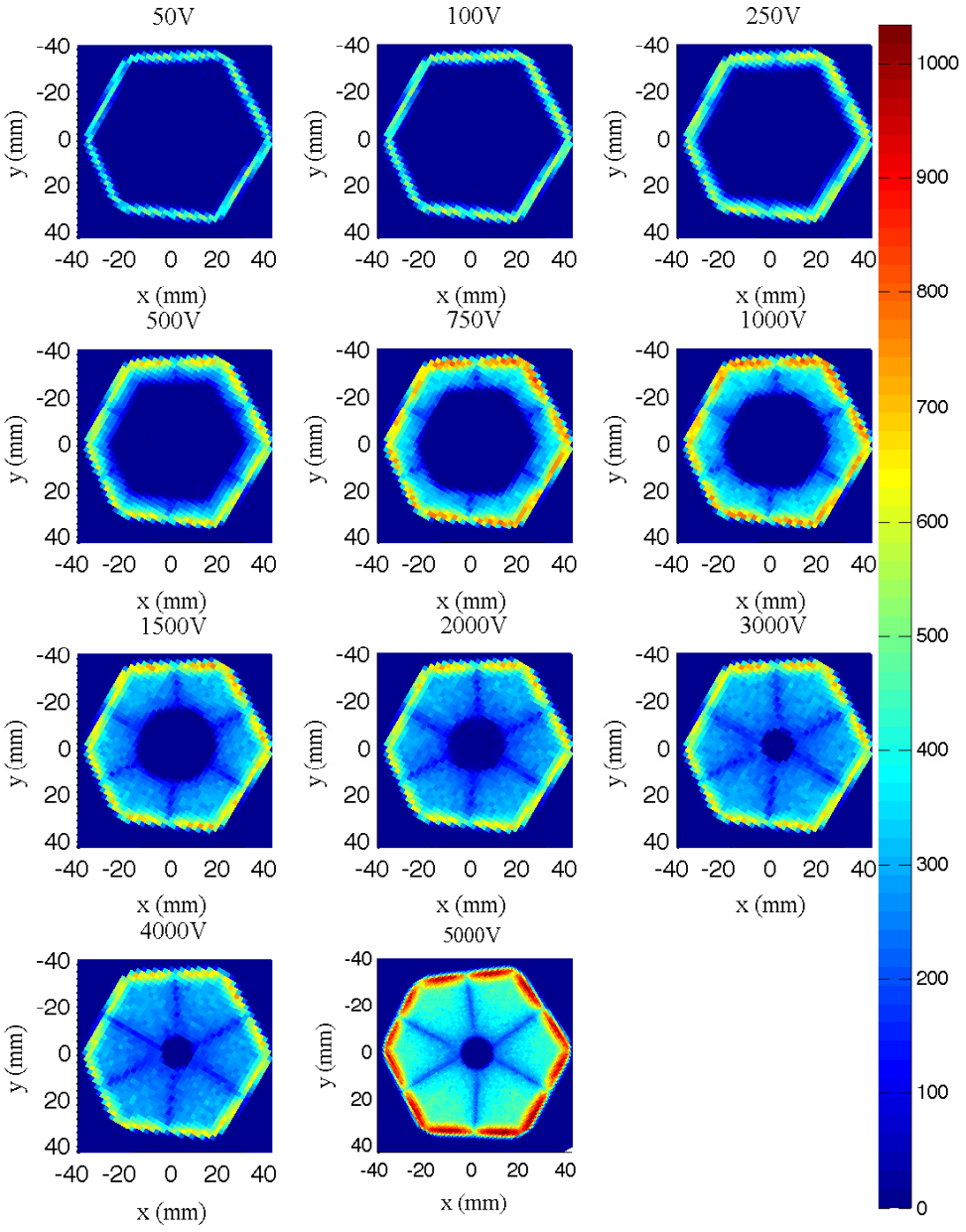

Figure 4.29: Intensity matrices for the A006 detector at full bias and reduced bias voltages gated on segment Fold-1 events and ^{137}Cs 662 keV photo peak energy. The key feature of these images is the growth of the depletion region from the outer contact to the core. Also apparent at a bias of 3000 V the detector is nearly totally depleted at this depth.

4.7.1 Depletion Depth by Voltage

The detector depletion as a function of bias voltage is studied for detectors A004 and A006. The area of depletion is calculated from the position intensity maps for Ring 4 shown in Fig. 4.28 and 4.29. Each position with an intensity above a lower threshold (30 counts) is summed and divided by the full bias depleted position to take a proportion of depletion measurement. This yields the proportion of Ring 4 for each voltage which is depleted, plotted in Fig. 4.30.

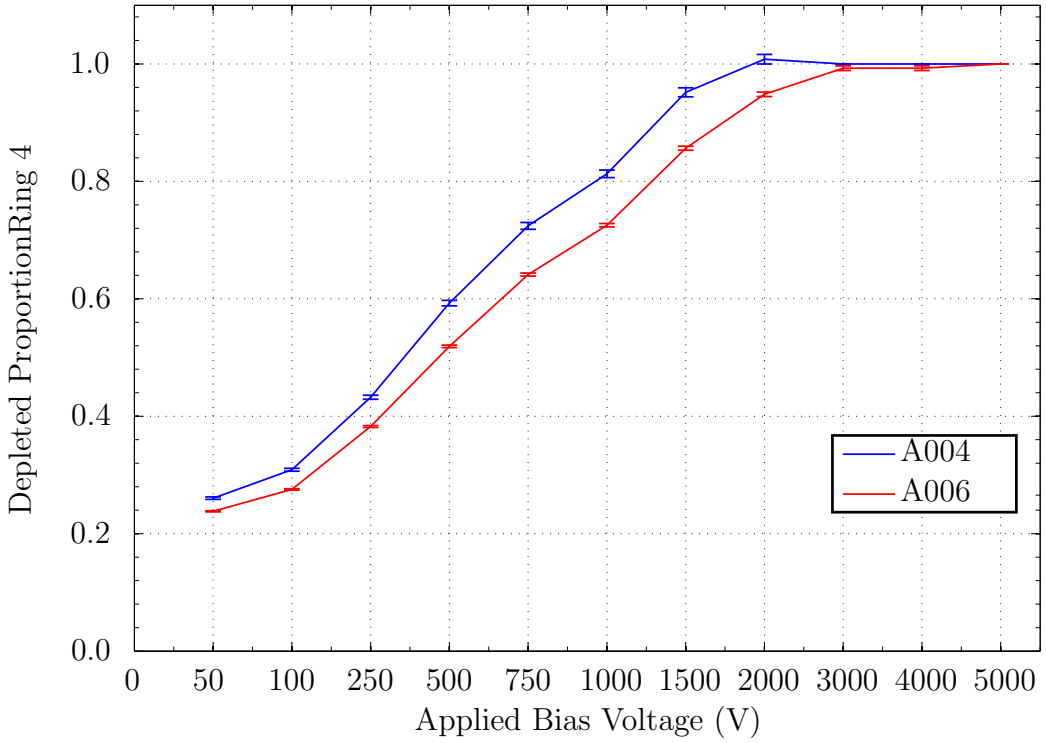

Figure 4.30: The proportion of depleted surface for reduced bias voltages in Ring 4. Capsule A004 is fully depleted at 2000 V, whereas capsule A006 is fully depleted at 3000 V.

From this plot it can be observed that capsule A004 depletes more readily than detector A006. From this ratio calculation, A004 is fully depleted in Ring 4 at 2000 V. Capsule A006 is fully depleted at 3000 V. This is due to the lower impurity concentration of A004, described in Section 4.1.2.

4.7.2 Energy Resolution and Centroid at Reduced Bias

The energy resolution and peak shift measurements were made on the A004 and A006 MWD energy spectra data sets within Fig. 4.31 and Fig. 4.32. The spectra were gain matched at the full bias voltage with ^{152}Eu, ^{241}Am and ^{56}Co sources. The 662 keV ^{60}Co peak measurements were made using a Gaussian fitting routine from MATLAB that produces the centroid position, peak area and FWHM measurement for all segments. Due to the volume of spectra to be fitted it was necessary to automate this process.

The photopeak centroid shift at reduced biases for both A004 and A006 are shown in the plots, Fig. 4.31. The centroid of the peaks shifts to lower values with the reduced applied bias voltage values. The centroid shift is also dependent on the segment location within the crystal. The A004 spectra show a very large shift in Segment E4, attributed to a faulty segment connection. The segments in ring 6 at the back of the detector (Table 4.1), show the greatest shift. Conversely, the segments in ring 1 at the front of the detector shift the least amount. The volume of the back ring segments is larger and therefore less depleted as the bias voltage is reduced. With less depletion, less charge carriers will be collected at the cathodes as the gain is reduced at lower bias voltages.

The energy resolution as a function of bias voltage is also plotted, Fig. 4.32. The digital energy resolution follows the trend of the analogue resolution, discussed in detail in Section 4.2.1. The energy resolution degrades at lower bias voltages. In general the FWHM degrades more at the back of the detector as the voltage is lowered due to the larger detector diameter. Larger volumes of these segments require higher voltages to deplete fully. The un-depleted volumes yields poorer resolution in the back segments. From the measurements of A006 at the voltages + 3000 V and + 4000 V the resolution does not degrade greatly at the reduced bias voltages.

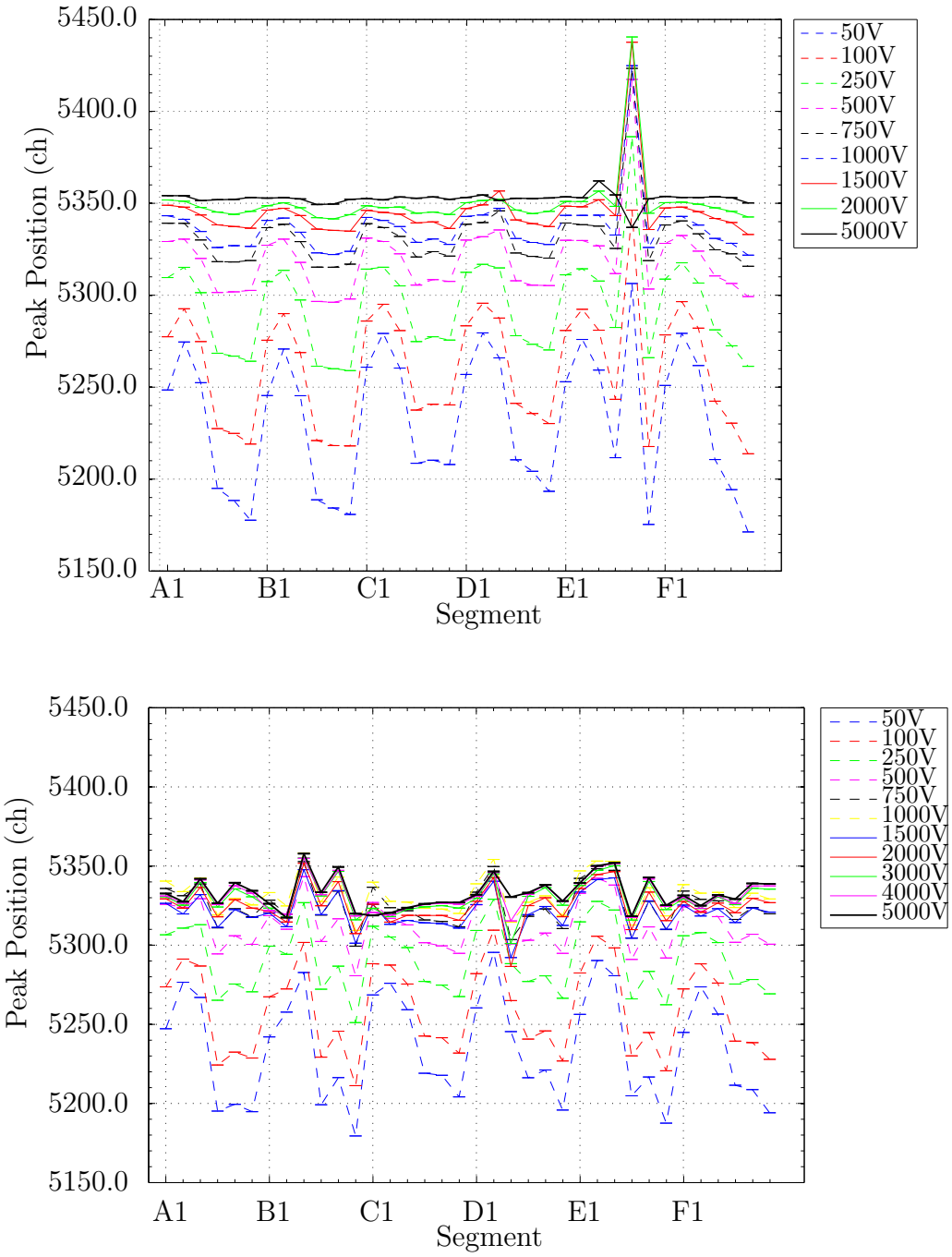

Figure 4.31: A004 (top) and A006 (bottom) photopeak centroid shifts at reduced bias voltages. Both detectors are sensitive to the reduction of the bias. The A004 spectra show a large shift in Segment E4, attributed to a faulty segment connection.

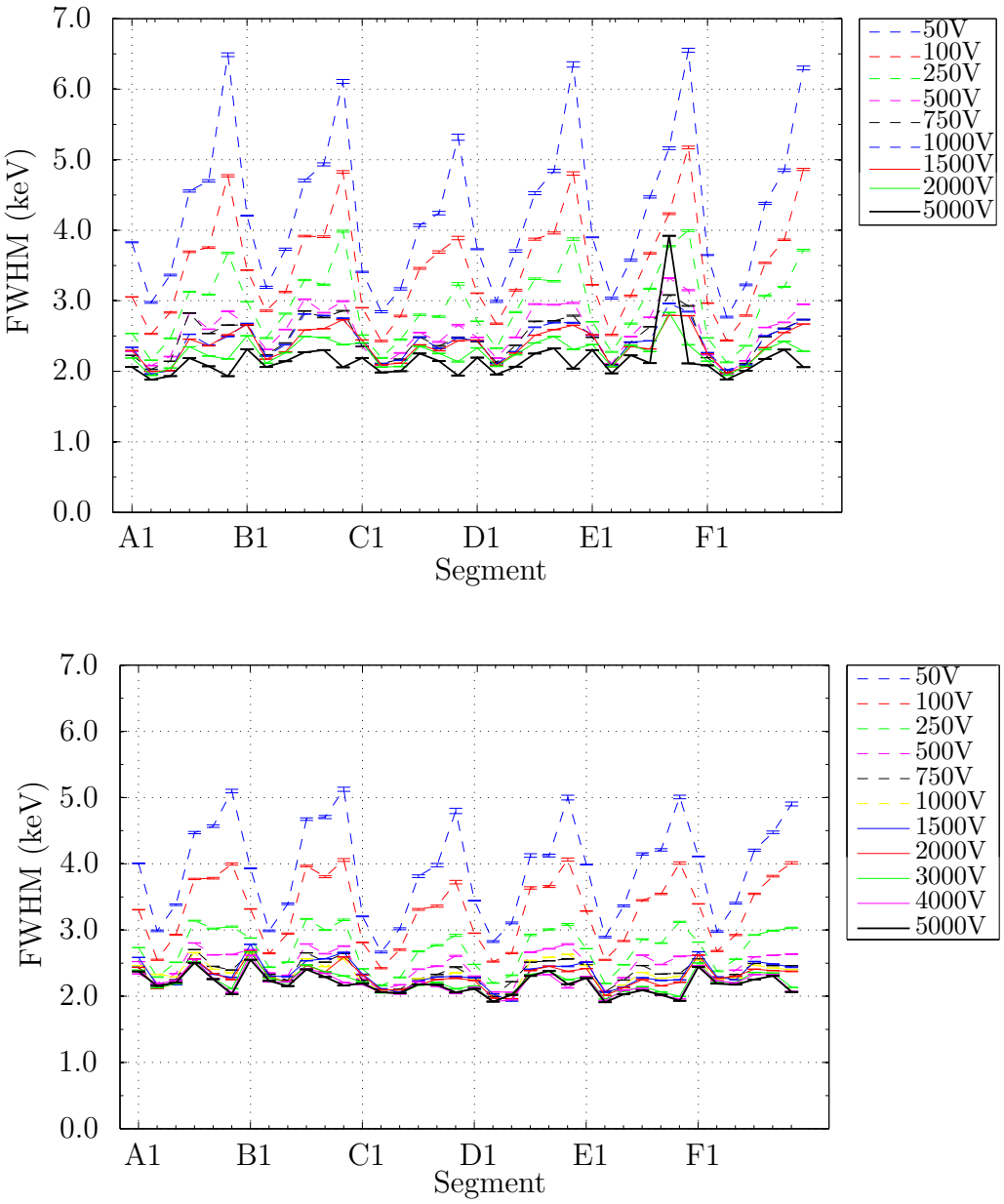

Figure 4.32: A004 (top) and A006 (bottom) energy resolution degradation at reduced bias voltages. At very low bias voltages it is clear that the energy resolution is highly effected. At bias values of 3000 V and up, the resolution is not strongly affected.

4.8 Side Scans

Upon the completion of front face scanning, each capsule was scanned on its side along the length of the detector using the ^{137}Cs source. The test cryostat was removed from the large LN_2 storage dewar and mounted on its side. The detector was scanned on a 1 mm x 1 mm xz grid similar to the front face scan. The detector was scanned for ∼8000 positions due to the larger surface area scanned by the source. The same trigger signal was used for the data acquisition as with the front face scan. This procedure was somewhat more delicate due to the basic mount for the side positioning. The detector was also filled every 8 hours in this configuration as it was not mounted to the liquid nitrogen storage dewar.

A photograph of detector A006 mounted within the test cryostat positioned on its side over the scanning table is shown in Fig. 4.33(a). The detector segmentation positioning over the scanning table is also indicated on the right with the coordinates of the scanning table indicated.

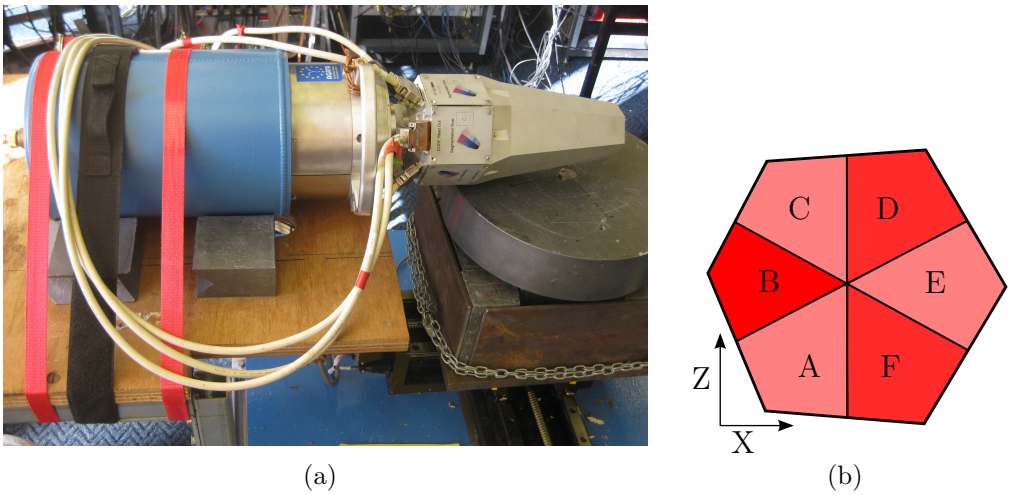

(a) (b)

Figure 4.33: The single crystal cryostat mounted on its side above the collimator of the scanning table (a). Figure (b) indicates the orientation of the detector segments to the scanning table coordinate system.

The detector was mounted such that the A/F segmentation boundary was located closest to the scanning table. The full bias un-gated intensity matrix with all accepted events is depicted in Fig. 4.34 (left). The outline of the detector can be observed as well as the asymmetry along either side of the detector. The side scan was also gated on the 662 keV photopeak energy in Fig. 4.34 (right). The areas of reduced intensity indicate the segment edges in

which the γ-ray scatters from the detector. The loss of intensity to the detector edges is radially dependant. The central bore hole is also visible.

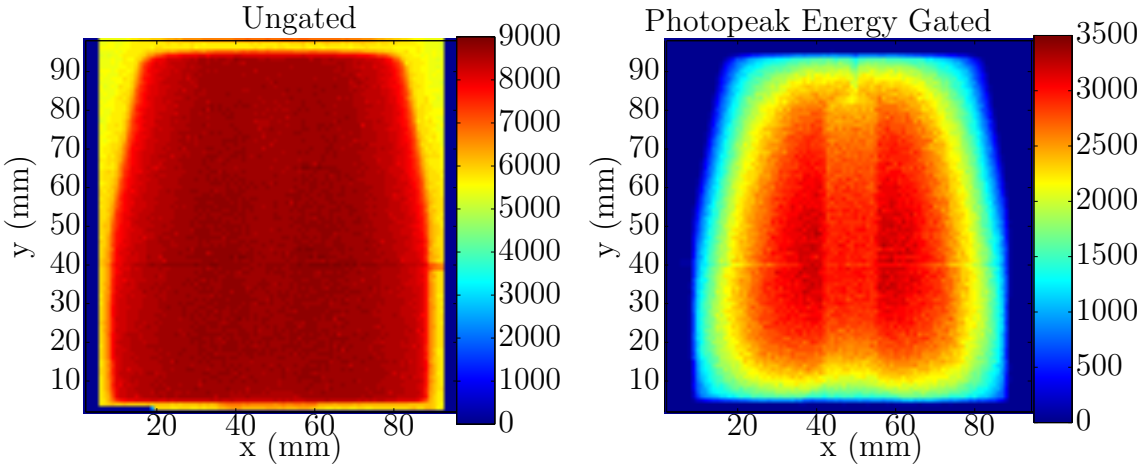

Figure 4.34: The full bias side scan position intensity matrices of detector A006. All accepted counts is shown in the un-gated spectra on the left. The 662 keV photopeak energy gated position intensity is shown on the right.

The energy spectra can be gated upon segment Fold-1 events and the 662 keV photopeak energy, shown in Fig. 4.35. The only sectors fully exposed to the photon beam are A and F and so the bulk of the crystal prevents a detailed observation of every segment.

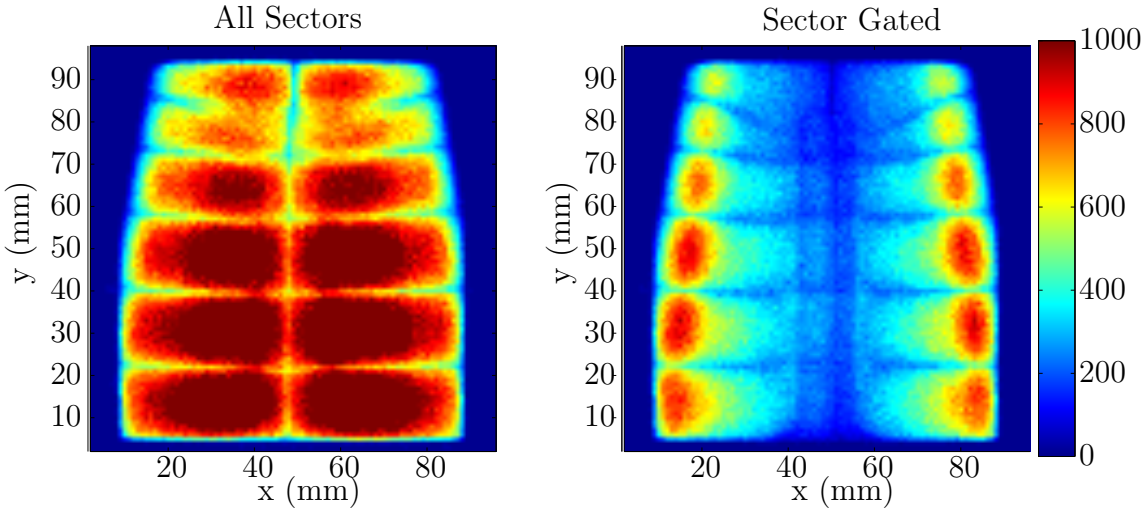

Figure 4.35: The Fold-1 662 keV photopeak gated full bias side scan, all detector sectors (right), BCDE sectors (left). The segmentation through depth is observed as well as the asymmetric shape. The sector gated spectrum shows a reduction of counts towards the central region, discussed in the text.

To reveal more detail of the detector at full and reduced bias voltages, only the back 4 sectors (B, C, D, E) were gated upon in the second image. This allows for an observation of the central detector volume. In the sector gated spectra a reduction of counts is observed as the 662 keV photons are absorbed in the central region of the detector with sectors A and F.

Detector A004 was also scanned on its side. However, the connection of Segment E4 was missing upon finishing the full bias side scan. For this reason the results for A004 are not used to describe detector performance in this section.

4.8.1 Reduced Bias Voltage Side Scans

Capsule A006 has been scanned on its side at reduced bias voltages. In order to study the depletion of the detector along the length of the detector as a function of voltage, several reduced bias scans were performed. In order to show the growth of the depletion region, these spectra are gated on the back 4 sectors. The spectra depicted in Fig. 4.36 show the growth of the depletion region from 100 V to full operating bias. The colour scale is chosen to show the outline of the fully depleted region of the detector. At 100 V the outer portion of the detector is depleted. As the bias voltage grows to 500 V the entire front ring is depleted. At 1000 V and 1500 V the depletion of the back two sectors is almost complete. At 5000 V the detector is fully depleted.

The proportion of the detector that is depleted has been calculated in the same way as for the front face scan. The result is shown in Fig. 4.37. The depletion proportion versus bias voltage agrees the measurement made on the front face reduced bias voltage scan. The range of voltages used in the reduced bias side scans was between 100 V and 1500 V, less than that used for the front face scan. This result indicates that at 500 V along the length of the detector nearly 90 % of the surface is depleted.

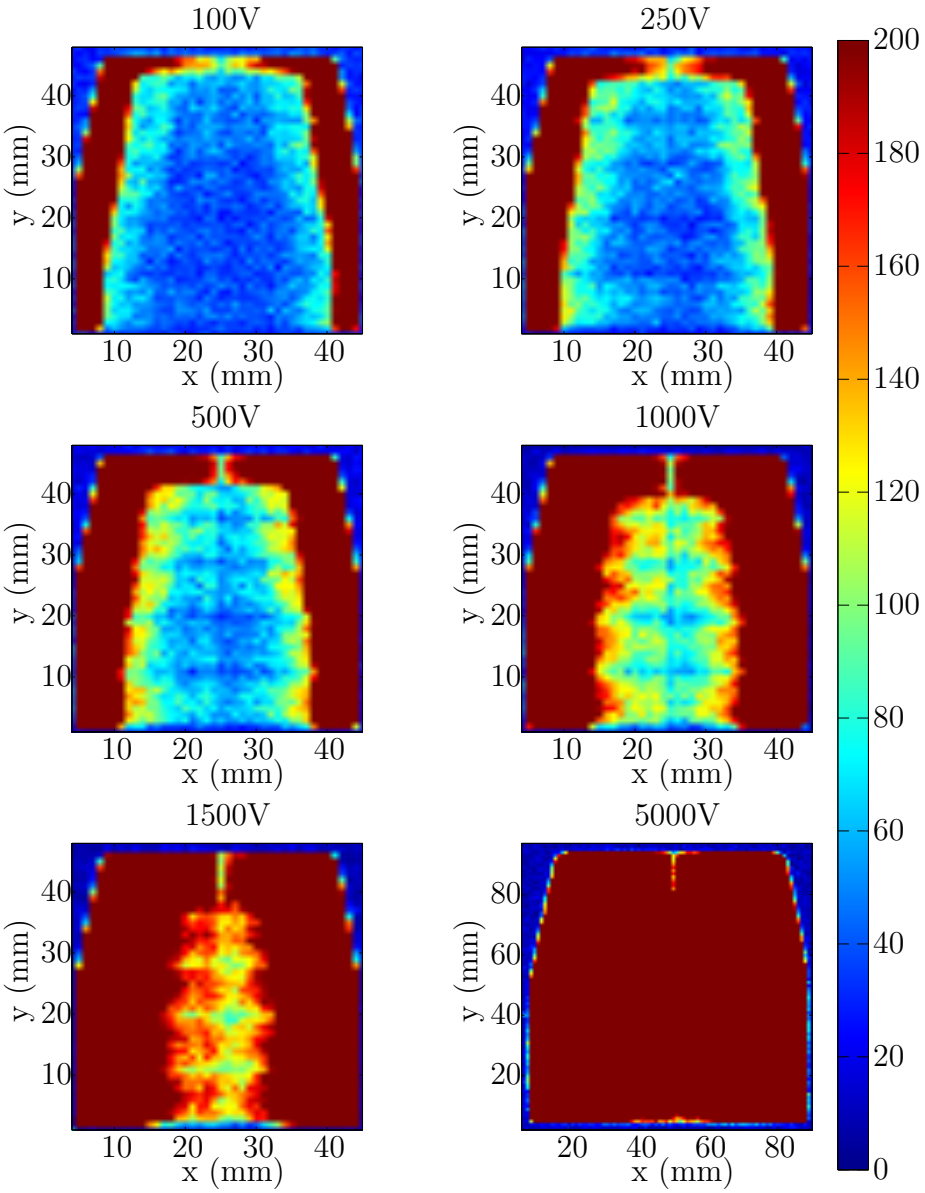

Figure 4.36: The reduced bias side scan of detector A006. The spectra are gated on the back rings to show the depletion surface. The evolution of the depletion region is clearly shown. The colour scheme has been chosen to view the growth of the depletion region.

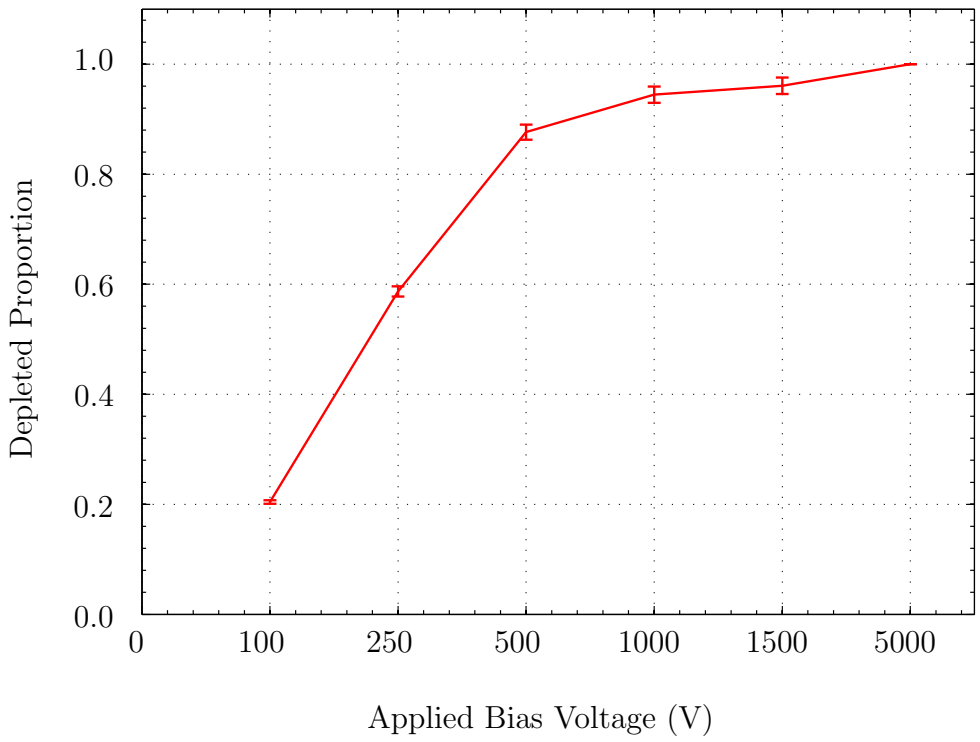

Figure 4.37: The proportion of depleted surface for reduced bias voltages as calculated for the sector gates (BCDE) position intensity in the A006 side scan).

Chapter 5

Simulated Detector Response Libraries

The ability to identify (within a few millimetres) the interaction positions of γ-rays within the AGATA detectors is made possible with pulse shape analysis (PSA). A database, or library, of the signals generated by each AGATA detector can be utilised to determine these interaction positions, as described in Section 1.3. The AGATA detector response has been simulated in order to build the pulse shape libraries.

An experimental pulse shape database can be used to verify the performance of the detector simulations. There are several ways to produce a database of signals from the volume of the crystal experimentally. Databases created through *coincidence scanning*, determine the response of a capsule to a γ-ray interaction at a specific x, y and z positions through the use of collimation and ancillary detectors for coincident photon measurements. Previously such experimental databases have been created for the symmetric prototype AGATA capsules as well as the asymmetric capsule C001 [42,49]. An experimental pulse shape database was generated for AGATA capsule A006 in this work, the process is discussed within Chapter 6.

A drawback of coincidence scanning is the lengthy time required to collect the data at a sufficient number of interaction positions throughout the crystal volume (several thousand). This process can take up to several months. An additional method of creating experimental database is the *Pulse Shape Comparison Scan* (PSCS) which requires the comparison of pulse shapes produced though the front and side *single scans* of the capsules [54]. In this way the entire detector response can be collected within the time it takes for two *singles*

scans (Section 4.3). Data was collected in this manner for detector C001 to verify the methodology. This method is new and has not been verified such that it can be used to generate the pulses for all of the crystals. New methods of scanning the detector at multiple positions have also been developed with the Orsay scanning system [13]. These new methods are in development at this stage and not used in this work.

5.1 AGATA Detector Simulations

The signal shape produced by the crystal depends upon the physical properties of each capsule as well as the interaction positions. There are three crystal shapes and each crystal can vary in impurity concentration. The signal shape produced is dependant upon these properties as well as the crystallographic axis angle. The large number of capsules intended for the AGATA demonstrator and full AGATA array requires an alternative method to produce this database of signal shapes for each capsule, which is done with simulations.

In order to verify the performance of the simulations a comparison between that and the experimentally generated database is performed, discussed in Section 6.5.

Several programmes are used to simulate the AGATA capsules in order to produce databases for experimental data analysis with PSA, including the Multi Geometry Simulation, MGS [55], the Java AGATA Signal Simulation, JASS [56], as well as the AGATA Detector Library (ADL) [57]. The MGS and JASS simulations have been previously compared with the experimentally generated databases produced through coincident scanning [42] [49]. The MGS simulation is limited by a fixed grid size calculation of the electric field. This limits the ability to calculate the field accurately near the electrodes where it is changing rapidly. The JASS simulation has been developed specifically for the AGATA geometry in which the user can specify the grid size. ADL, which has the flexibility of being used for multiple detector configurations as well a user specified step size for file calculation, will be compared with experimental A006 data in this work.

5.2 The AGATA Detector Library

The AGATA Detector Library (ADL), is a set of routines developed in order to characterise germanium detectors [57]. It has been developed by Bart Bruyneel and Benedikt Birkenbach at the Institut für Kernphysik der Universität in Cologne, Germany. ADL is written in standard C for the calculation of pulse shapes response. The simulation can be tailored for different geometries.

In this simulation, the electric field and weighting potential (Sections 3.3.2 and 3.3.3) are calculated by solving the Poisson equation. In this work, the detector geometry and configuration of the electrodes are input into the programme SIMION [58, 59], to generate the potentials and electric fields. ADL is then used to generate the weighting fields for each segment as well as the charge carrier trajectories for AGATA crystal A006. This process is discussed further in Section 5.3.

5.2.1 Detector Geometry and Electrostatic Field

The first step to create a signal shape database is to specify the detector geometry. The 3 geometries for the AGATA detectors (A, B and C), are specified within SIMION. The geometry of detector A006 is depicted in Fig. 5.1.

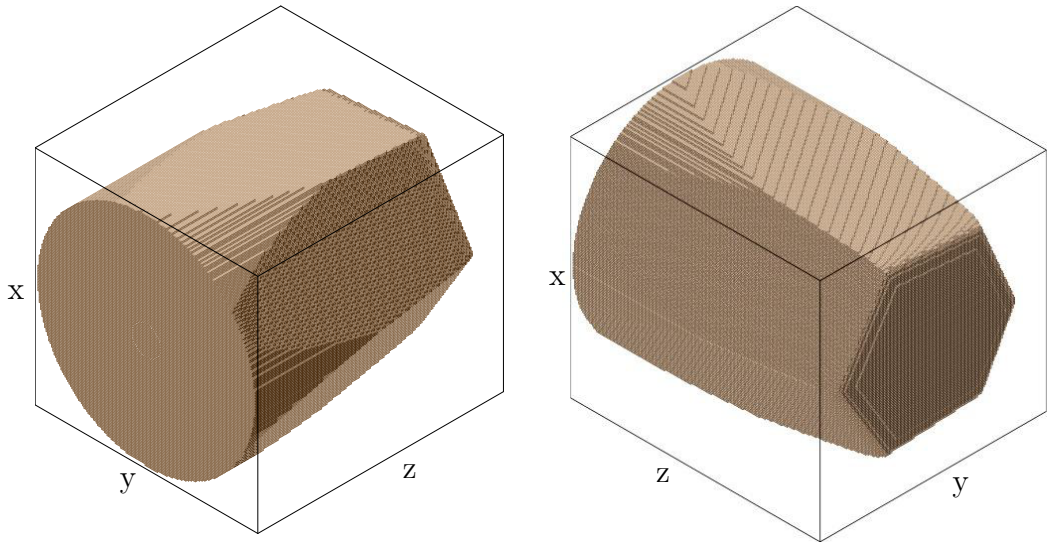

Figure 5.1: Geometry specification for detector A006 as generated by SIMION. The geometry of the core and segment electrodes have been specified in order to generate the electric field and potential utilised by ADL [60].

The electrostatic potential is derived from this detector shape as well as the

applied bias voltage. The Poisson equation, Equation 5.1, can be used for the calculation of the electric potential,

$$\frac{d^2\Phi}{dx^2} + \frac{d^2\Phi}{dy^2} + \frac{d^2\Phi}{dz^2} = \frac{-\rho(x,y,z)}{\epsilon_0} \tag{5.1}$$

where $\rho(x, y, z)$ is the space charge density in the volume. The boundary conditions of the volume and the relative dielectric constant, ϵ_0, must be known for the calculation of Φ(x, y, z).

The space charge density is provided to SIMION. This charge density of the crystal is determined by the impurity concentration from the front to the back of detector A006, 1.80-0.52 x 10^{10} cm^{-3}. The field strength must be determined numerically due to the complex shape of the AGATA crystal.

The electric potential profile on a xz plane through the centre of the crystal is depicted in Fig. 5.2 (left) for an applied bias voltage of + 5000 V at the central anode contact and 0 V at the cathode.

The electric field, E, as a function of position is calculated using the voltage boundary conditions from Equation 5.2:

$$E(x,y,z) = -\nabla\Phi(x,y,z) \tag{5.2}$$

and is depicted in Fig. 5.2 (right). There are three distinct regions of charge collection due to the shape of the electric field: the front face of the detector (A), the front corners (B) and the charge collection in the coaxial region of the detector (C).

The electric potential decreases from the central contact with the radius. Within regions (A) and (B) the gradient of the field is high at the front and in the corners of the crystal. This is most extreme in region (A) where the distance between the electrodes is smallest and are in an approximately planar configuration. The electric field is nonuniform at the front corners within region (B). The electrons produced in this region will travel along the electric field lines diagonally toward the bottom of the central contact. The crystal asymmetry affects the electric field in this region shown by the field asymmetry on either side of the crystal. In region (C) the electric field profile is approximately uniform as charge carriers are collected across the radius of the detector toward the central and segment electrodes. At the back of the detector between 85-90 mm the field strength is low.

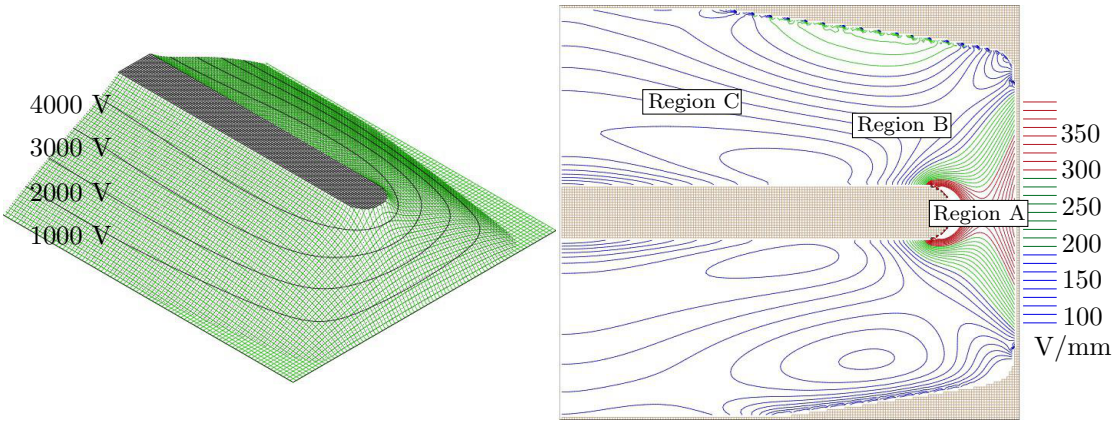

Figure 5.2: An illustration of the electric potential (left) and electric field (right) on the xz plane through the centre of the crystal. The electric field gradient varies in across the crystal in the three regions: A, B and C. The behaviour of the field within these regions is discussed in the text.

5.2.2 Weighting Potential and Field

In order to determine the response of the detector at the electrodes the weighting potential and field must also be calculated. This calculation has been discussed within Section 3.3.3. The boundary conditions specified for this calculation are +1 V on the charge collecting electrode and 0 V at all other electrodes. The weighting potentials as calculated by SIMION for a segment and core electrode are shown in Fig. 5.3.

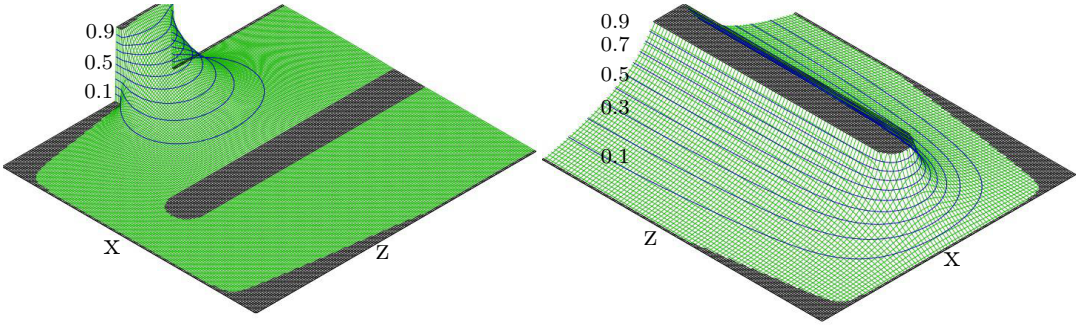

Figure 5.3: The weighting potentials of segment A4 and of the core electrode on the xz plane through the centre of the crystal

The weighting potential for each electrode extends to adjacent electrodes and through the entire crystal. Smaller segment electrodes will have a weighting potential which drops off to near zero beyond the adjacent neighbouring segments. The distribution of the core weighting potential is similar to the

electric potential, both of which drop off radially from the central electrode. The segment weighting potential is shown in detail in Fig. 5.4

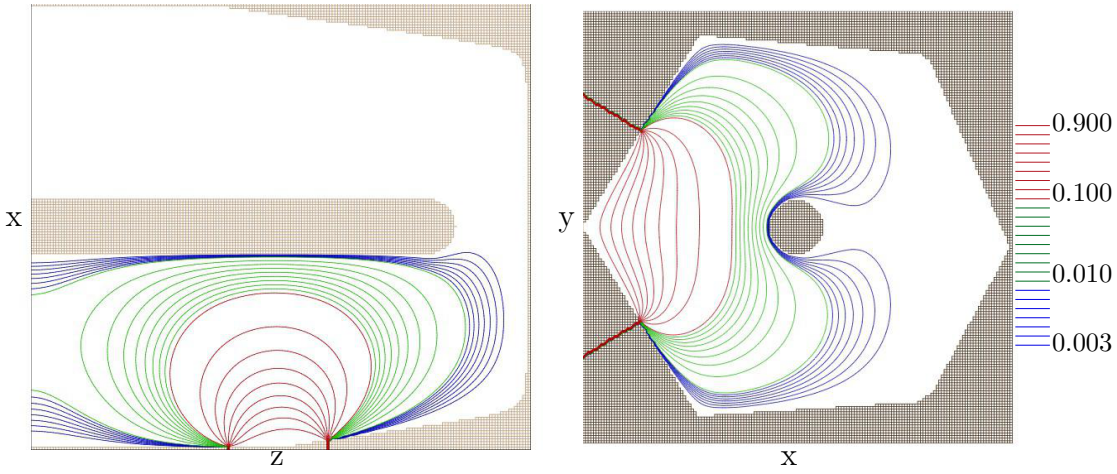

Figure 5.4: The weighting potential for segment A4 on the xz plane through the centre of the crystal (left) and on the xy plane of the crystal (right). The field is strongest towards the segment electrode and drops off quickly.

From the potential derived from the Shockley-Ramo theorem, the induced transient charges are determined by the position of interaction, Equation 3.13. For interactions close to the central electrode, electrons will be collected more quickly. Holes will be collected slowly for the same interaction. Conversely at interactions far from the central cathode, the holes will be collected more quickly and electrons more slowly. The magnitude of the transient signals induced is determined by the weighting potential field from the charge collecting electrode on its neighbouring segments. The shape and magnitude of the transient response is governed by the shape of the weighting field.

5.3 Features of ADL

The electric fields, electric potentials and weighting potentials are calculated within the SIMION programme utilising the detector geometry as well as the applied bias voltage to set the boundary conditions. This calculation is performed with SIMION due to its flexibility. Once these have been calculated, they are read into ADL in order to calculate the drift velocity and determine the signal shapes produced by the detector. The libraries included within ADL are designed to be flexible enough to use with multiple detector geometries for other HPGe applications.

The process of signal shape calculations in ADL is given in Fig. 5.5.

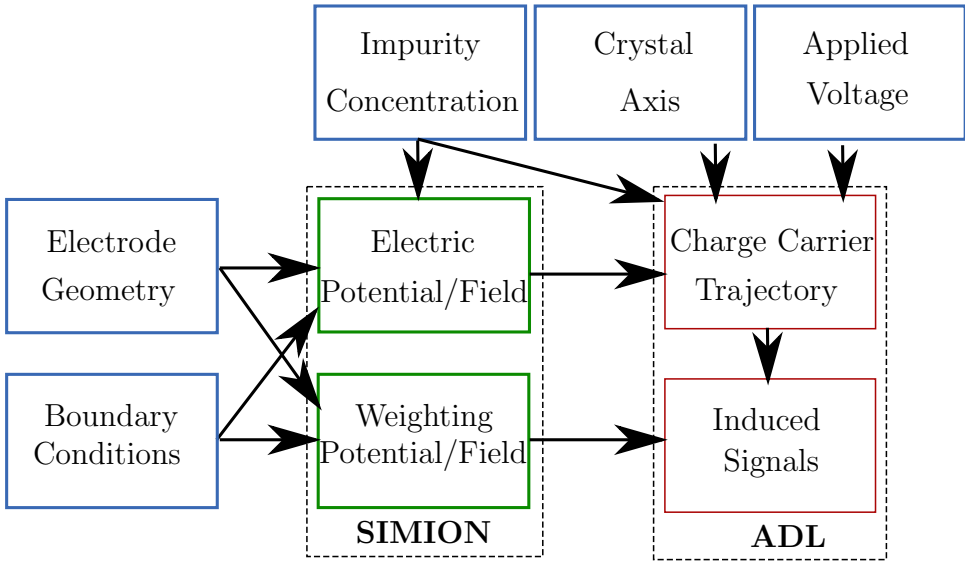

Figure 5.5: A flow chart indicating the steps used to calculate the pulse shape database using ADL.

ADL utilises the crystallographic axis configuration and the impurity concentration as reported from the crystal manufacturer. This impurity concentration is reported with a linear gradient which is used for the calculation but not necessarily accurate, as discussed in Section 4.1.2. Electron and hole mobility values are then used to calculate the charge carrier drift velocity, using Equation 3.10. The charge collection process is then calculated within ADL, either on a fixed grid or from a list of x, y and z positions. The results derived include the signal shapes generated by the core electrode, charge collecting electrode and transient signals induced on neighbours on a fixed 1 or 2 mm grid. The output from ADL can be given in ASCII format for quick analysis and for use within the pulse shape analysis algorithms

The database used to compare the simulated pulse shapes to the experimental database was generated on a 2 mm grid, which yielded 46 318 positions. The points generated for the A006 detector on this grid are depicted in Fig. 5.9.

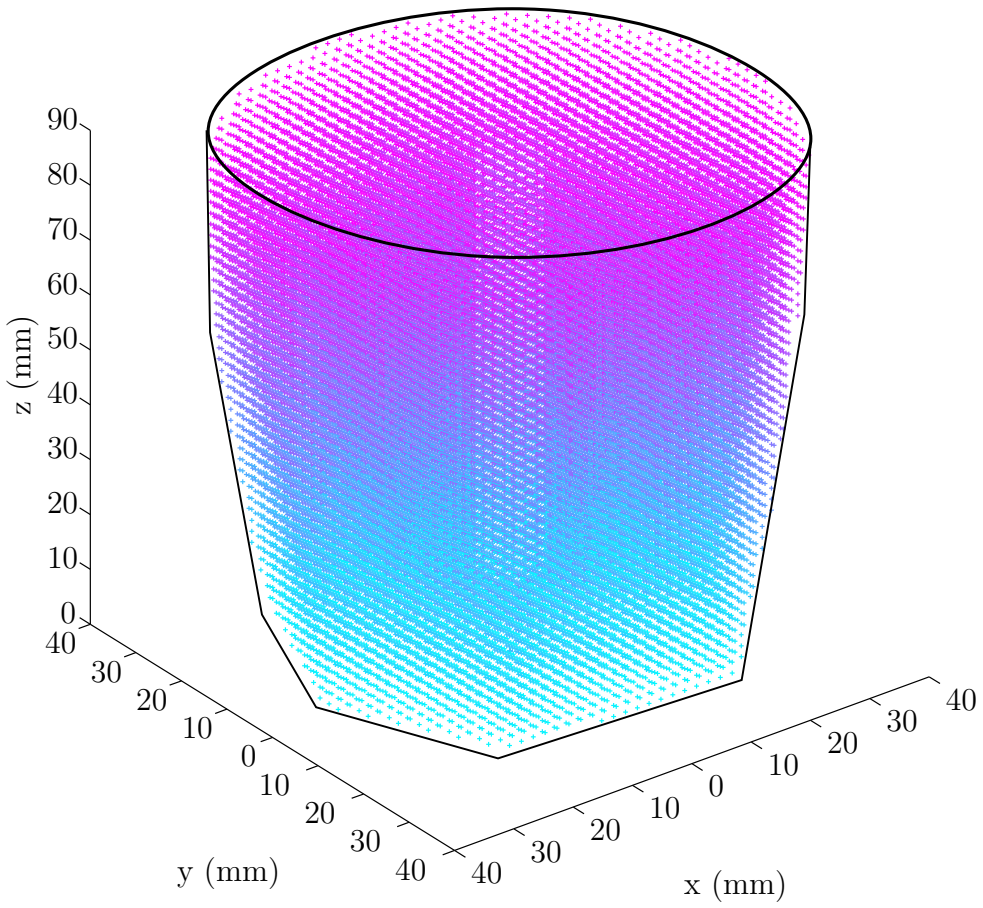

Figure 5.6: The 2 mm grid of positions generated in an ADL simulated database used to compare with the experimental A006 data. There are 46 318 positions within this database. The colours are chosen to highlight the detailed grid.

5.3.1 Preamplifier Correction

In order to generate a simulation equivalent to the output from the capsule and test cryostat the signal must be corrected in several ways. To account for the long decay and limited bandwidth of the charge sensitive preamplifier, a correction based on the AGATA charge sensitive preamplifier output is applied.

A correction to the raw ADL signal has been applied including the response of the preamplifier. The AGATA preamplifier has been introduced in Section 3.4.2. The output of the preamplifier, the voltage response $V(t)$, is a convolution between the input current, $I(t)$, and the preamplifier response function, $R(t)$, given in Equation 5.3:

$$V(t) = \int_0^t I(t - t') \cdot R(t')dt' \tag{5.3}$$

The preamplifier response function, which is taken from [61] as a function of time, t, is given in Equation 5.4,

$$R(t) = g \cdot \frac{1}{1-c} \cdot \left(\frac{1}{1 + \frac{(1-c)}{c} \cdot exp(-b \cdot t)} - c \right)^{\frac{-t}{t_d}} \tag{5.4}$$

which is derived from the Sigmoid function [62]. Where g is the gain, the value of b determines the rise of the pulses and $(1-c)/c$ determines the point of the change in the curvature of the signal shape. This response function was applied to the ADL simulated database. The correction of a charge collecting segment B4 and its neighbours, as well as the core are shown in Fig. 5.7.

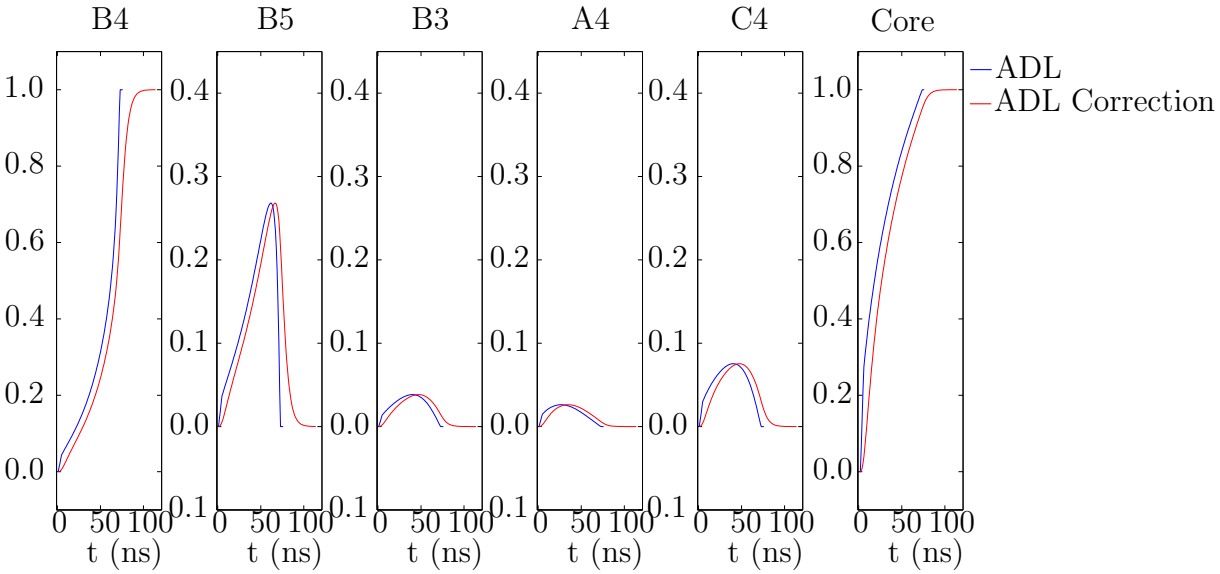

Figure 5.7: The preamplifier response function correction to the ADL simulated pulse shapes. Equation 5.4 has been applied to the charge collecting segment and its neighbours, as well as the core.

The influence of the preamplifier on the signal causes a long decay on the real charge pulse shape signal in segment B4 and in the core signal. The correction smooths out the curvature on the transient signal shapes as well. The correction will affect the risetime calculations performed in Section 5.3.3, lengthening the both the T30 and T90 calculated values. This correction has been applied to the simulated database used for the rest of the analysis in this rest of this chapter and within Chapter 6.

5.3.2 ADL Signal Shapes

The signal shapes generated from ADL can be studied by examining how the pulse shapes change as a function of position over the volume of the detector. To study the simulation results by position, the ADL data base was generated again for detector A006 on a 1 mm grid. The following sections give the results of this study through the calculation of the T30 and T90 rise times as well as the position sensitivity. An example of signal shapes generated for detector A006 for interaction positions at Z = 40 mm on a line within segment C4 are shown in Fig. 5.8.

The evolution of the pulse shapes across the charge collecting segment and core is shown from the core electrode (blue) to the segment electrode (red). From the core and C4 plots, the rise time values for positions close to the charge collecting electrodes are steeper as charge is collected more quickly near the electrode.

The evolution of the transient signals is shown for the neighbouring segments (C3, C5, B4, D4). The magnitude of the transient signals is directly dependant upon the interaction position which increases for interactions close to the neighbouring segment. This effect is clearly shown in the plots of the response of segments B4 and D4. Charge is also induced on the segments directly above and below the charge collecting segments. The Z = 50 depth is closer to the Ring 3 than Ring 4, which results in the transient signal having a greater magnitude in Segment C3 than in Segment C5.

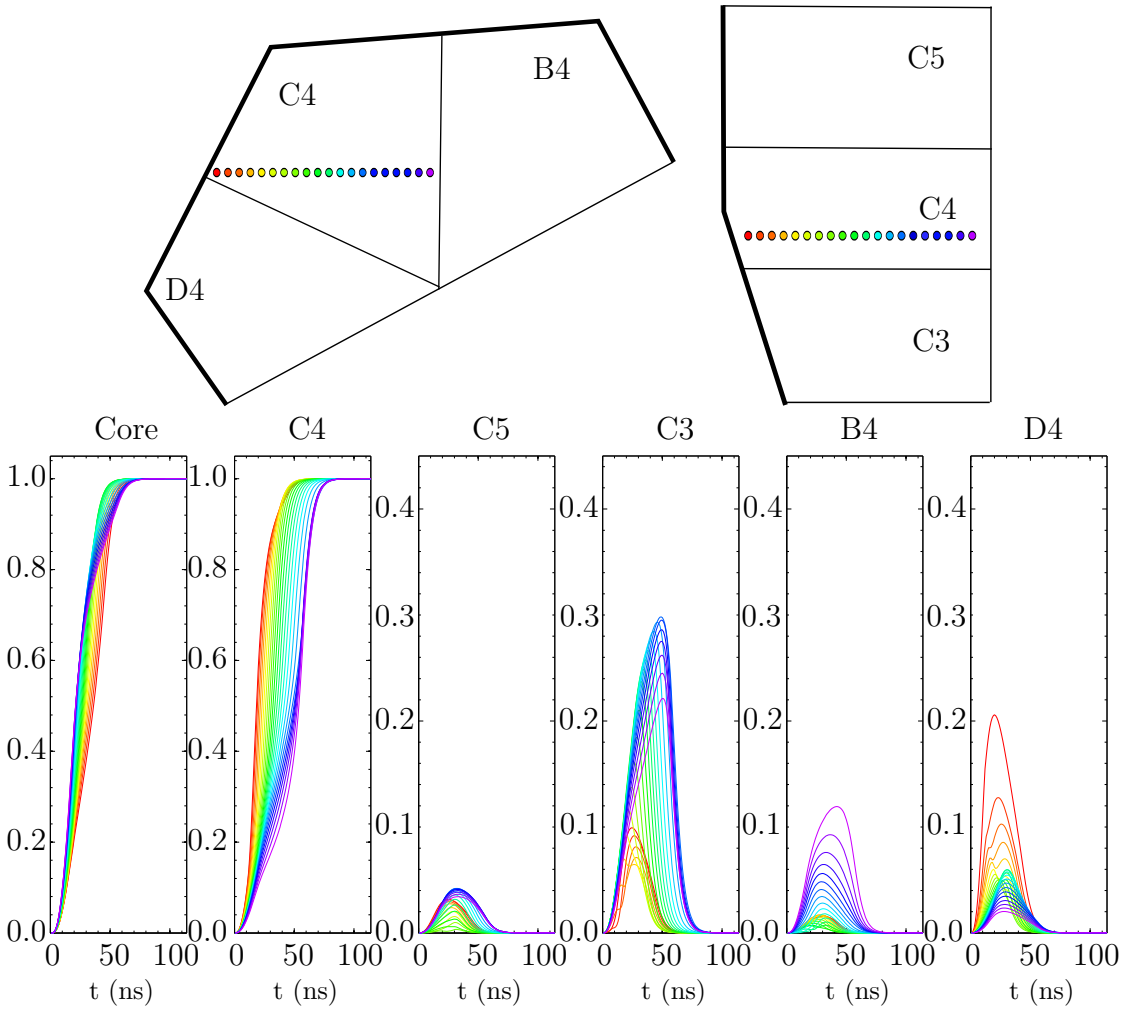

Figure 5.8: The evolution of ADL pulse shapes and transient signals across segment C4 at Z = 40 mm from the detector front face. The evolution of both the core and charge collection segment signals as the interaction position moves from the segment electrode (blue) toward the core electrode (red) are shown. The evolution of the transient signal induced upon the neighbouring segments is shown as the interaction position changes across the charge collection segment.

5.3.3 ADL Rise Time Calculation

The T30 and T90 rise time values have been calculated from the 1 mm ADL database. This calculation is made on the core signal in order to study charge collection as a function of position. To approximate the response from the experimental *Front Face Singles Scan* for rings 1, 2 and 3 the risetime calculation has been calculated from a weighted average over the depths of the rings. The calculation of T30 and T90 are taken from the t10 to t30 and t90 times, respectively. Within Ring 1, depths 1 - 8 mm were averaged; Ring 2, depth 9 - 21

mm were averaged, in Ring 3, depths 22-36 mm were averaged. The rise time maps are shown in Fig 5.9.

For the T30 core risetime values, the fastest risetime occurs at positions close to the core electrode. Within the T90 risetime plots, central regions of the rings have the highest rise times as observed experimentally. The crystallographic axis can also be observed as the azimuthal variance in risetime. The core risetime response of the A006 simulation shows good agreement with the experimental core risetime calculation, see Section 4.5.2.

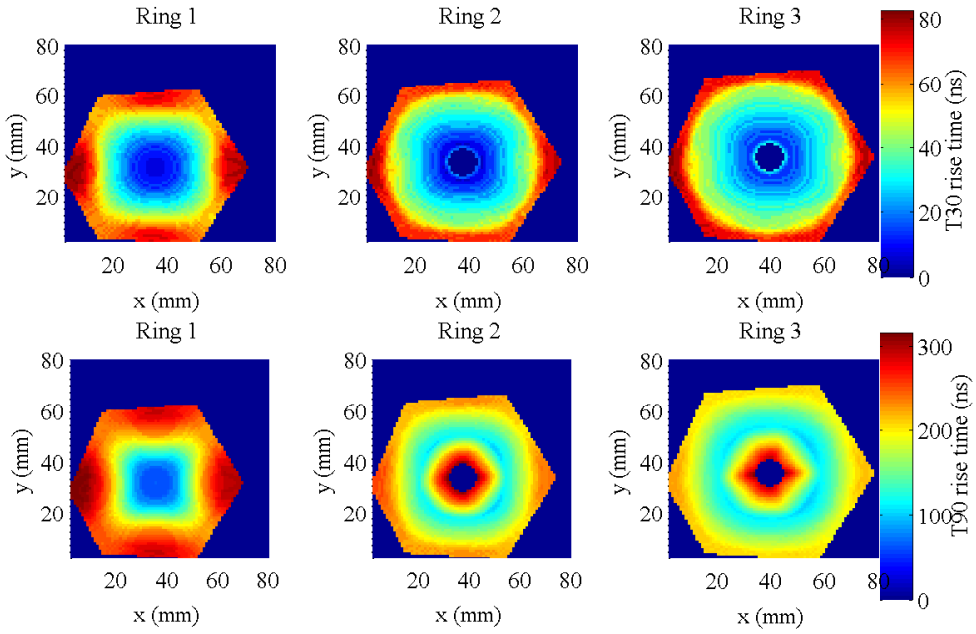

Figure 5.9: ADL T30 core rise time (top) and ADL T90 core rise time (bottom) for rings 1-3. These values are calculated from a 1 mm ADL database by weighting each Z layer over the ring depth and accounting for the photon attenuation through the crystal. The four fold crystallographic axis can be observed as the azimuthal variance in rise time.

5.3.4 ADL Position Sensitivity

The position sensitivity of simulated 1 mm database is calculated. The sensitivity, S_{ij}^2, is defined as the change in signal shape in time produced by each detector segment over the volume of the crystal. This will result in the variance in the response by position within the entire detection volume.

This can be defined as the difference in signal across every segment, $q^k(t)$ - $q^j(t)$, at time t between positions i and j. The detector sensitivity S_{ij}^2 is given

by Equation 5.5,

$$S_{ij}^2 = \frac{\Delta r_{ij}^2}{\Delta s_{ij}^2} \tag{5.5}$$

where Δr_{ij} is the distance between the electrodes and Δs_{ij} quantifies the difference in signal amplitudes. The sensitivity over all of the detector segments over the entire signal is given in Equation 5.6,

$$\Delta s_{ij}^2 = \sum_{k=1}^{k=37} \sum_{t=t10}^{t90} \Big[\frac{q(t)_i^k - q(t)_j^{-k}}{\sqrt{2}} \Big]^2 \tag{5.6}$$

where k is the segment index.

This equation was adapted from [63] and used to calculate the sensitivity for the ADL 1 mm database for the difference in signal in the x, y and z directions as the interaction positions moved. For those positions that are less sensitive, the Δs_{ij} value is lower. Higher Δs_{ij} values indicate regions which produce varying signal shapes.

The sensitivity of the signal shapes is calculated for a xy plane at Z = 45 mm in the centre of the detector. The *xy direction* sensitivity, is shown in Fig. 5.10(a), the *xdirection*, Fig. 5.10(b), and the *Y direction*, Fig. 5.10(c).

The xy sensitivity maps indicate that the greatest detector sensitivity occurs at the segmentation edges. There is also a sensitivity across the xy direction of each segment. This azimuthal dependance is due to the change in transient signal magnitude, dependant upon interaction position.

The sensitivity has been calculated on the xz plane at y = 0 to show the signal variance over the centre and length of the detector. The sensitivity of the signal shapes in the *xz direction*, Fig. 5.11(a), the *xdirection*, Fig. 5.11(b), and the *Z direction*, Fig. 5.11(c).

The xz plane figures indicate that at the segment boundaries the signal shapes vary greatly. In the central regions of the segments, the sensitivity is lower, indicating a lower variance in signal shape of all segments of the detector. The sensitivity for the x direction over the centre of the segments is, however, greater than that of the z direction sensitivity due to the change in signal shape as the charge is collected by the electrodes.

In the front of the detector where the electric field becomes approximately planar there is a high sensitivity. In this region the z direction sensitivity varies greatly as the charge is collected along the electric field lines, electrons towards

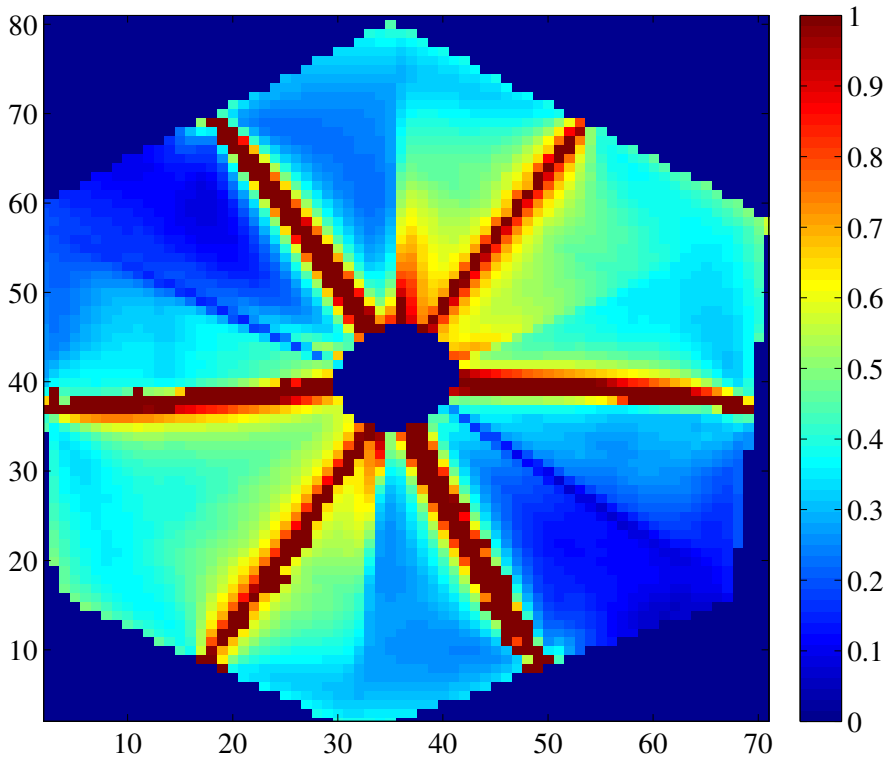

(a) Total xy on a xy plane.

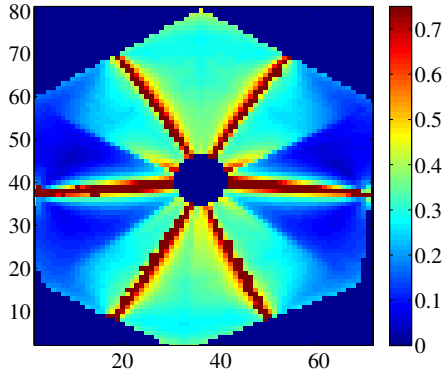

(b) X sensitivity on a xy plane.

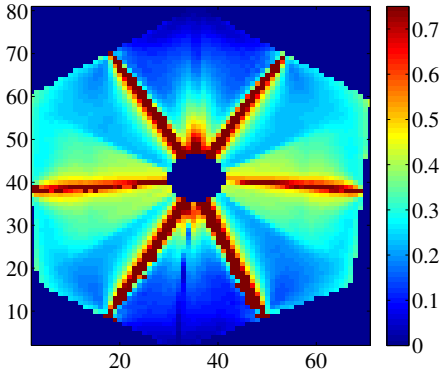

(c) Y sensitivity on a xy plane.

Figure 5.10: The sensitivity, Δs_{ij}, of the xy plane for the 1 mm simulated pulse shape database.

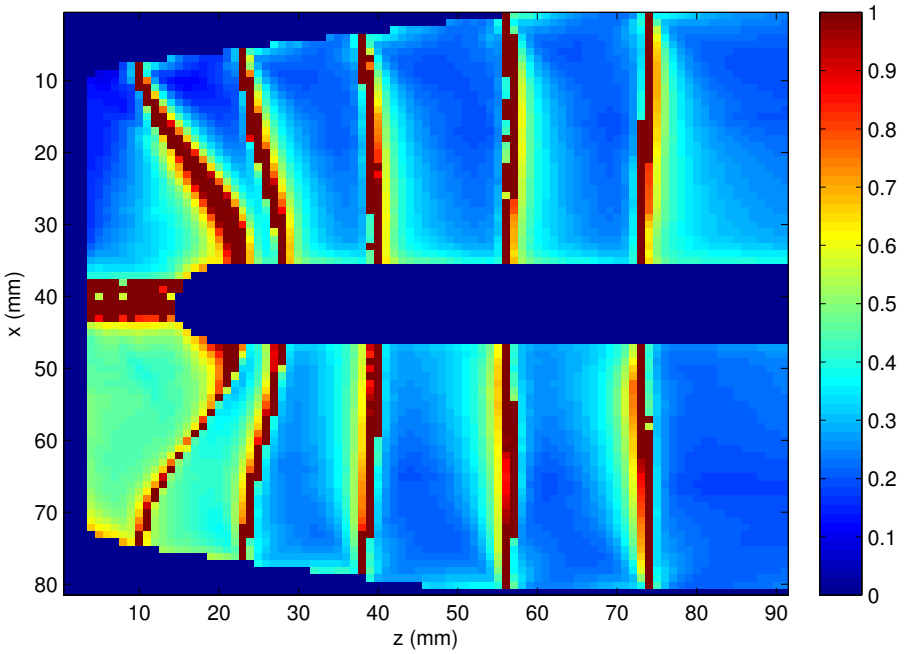

(a) Total xz Δs_{ij} calculated for the y = 0 plane.

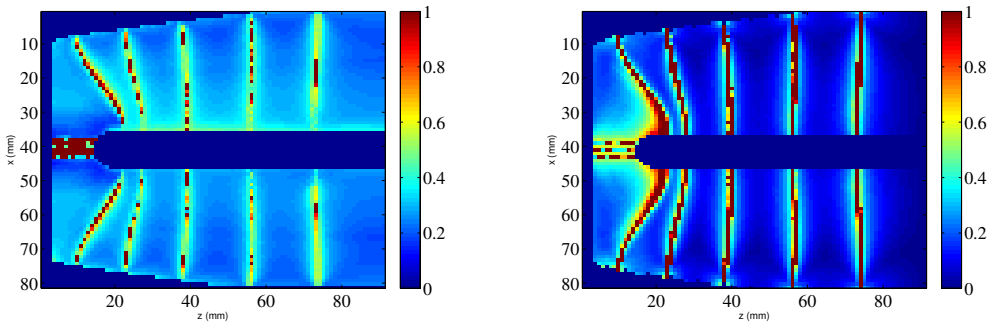

(b) The x Δs_{ij} calculated for the y = 0 plane. (c) The Z Δs_{ij} calculated for the y = 0 plane.

Figure 5.11: The sensitivity, Δs_{ij}, is calculated on a xz plane at y = 0 for the 1 mm simulated pulse shape database.

the central electrode and holes toward the segment electrodes. The result of this measurement indicate that a regular grid of simulated interactions may not be the most effective for online experimental pulse shape analysis. A database with less detail in central segment regions and greater position resolution near segment boundaries and in the front of the detector could be a more useful database for PSA due to the higher sensitivity in these regions.

The xz sensitivity has been examined further by making a cut across the xy plane at x = 14 mm, shown in Fig. 5.12. There is a sharp increase in sensitivity at the segmentation boundaries through the depth of the detector.

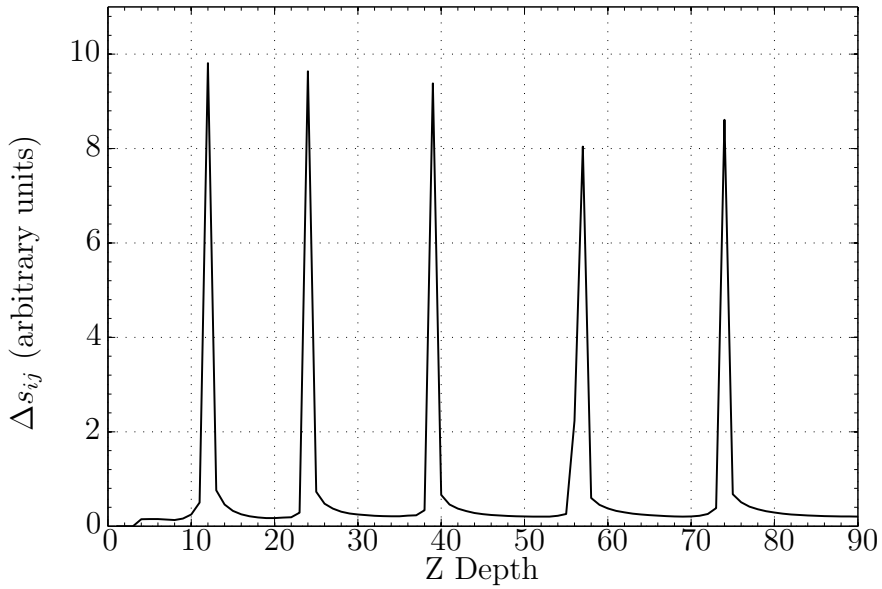

Figure 5.12: The Δs_{ij} as a function of Z depth for the xz plane at x = 14 mm.

5.4 Summary

The ADL library has been introduced and the signal shapes generated have been studied. Rise time and position sensitivity have been calculated for a 1 mm database. Referring to the experimental core rise time calculations in Appendix A, the behaviour of the ADL database is very similar to the experimental data. This calculation indicates that the simulation signals have similar values as the experimental results when looking at the average position performance of the detector. The sensitivity demonstrates how the signal shapes vary for detector A006 over its volume, indicating the utility of a non-uniform pulse

shape database for PSA calculations. A detailed comparison of the corrected simulated ADL database will be done with real experimental data acquired for detector A006 within the following chapter.

Chapter 6

Experimental Pulse Shape Database

An experimental detector pulse shape database is generated to validate the simulated pulse shape databases. In order to create the experimental pulse shapes, the detector signal response is produced from precisely defined single site γ-ray interactions within the HPGe material through a *coincidence scan*. This coincidence scan is performed using the AGATA capsule A006 coupled with ancillary scintillation detectors.

The purpose of the coincident data acquisition is to calculate a pulse shapes produced at precise XYZ positions within the detector. This measurement is performed with the Liverpool scanning table using secondary lead collimators to laterally isolate each detector ring. The collimated ^{137}Cs photon beam, moved in XY by the Parker scanning table, impinges on the detector and through the Compton scattering interaction process, some of the 662 keV photons will scatter at 90° within the AGATA detector which can then be detected within scintillator detectors surrounding the secondary collimators. This allows for identification of the position of interaction in the Z direction. The pulse shapes are used to calculate averages, or mean pulses, for each position in each ring. The average is calculated to reduce the electronic signal noise on the individual pulses.

Ideally, a scan of all of the AGATA asymmetric detectors would be performed to test the simulated databases. However, given restrictions on the availability of each crystal for this process and the length of time of coincident data acquisition, the priority was made to scan at least one of each shape of AGATA detector. In this way, the electric field simulations can be validated and verified.

6.1 Coincident Scanning Method

The process of performing a coincidence scan on the AGATA detectors has been outlined in both [42, 49]. Some of the principles important for the data acquisition for A006 will be outlined in this section. Capsule A006 was mounted in the test cryostat above the scanning table in the same configuration as described in Section 4.3.1. A *singles* scan was made in order to identify XY coordinates of the detector front face provided by the scanning table.

The detector was then surrounded with semicircular lead bricks which acted as the secondary collimators. Gaps between the bricks were made at each ring depth in order to isolate position interactions on a Z depth within each ring. Scintillator detectors were then placed at these gaps. Over a period of 3 months data was collected for capsule A006 in coincidence with the ancillary scintillator detectors in order to collect a sufficient amount of statistics for all positions.

6.1.1 Collimator and Scintillator Layout

The layout of the secondary collimators is distinguished by the left side (LS) and right side (RS), shown in Fig. 6.1. The scintillator detectors used included 36 small hexagonal bismuth germinate (BGO) detectors and 3 sodium iodide (NaI) detectors. The BGO detectors were clustered together in groups of 3-4, sharing one signal output channel. The clusters of BGO detectors are placed around each collimator gaps on the rings 1-4 on the LS and 1-6 on the RS. The NaI detectors are placed to cover rings 3-4 on the LS of the AGATA detector. The distribution and layout of the collimator ring gaps and detectors is given in Table 6.1.

Ring	Gap Width (mm)	LS Depth (mm)	Scintillators [Cluster]	RS Depth (mm)	Scintillators [Cluster]
1	1.5	4.0-5.5	4 [C1]	4.0-5.5	4 [C2]
1 & 2	3	15.7-18.7	5 [C3/7]	15.8-18.8	5 [C4/9]
3	3	31.8-34.8	2 [C10] + 3 NaI	32.9-35.9	4 [C5]
4	3	50.6-53.6	2 [C12] + 3 NaI	52.0-55.0	4 [C6]
5	3			69.1-72.1	3 [C8/6]
6	3			87.8-90.8	3 [C11]

Table 6.1: The dimensions of the collimation gaps in the the secondary lead collimator configuration used in the coincidence scan.

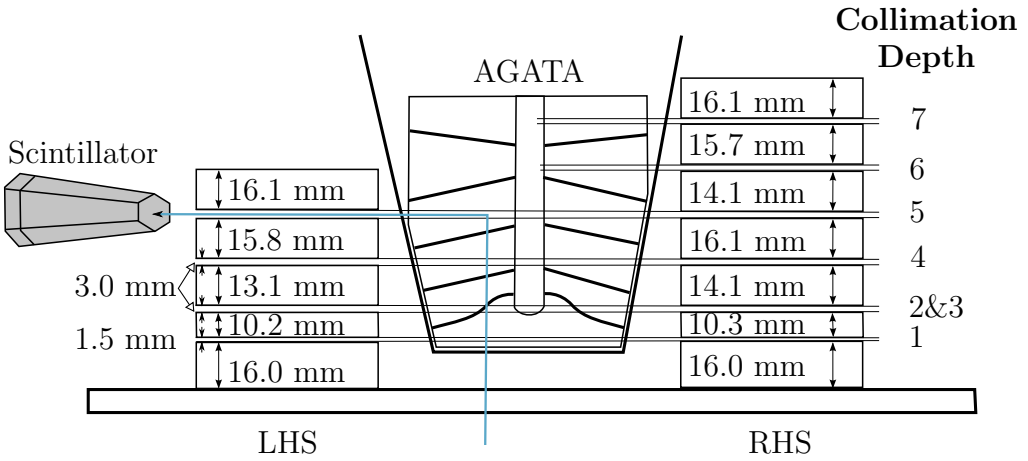

(a) The collimator spacing versus ring depth.

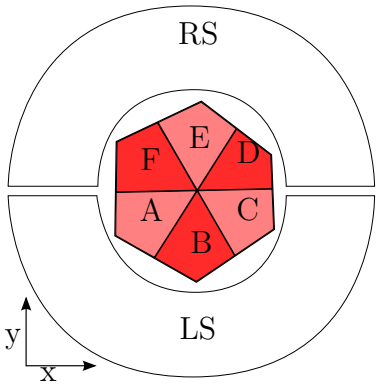

(b) Collimator - detector orientation.

Figure 6.1: Figure (a) shows the coincident scan collimator layout. The secondary lead collimators used in the acquisition of coincidence data. These collimators isolate the Z depth of interaction within each ring. This method allows for the coincident measurement of 90 ° scatter events. Figure (b) shows the detector sector positions scheme orientated on the scanning table.

6.1.2 Scan Positions

The grid of scan positions used for the collection of data is shown in Fig. 6.2. The coincidence scan was made up of 21 radial line scans (a) and 3 azimuthal scans (b), resulting in a total of 366 XY positions. The scan positions were generated by a MATLAB code, calculated based on the detector geometry.

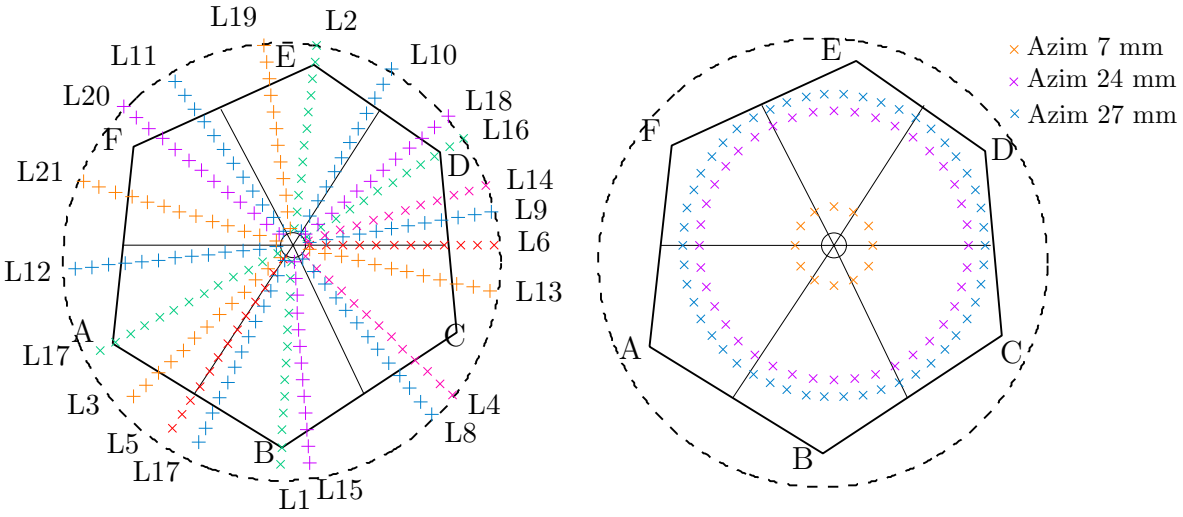

(a) Radial line scan positions.

(b) Azimuthal line scan positions

Figure 6.2: A schematic depiction of the 24 scans taken for AGATA detector A006. 21 radial line scans and 3 azimuthal line scans were performed resulting in a total of 366 XY positions. The sector labels are in the Cologne labelling scheme, which is used in the Liverpool scanning system. The secondary collimation of the detector into 7 depths results in 2562 total scanned positions.

The sector labels in Fig. 6.2 are in the Cologne labelling scheme which used in the Liverpool scanning system. The translation between the Cologne and AGATA labels is given in Fig. 4.3. The radial lines were generated based on the sensitive regions of the detector, which are concentrated near the segmentation boundaries where the signals are changing rapidly. The sensitive regions of the detector segments are shown for the ADL simulation in Section 5.3.4.

The radial line scans were centred on the crossing point of the segmentation of the detector. Each radial line scan has 12 or 13 points, dependant upon the radius of the detector along the line trajectory, which varies due to the detector asymmetry. The azimuthal line scans were generated centred upon the segmentation crossing point, and are therefore offset from the centre of the back detector ring. The detector is scanned at 3 hours per XY position in order to generate enough statistics.

Due to the shape of the electric field, Ring 1 interactions may be detected in the Ring 2 collimation gap. The secondary collimation of the detector into 7 depths, including the Ring 1 and 2 responses at collimator depths 2 and 3, results in 2562 scanned positions.

6.1.3 Data Acquisition Electronics

The coincident data acquisition is performed using scintillator detectors incorporated with the basic electronics used for the singles scans. To create the pulse shape database, additional electronics were used to form a coincident trigger to read out events triggering both the AGATA detector and the scintillator detector response. The singles scan electronics included the ORTEC 659 bias supply to provide capsule A006 capsule with + 5000 V, the CWC modules and the 4 ten channel GRETINA digitisers. The output core analogue signal is input to a ORTEC 671 spectroscopy amplifier with a 6 μs shaping time which was input into the CAEN ADC. The coincident scan electronics setup is shown in Fig. 6.3.

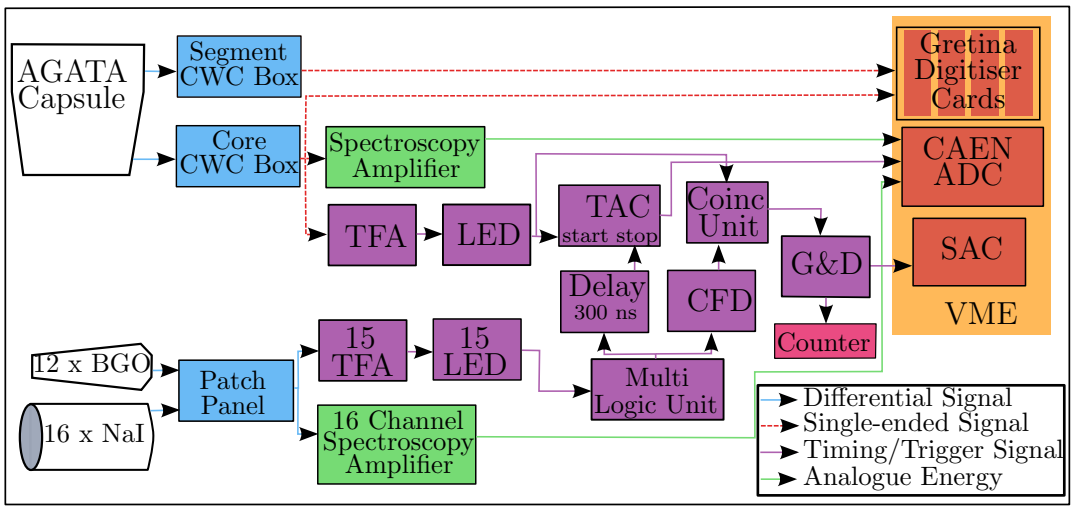

Figure 6.3: A schematic diagram of the electronics utilised for the coincidence scan setup. The trigger used in this mode of data collection was a coincident event between the AGATA capsule and the ancillary BGO and NaI scintillator detectors.

The *coincidence* trigger was generated by coincident events in the AGATA detector and the scintillators. A Timing-to-Amplitude Converter (TAC) produces a signal proportional to the time difference between the START and STOP triggers. The core analogue signal is input into a TFA and CFD, which

is used as the START signal and also input into a Coincidence Unit. The STOP signal is derived from the scintillator detectors. The 3 NaI detectors were powered with Canberra 3106D bias voltage supplies. Two NaI detectors were biased with + 600, the last one with + 750 V. The BGO detectors were coupled together in groups of 3 and 4, to be biased with + 900 V by purpose built voltage supply and preamplifier. The preamplifier boxes summed the BGO signals and supplied one output signal.

The combined BGO and NaI signals were connected to a patch panel to supply two outputs for each signal. One set of scintillator signals was input into a Silena ADC in order to record the analogue energy for gain matching and gating. A summary of the Silena channel map is given in Table 6.2.

LHS Ring	Silena Ch.	RHS Rings	Silena Ch.
1	1	1	2
2	3, 7	2	4,9
3	10, 13 - 15	3	5
4	12 - 15	4	6
5		5	8, 6
6		6	11

Table 6.2: The scintillator - Silena channel layout. The output of groups of 3 - 4 BGO detectors were combined within their preamplifier/bias supply boxes.

The second set of scintillator signals were combined in a Multiplicity Unit, which provides an output when a scintillator is triggered. A 300 ns delay was added to the multiplicity output signal which was used as the TAC stop. The TAC gate was set to 200 ns. A second output from the multiplicity unit was input into the Coincidence Unit. This unit provides the option of a trigger if there is a trigger from either the AGATA detector or the scintillator (a single trigger) or a coincident trigger if the AGATA and scintillator are triggered in coincidence. The coincidence unit output was used in a Gate and Delay generator and then input into the SAC, triggering the data readout.

Calibration data was acquired for detector A006 with ^{241}Am and ^{152}Eu sources. The BGO and NaI detectors were gain matched with ^{57}Co and ^{137}Cs. With the LE threshold set to zero, the background trigger rate for the BGO detectors was ∼50-200 Hz. The background trigger rate for the NaI detectors was ∼0-40 Hz. As the collimators were built around detector A006, a ^{22}Na source, which emits two back to back 511 keV γ-rays, was used to check for coincident

measurements signals between the AGATA detector and the scintillators. The singles trigger rate at the collimator gaps for the BGO detectors was ∼4 kHz in the Ring 1 and on average ∼20 kHz in Rings 2-6. The singles trigger rate for the NaI detectors was ∼1-2 kHz.

The coincident trigger rate varied based on the scanning table position with respect to the detector. In central regions of the detector, there were fewer coincidences (≤0.5 Hz), whereas at the outer regions of the detector the coincidence rate was ≈ 0.8 Hz.

The data readout was determined by a trigger in both AGATA and the scintillators by a coincident γ-ray interaction. The energy deposited within AGATA for a 90° scatter is determined by the Compton scattering formula, Equation 2.5. The energy deposited by the 662 keV γ-ray photon beam scattering at 90° is 374 keV. The remaining photon energy of 288 keV will be detected by the scintillator detectors.

6.2 Pulse Shape Database Generation

Upon the completion of the coincidence data acquisition, the pulse shape library is built from averaging the response of the detector made at each position. The data was filtered offline and average (mean) pulses were formed from iterations at each position in the coincidence scan.

6.2.1 Coincident Event Gates

Pre-filtering of the data is performed with the MTSort programme in order to perform gain matching. Approximately 1% of the events that triggered the system and were recorded for the scan were single site interactions, as only a small portion of interactions between the 662 keV photon beam and the crystal will result in 90° scattered events. The coincident data is gated on fold, detected energy and scintillator channel in order to identify true events at each ring.

Energy Gate: Energy gates are placed on the AGATA core MWD energy and the Silena scintillator energy. The E_{AGATA} vs $E_{Scintillator}$ matrix and the corresponding energy spectra are indicated in Fig. 6.4. The energy gates were placed on the AGATA core MWD energy spectrum and the scintillator energy spectra, corresponding to E_{AGATA} = 288 ± 3 keV and $E_{Scintillator}$ 344 ± 100 keV. The poor energy resolution of the Scintillator signal as well as the detector gain shift contributes the the poor energy resolution. This is observed in the

correlation matrix and the scintillator energy spectra Fig. 6.4 (bottom right). Additional features are visible in the energy correlation matrix, including the faint 511 keV annihilation peak and the full energy 662 keV γ-ray energy.

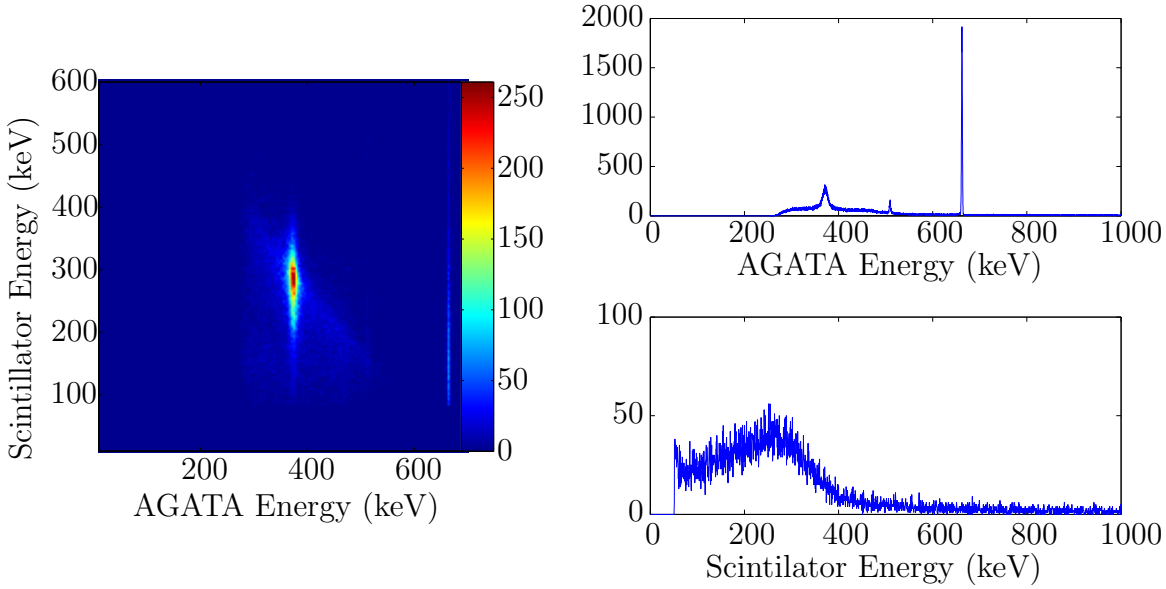

Figure 6.4: Left: The E_{AGATA} vs $E_{Scintillator}$ correlation matrix. Gates were placed on the AGATA MWD energy spectra at $E_{AGATA} = 288 \pm 3$ keV and on the scintillator energy spectra at $E_{Scintillator}$ 344 $\pm$ 100 keV. Right: The corresponding energy spectrum for the core MWD energy (top right) and scintillator (bottom right).

Segment Fold Gate: The data is also gated on the AGATA segment Fold-1 events, where the full 374 keV energy was deposited within one segment. The contributing events which had energy shared between AGATA segments due to scattering were rejected.

Scintillator Fold Gate: There is also a gate placed on Fold-1 scintillator events, in which the scattered 288 keV energy spectra was deposited in a single scintillator.

Ring/Scintillator Correlation Gate: The collimator detector placement resulted in a correlation between AGATA ring and scintillator channel number, summarised in Table 6.2. Events triggered by random combinations of channels that did not correlate to this scheme were filtered from the data.

The number of events which remained after these gates on the experimental data at each collimation depth in rings 1-6 ring is depicted in Fig. 6.5.

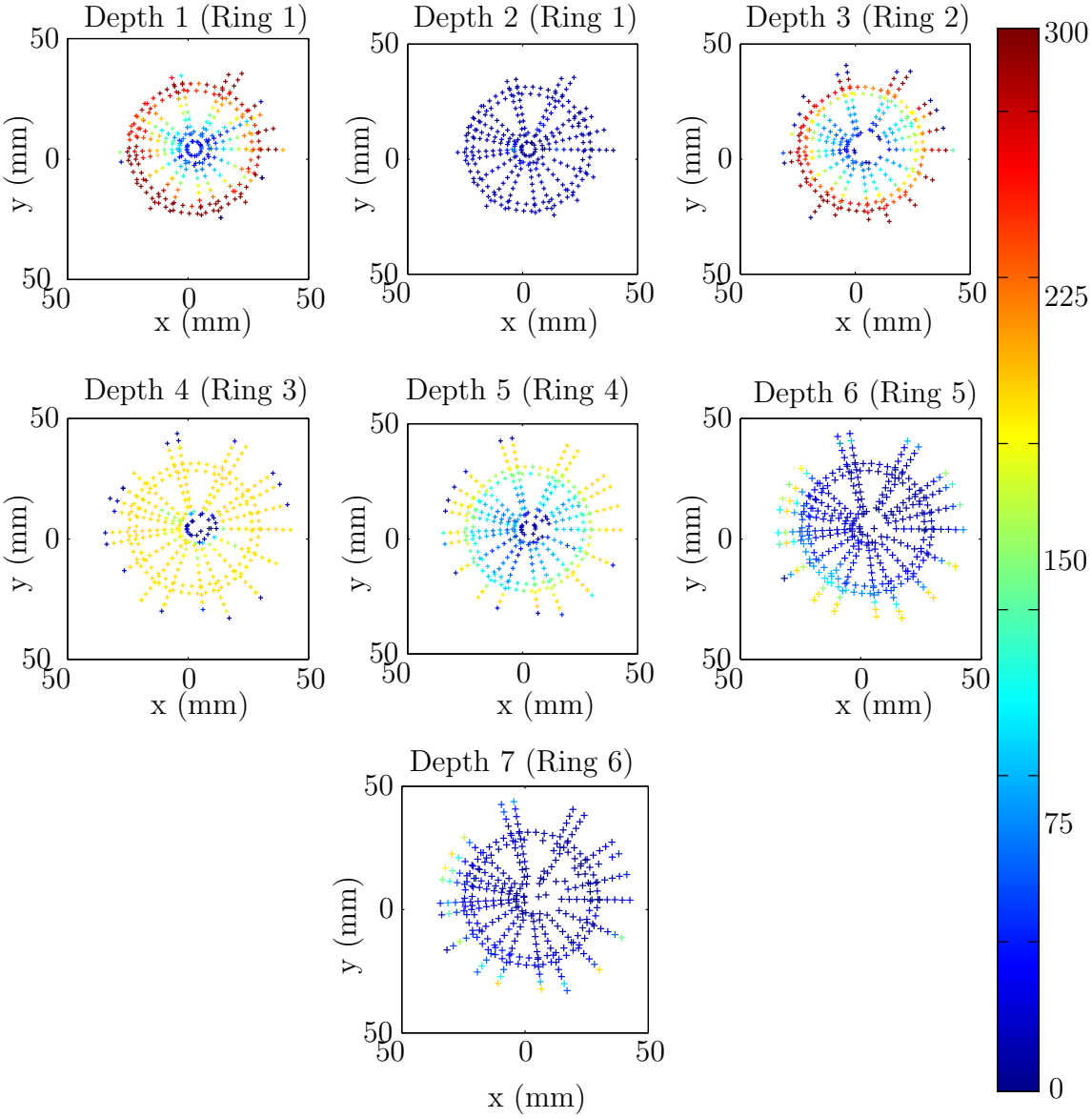

Figure 6.5: The number of coincident events per collimation depth which pass the energy, fold and ring/scintillator gates.

6.2.2 Mean Pulse Formation

The coincidence data acquisition time of 3 hours per position was required to obtain enough statistics in order to form a mean pulse signal for specific x, y and z positions within the detector. The mean pulse code, fm.m, was developed previously by Matthew Dimmock and Carl Unsworth for building the experimental pulse shape database for detectors S002 and C001 as described in [42,49]. This code was used to form the experimental pulse shapes for detector A006.

Mean pulse formation is necessary to reduce baseline noise on the individual signals. The first step of the mean pulse calculation was to normalise the core and segment real charge pulse shapes as well as transient charges to 1. The individual pulses are then time aligned: the segment real charge and transient signals to the T10 and the core signals to T90. The risetime of each channel differs between the segment and core signals. These values were aligned due to the variation in the risetime at sample position which is caused by *walk* in the LE trigger. The number of initial pulse shapes used to calculate the mean varied with detector position, due to a reduction in the number of triggers as discussed in Section 6.1.3.

Photon attenuation of the 662 keV γ-ray leads to a reduction in hits passing the coincidence gates from the front to the back of the detector. In the central regions of the detector, there is a reduction in coincidences due to the likelihood that the photon will scatter again before it is detected by the scintillators. There is also a variation in how well the scintillator detectors cover the rings to detector events, so there will be a variation in the response azimuthally. A minimum threshold of 2 pulse shapes was set in order to form a mean pulse. The number of events contributing to the final mean in each ring is shown in Fig. 6.6

An initial mean pulse was created by averaging all of the pulse shapes from interactions passing the coincidence gates. Each individual pulse shape was then again compared to this mean and any pulse shapes deviating greatly from the mean were then rejected from a final mean calculation. An example of the pulse shapes for an interaction occurring in Segment C4 is shown in Fig. 6.7.

The core and segment real charge pulse shapes as well as the 4 neighbouring transient pulse shapes are shown. All of the pulse shapes passing the coincidence gates are shown as well as the final mean pulses, indicated in red.

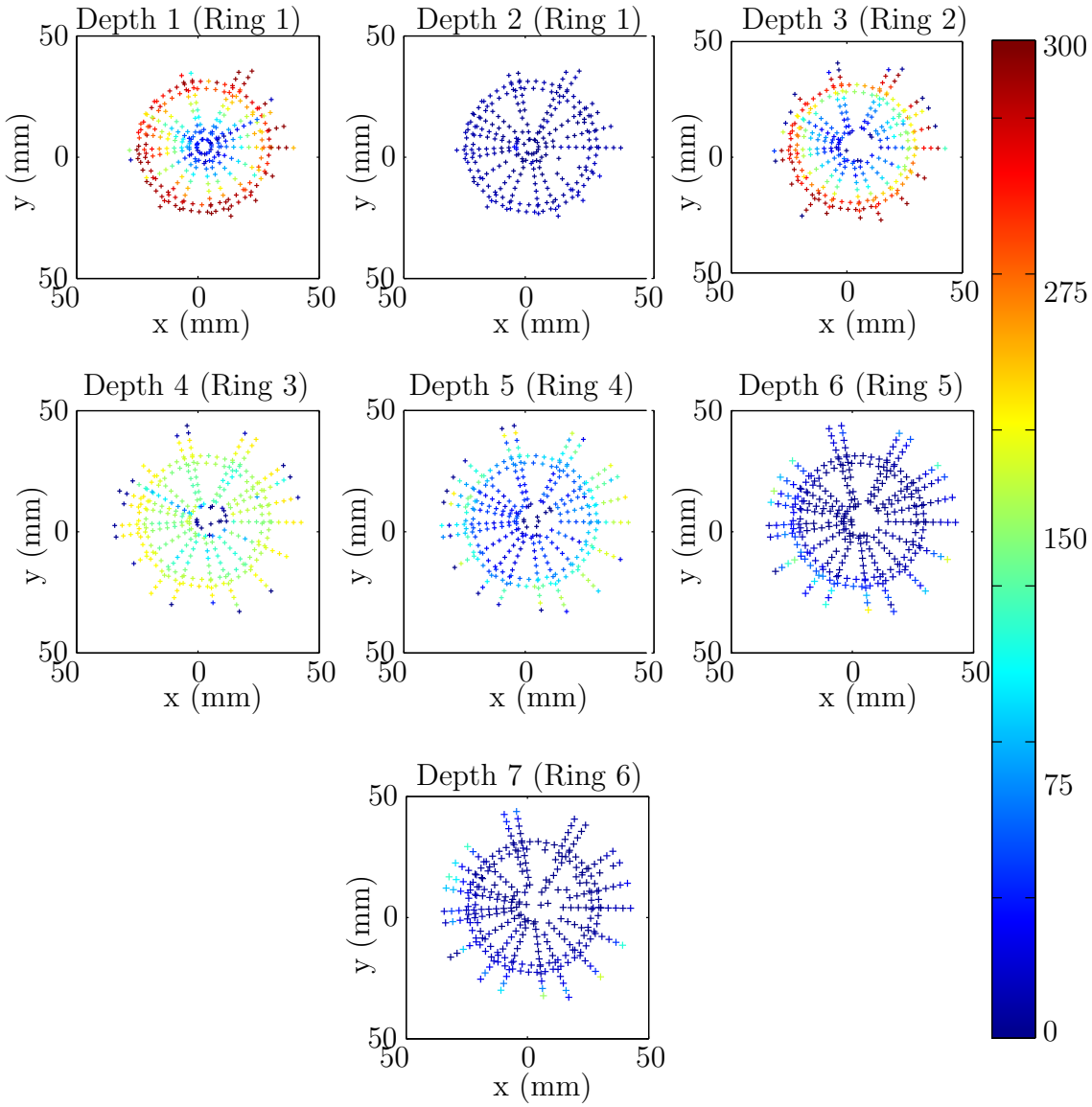

Figure 6.6: The number of coincident events per collimation depth which contributes to the mean pulses.

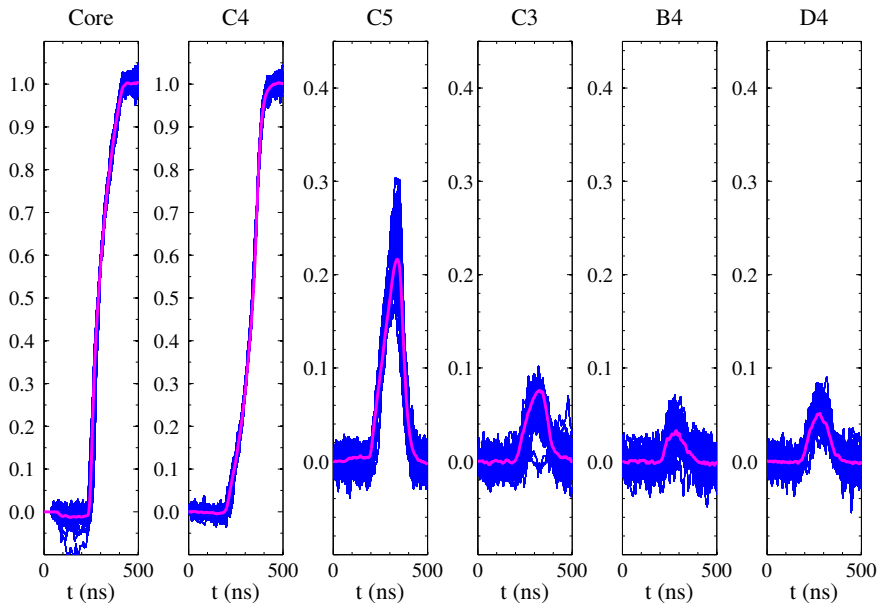

Figure 6.7: An example of the formation of the mean pulse shapes for an interaction in Segment C4. The mean is formed from 52 coincident events. The mean pulse is indicated in red, showing a reduction in baseline noise.

6.3 Experimental Position Translation

Several translations are made in order to convert the detector scan coordinates into the AGATA coordinate system in order to compare the database with the ADL simulated database.

6.3.1 XY Coordinate Rotation

The coordinates of the detector were converted from the scanning table coordinate system to the AGATA coordinates. This was performed in order to standardise the pulse shape database positions as well as to compare the detector with the ADL database. The detector was first translated in XY position to be centred on (0,0) at the front face segmentation crossing point. The detector data set was then rotated 120 degrees to align sector A with the X-axis. The rotation of the coordinate system is shown in Fig. 6.8.

6.3.2 Z Depth Offset

The absolute depth of interaction must be corrected for each of the collimation depths. Uncertainties in this value are caused by the difficulty in the precise

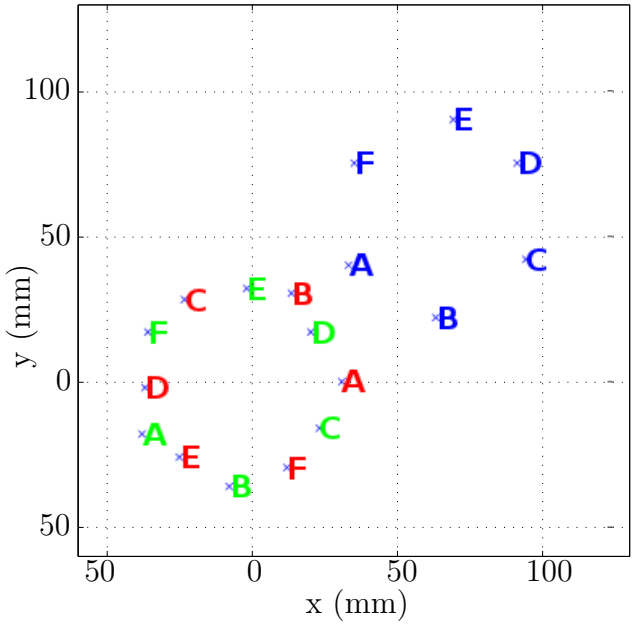

Figure 6.8: The coordinate and rotation correction applied to detector A006. The coordinates were transformed to the AGATA coordinates scheme. The blue labels indicate the experimental scanning table setup. The green labels indicate the translation in XY and the red indicates the final rotation to AGATA coordinates.

positioning of the A006 capsule with respect to the lead collimators and also by the uncertainty distance from the capsule to end cap.

A least squares measurement was made between the ADL simulation and the experimental database in order to verify the Z position of the interaction positions with the rings. The measurement was performed on radial scan line 4, extending from the core to edge of the crystal. Segment C4 due to the uniformity of the electric field within Ring 4.

The original estimation of depth of interaction are given in Table 6.1 indicate that for Ring 4, the Z depth interaction was at 50.6 - 53.6 mm on the right side (RS) of the crystal. The results of the least square measurement are shown in Fig. 6.9.

The calculated least squares measurement indicates that the actual collimation gap for the Ring 4 coincidence measurements differ from the estimated depth. The result of the calculation yielded a minimum value is 54 mm, used as the depth to compare with the simulated database, given in Section 6.5.

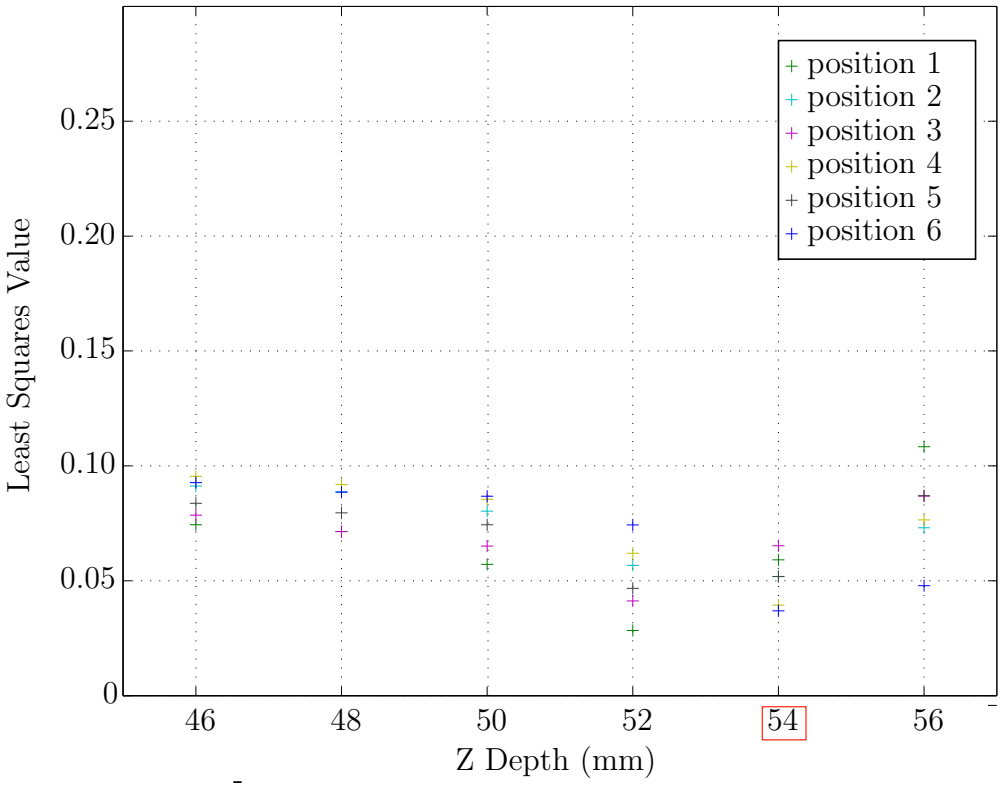

Figure 6.9: The depth correction calculated from a least squares method based on 6 positions within radial line 4. The minimum least squares minimum occurs at 54 mm.

6.4 Experimental Pulse Shape Results

The mean pulse shapes can be examined to look at the pulse shape response of the detector in detail. For this work, Segment C4 in Ring 4 was chosen to illustrate the pulse shape changes radially and azimuthally through the detector. The core, hit segment and hit segment neighbours are used for this analysis. The sensitivity of the pulse response as a function of position has also been measured. The radial lines examined within this section and Section 6.5 are shown in Fig. 6.10.

The experimental mean pulse shapes of radial lines 4, 8 and 13 are given in Figures 6.11, 6.12 and 6.13 respectively. The results for the azimuthal line scans at 24 and 27 mm for sector C are given in Figures 6.14 and 6.15 respectively.

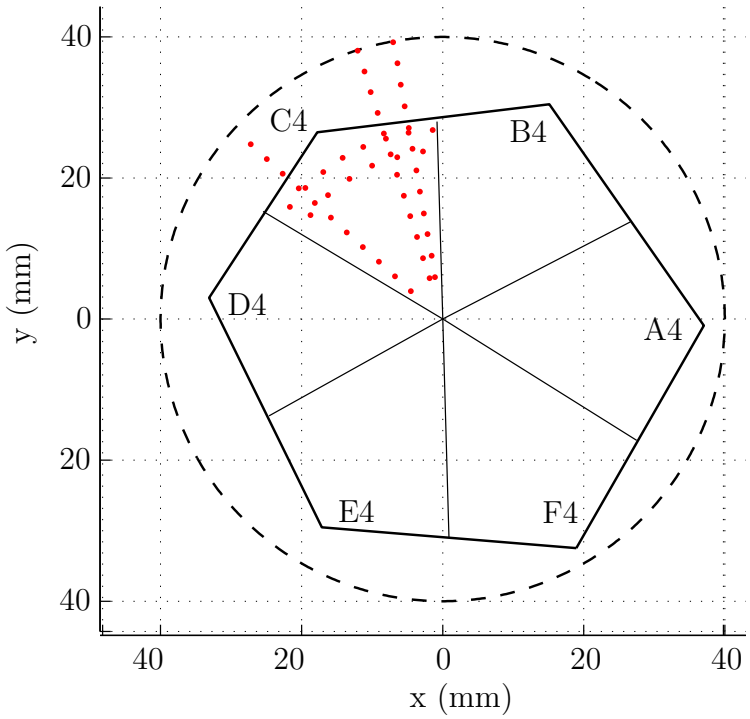

Figure 6.10: The radial and azimuthal lines scanned in Segment C4.

6.4.1 Radial Line Scan 4, 8 and 13

The radial line scans consist of 12 - 13 points equally spaced on a straight line. The radial line scans indicate the change in real charge risetime as a function of radial position. This is due to the change in drift distance for the electrons and holes within each segment. From the radial line scans, it is observed that the core risetime is faster for positions closer to the core electrode.

The C4 segment risetime is slower for positions closer to the core electrode. For positions close to the segment electrode, the core risetime drops and the segment risetime is faster.

The transient charge signal in Segment C5 has a greater magnitude than C3 due to the collimation depth positioning. As the position increases radially the change in transient charge magnitude is also observed, from positive to bipolar to negative. This is the result of the electron and hole collection. Near the core electrode at small radii, the risetime is dominated by the movement of the holes toward the segment contact, which induces positive transient signals in the neighbouring segments. At larger radii toward the segment electrodes the risetime is dominated by the electron collection, which induces negative transient signals. The intermediate radii, bipolar signals are induced.

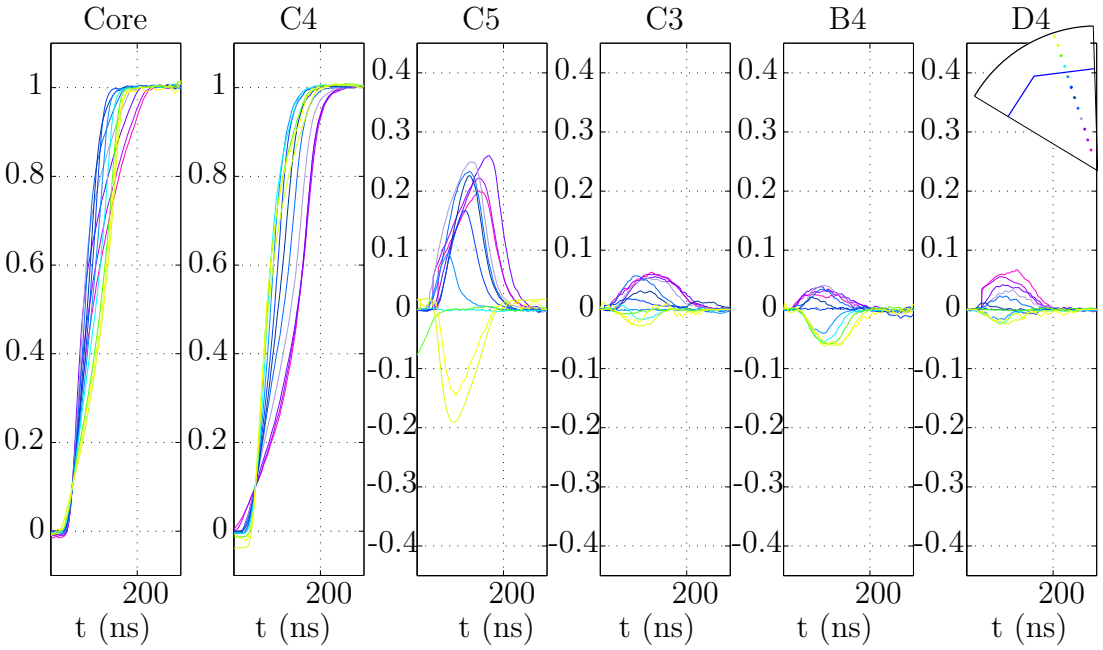

Figure 6.11: Radial Line 4 through Segment C4, where the interaction position moves from the centre of the crystal (pink) to the outer edge (yellow).

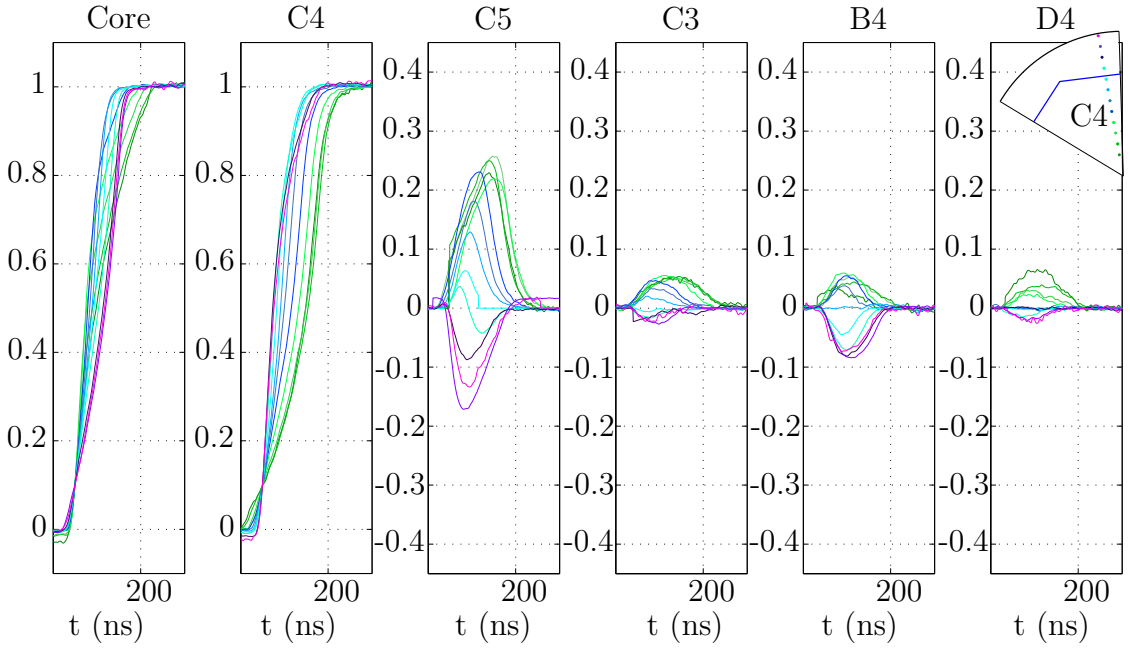

Figure 6.12: Radial line scan 8 through Segment C4. The interaction position moves from the centre of the crystal (green) to the outer edge (purple).

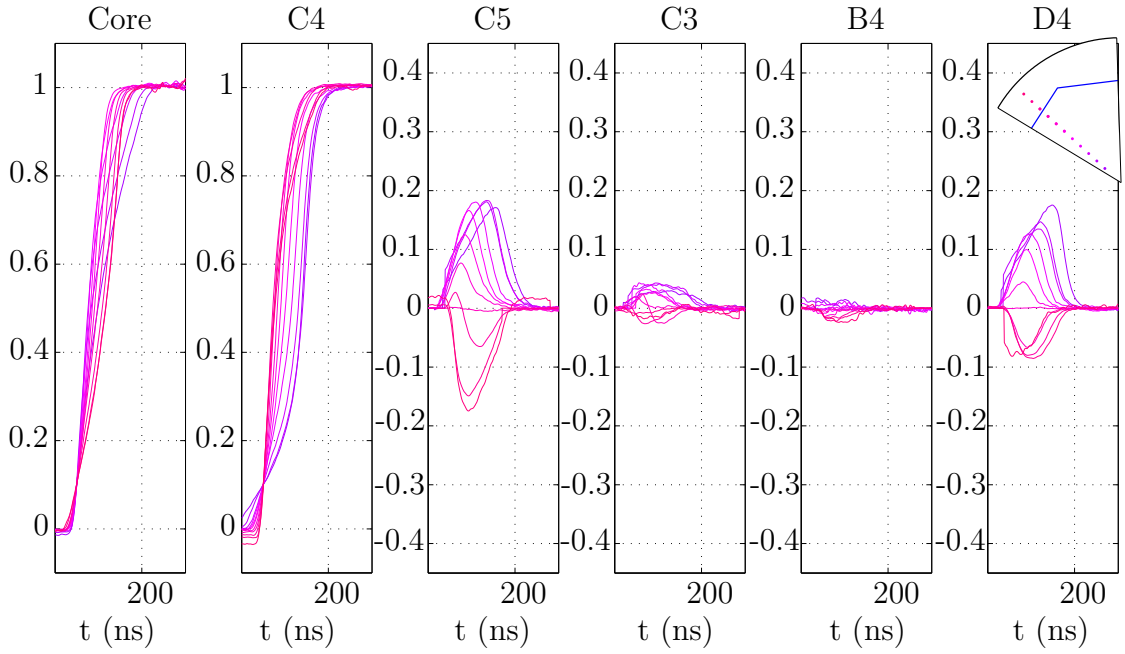

Figure 6.13: Radial line scan 13 through Segment C4. The interaction position moves from the centre of the crystal (purple) to the outer edge (pink).

6.4.2 24 and 27 mm Azimuthal Line Scans

The azimuthal scans through Segment C4 indicate a more uniform risetime at constant radius. The azimuthal scan lines show the change in transient signal magnitude as the position moves from one segment to another. The segments adjacent to C4 within Ring 4, B4 and D4 indicate the position dependance of the transient charge amplitude. This effect is more obvious on the 27 mm scan shown in Fig. 6.15.

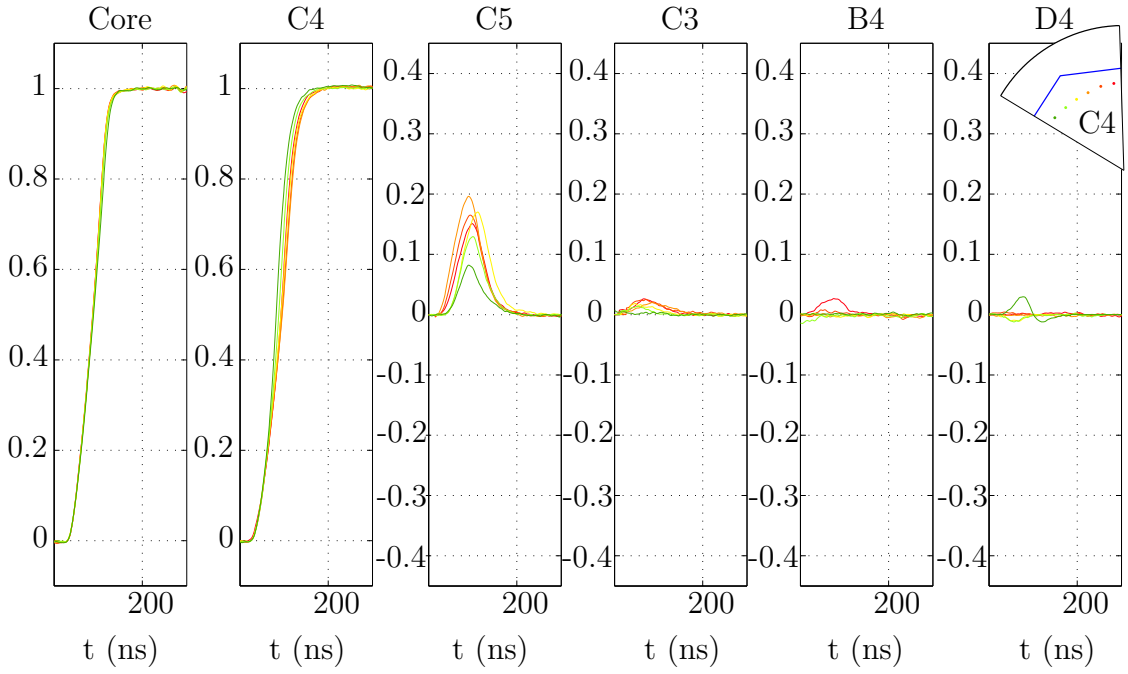

Figure 6.14: The 24 mm azimuthal line scan through Segment C4. The magnitude of the D4 transient charge increases as the interaction position moves within Segment C4 from Segment B4 toward Segment D4 (orange to green).

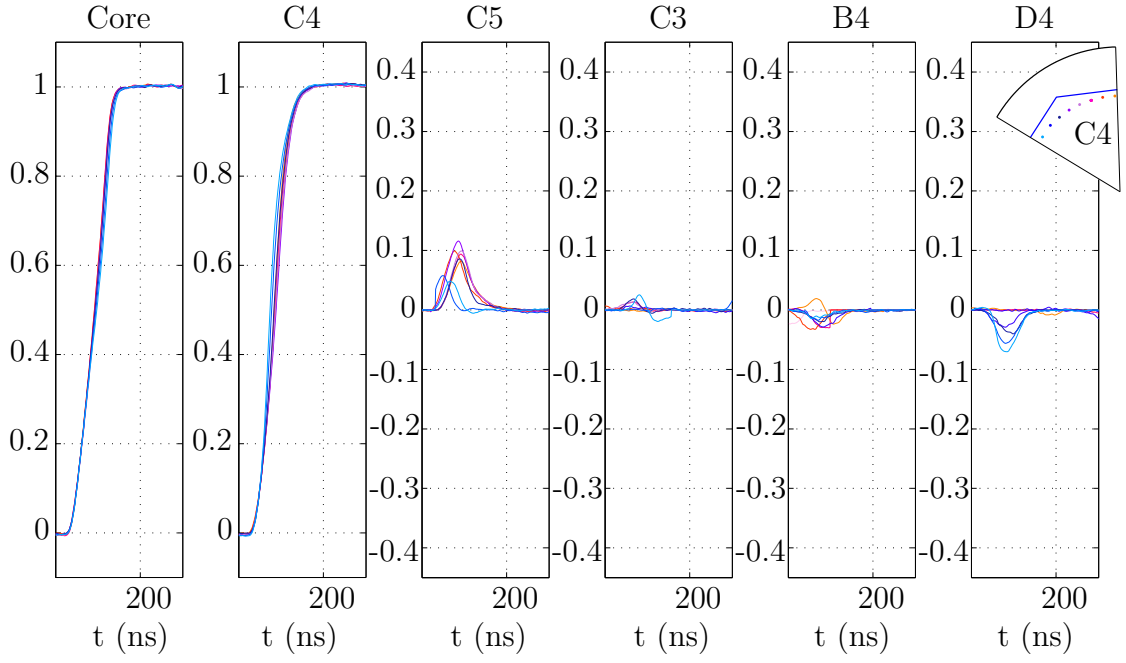

Figure 6.15: The 27 mm azimuthal line scan through Segment C4. The magnitude of the D4 transient charge increases as the interaction position moves within Segment C4 from segment B4 toward Segment D4 (orange to blue).

6.4.3 Experimental Position Sensitivity

The position sensitivity, Δs_{ij}^2, is calculated for the experimental database in the same manner as for the ADL sensitivity measurement, using Equation 5.6. Sensitivity is important as it reflects how well the pulse shape signals can be distinguished throughout detector position. For this calculation the core response, hit segment response and four neighbouring segment signals are included for each position.

$$\Delta s_{ij}^2 = \sum_{k=1}^{6} \sum_{t=t10}^{t90} \left[\frac{q(t)_i^k - q(t)_j^{-k}}{\sqrt{2}\sigma} \right]^2 \tag{6.1}$$

where $q(t)$ represents the signal amplitude at each sample position, and σ represents the standard deviation in the baseline signal, or the noise on the mean pulse. A high value of Δs_{ij}^2 represents a large sensitivity where the signal response of the detector is changing rapidly. The sensitivity was normalised to the maximum sensitivity within each scan line. The sensitivity as a function of position for the scan of Segment C4 is given in Fig. 6.16.

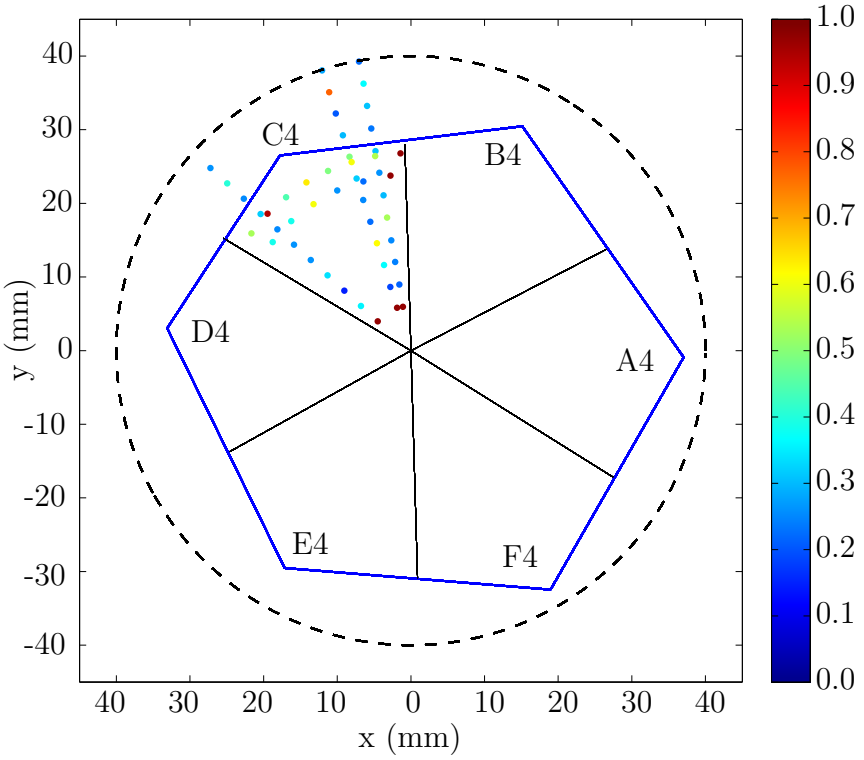

Figure 6.16: The experimental position sensitivity as a function of radius (left) and azimuthal angle (right). The lines show trend lines only and do not represent a fit.

The sensitivity results are also plotted as a function of line radius and azimuthal angle as well, shown in Fig. 6.16. The lines plotted on top of the data reflect the trend of the sensitivity measurement, not a calculated relationship

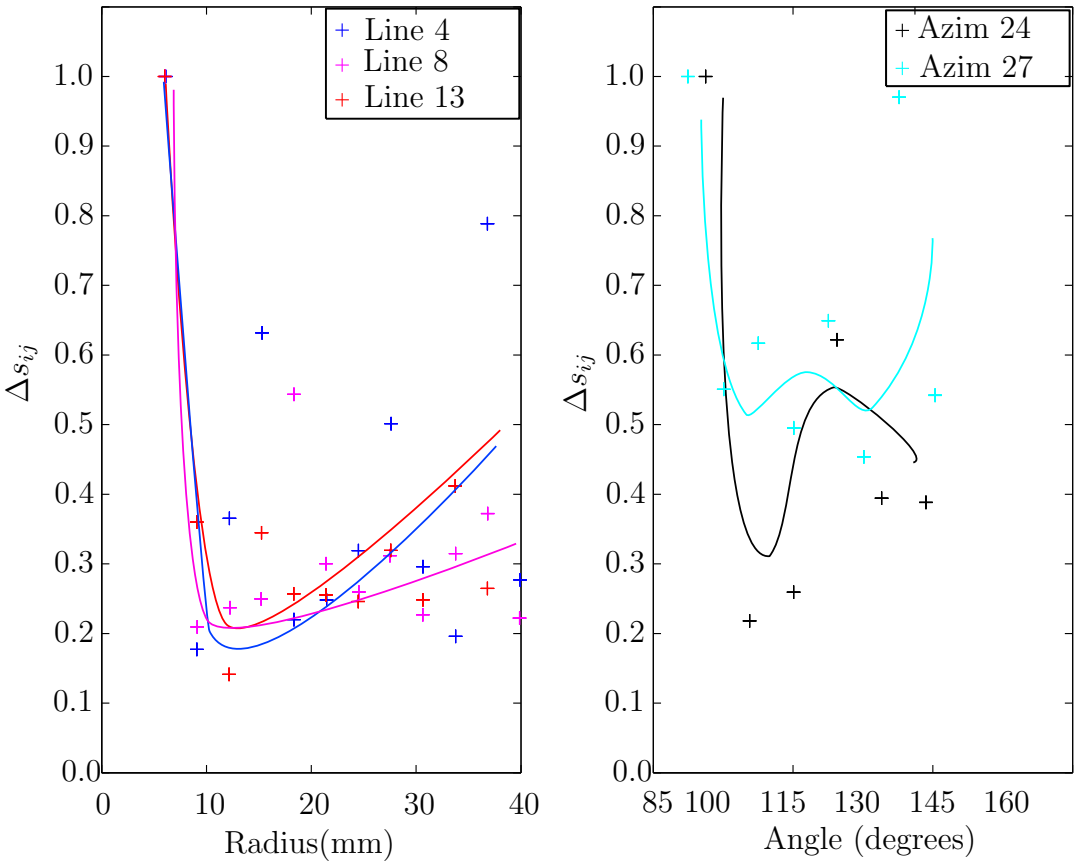

Figure 6.17: The experimental position sensitivity as a function of radius (left) and azimuthal angle (right). The lines show trend lines only and do not represent a fit.

The radial scan lines indicate that the sensitivity is greatest at the segment borders and that the detector sensitivity reduces at intermediate radii within the central region of the segments. The azimuthal scan result shows that in the central region of the segment the sensitivity increases. This is due to the change in transient charge signals within adjacent segments.

Upon examining the simulated results for the sensitivity within the ADL database, Fig 5.11, there is agreement that the sensitive regions of the detector occur along the segmentation boundaries, with less sensitivity at the centre of the contacts. This experimental sensitivity calculations show an agreement with the results shown for the ADL simulation, further described in Section 5.3.4.

6.5 Pulse Shape Comparison with ADL Database

The experimental database has been compared to the ADL simulation in the following section. An example of the experimental pulse shapes versus the ADL pulse shapes is shown in Fig. 6.18.

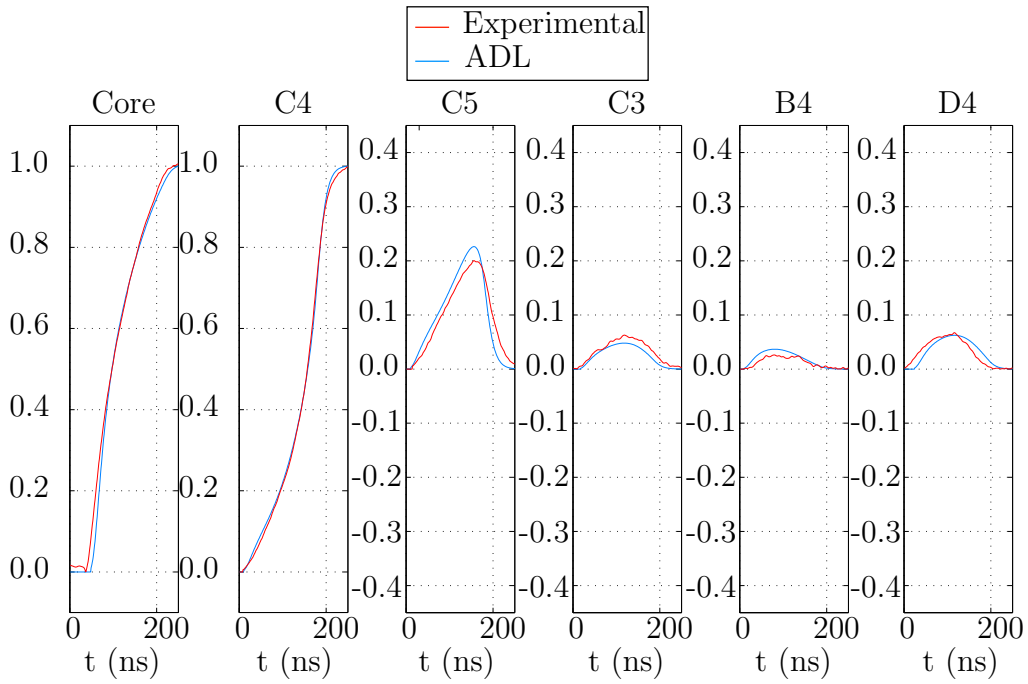

Figure 6.18: The experimental and ADL pulse shapes for radial line 4, position 1. The result shown is for Segment C4 and ADL depth 52 mm.

The overlaid pulse shapes indicate an excellent agreement in the risetime and transient signal magnitudes. In this figure, the transient signals are aligned to 0.05 magnitude position.

6.5.1 Position Resolution Results

The ultimate goal of the coincidence scan is to validate the ADL simulation with the experimental detector data.

In the RMS difference was calculated for the hit segment, C4, and the neighbouring segments between the experimental database and a range of ADL positions. The core and real charge signals were aligned at t50 for this measurement, and the transient signals were aligned at maximum amplitude.

The experimental pulse shapes were compared to a 2 mm database of ADL pulse shapes at Z depth = 52 mm, which showed the best agreement for Segment

C4. The minimum difference between signals searching within a 10 mm^2 range of ADL positions was calculated with Equation 6.2, where Δs^2 is the total difference in signals,

$$\Delta s^2 = \sum_{i=0}^{samples} \left[\frac{(ADL_i - Exp_i)^2}{samples} \right] \tag{6.2}$$

Quiver plots are generated for each detector ring showing the difference in experimental and ADL position for the minimum RMS value calculated. The results generated for the scan lines through Segment C4 is given in Fig. 6.19.

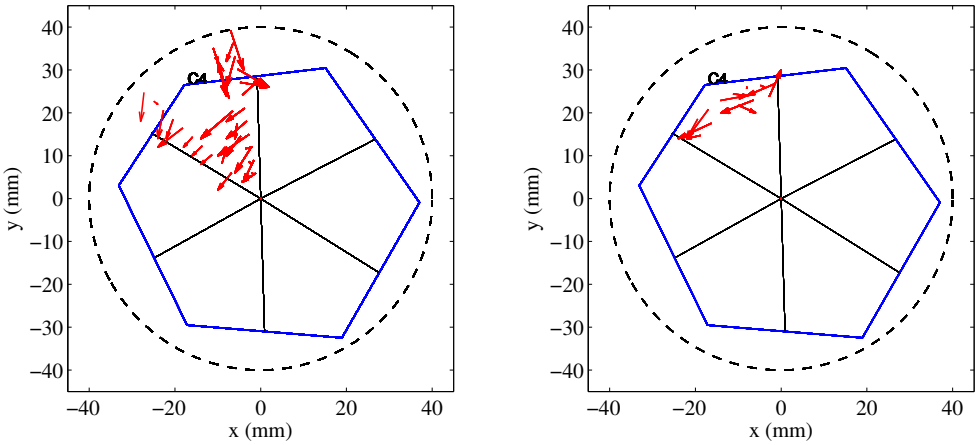

Figure 6.19: The difference in the minimal position between the experimental data and ADL azimuthal scans. A calculation of the mean displacement yields a value of dR = -5.6 mm.

The average displacement calculated Segment C4 between the experimental position and ADL position, dR = dX + dY + dZ = -5.6 mm. From the radial line quiver plots it appears that there is a systematic rotation in the position of the experimental pulses, resulting in a large number of the arrows which point toward neighbouring Segment D4.

Fig. 6.19 indicates that for this measurement the average dR position resolution achieved for the detector, 5.6 mm takes into account several large outlying RMS values. For the points at the edge of the detector segments, the position displacement is approximately 2.5 mm. With further examination, the large initial dR value could be inflated due to the small number of points, with respect to the entire detector, that are included in this calculation. Further work may include an examination of the entire database of pulse shapes.

Chapter 7

Summary

Two AGATA asymmetric detectors were scanned at the University of Liverpool Oliver Lodge Laboratory scanning table in order to study and compare their performance. Over a period of 3 months, experimental data was acquired in order to generate a database of signal responses. This data is used to validate a pulse shape database produced through the simulation library ADL.

The uniformity in performance of the detectors supplied by Canberra is essential for the AGATA project. In order to verify this, the energy resolution, efficiency and charge collection response of the AGATA capsules A004 and A006 have been compared directly. The energy resolution and efficiency were measured to be within the AGATA specifications. The core energy resolution measurement yielded FWHM of 2.10 keV at 1332 keV for A004 and 2.06 keV for A006.

The collimated photon scans of the two detectors indicated excellent uniformity of response throughout each ring over the surface of the HPGe crystals. A comparison of transient charge response of both A004 and A006 gave good agreement.

The depletion as a function of bias voltage has been compared quantitatively between detectors A004 and A006, showing that the impurity concentration has an effect on the rate of depletion of the detector. For lower impurity concentration, the detector depletes more readily. The performance of the detector at bias voltages lower than the operating voltage was also examined. This study showed that the photopeak position gain shifts to lower values as the bias voltage is lowered. The resolution worsens as the detector becomes undepleted at reduced bias voltages.

The pulse shape response of AGATA has been studied using the ADL sim-

ulation, indicating that the sensitivity of response is dependant upon detector position. The most sensitive region, where the pulse shape and transient response is changing more readily, is found to be at the segment boundaries and the front region of the detector.

The experimental pulse shape database generated for AGATA detector A006 utilised the Liverpool coincidence scanning system. The experimental database response was quantified, indicating the variation in sensitivity throughout a region of the detector. The ADL simulation of A006 was compared to the experimental database. The measurement yielded an average displacement, dR, between the two data sets of 5.6 mm. This value may be investigated further by validating the entire experimental detector library against the simulated database.

7.1 Further Work

The comparison of detectors A004 and A006 has given detailed information on the uniformity of performance. It is recommended that future work should include measurements on the crystallographic axis and depletion as well as a detector response on the next AGATA crystals scanned at the University of Liverpool with a 60 keV ^{241}Am collimated source. This will enable detailed study of the capsule.

Several experimental parameters may be included in this analysis in order to improve the comparison between the ADL simulation and the experimental data, including possible capsule rotation and electronic crosstalk. A calculation of the crosstalk for the detector A004 and A006 is possible and has been performed for detector C001 previously [49].

This work will be utilised by the collaboration in order to improve understanding of the response of the AGATA capsules as well as the validity of PSA calculations utilised in nuclear structure experiments.

Appendix A

Singles Images

The full collection of front face figures are given in this section. They are included for interest and completeness.

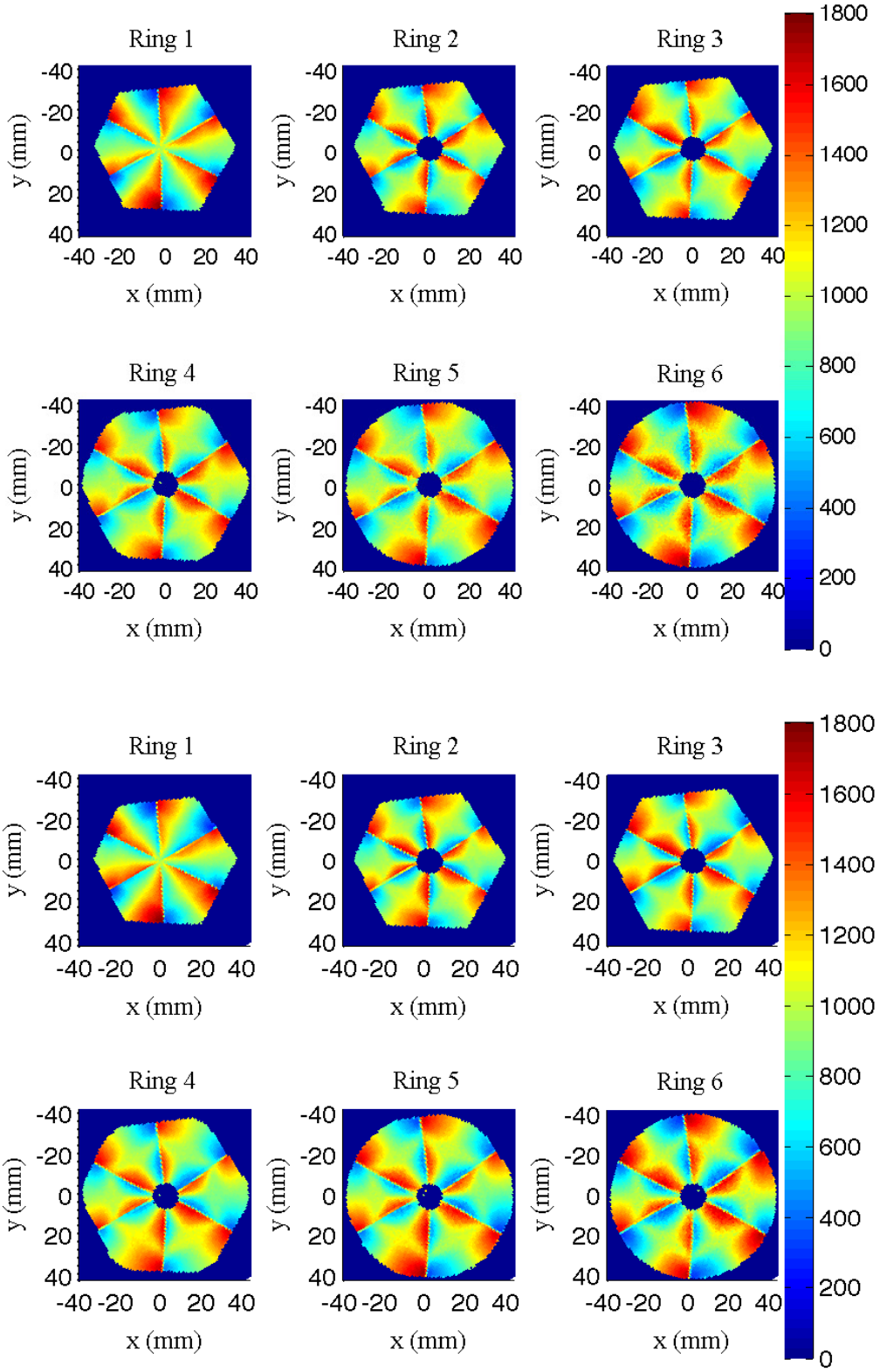

Figure A.1: A004 (top) and A006 (bottom) clockwise/anticlockwise average image charge asymmetry per position.

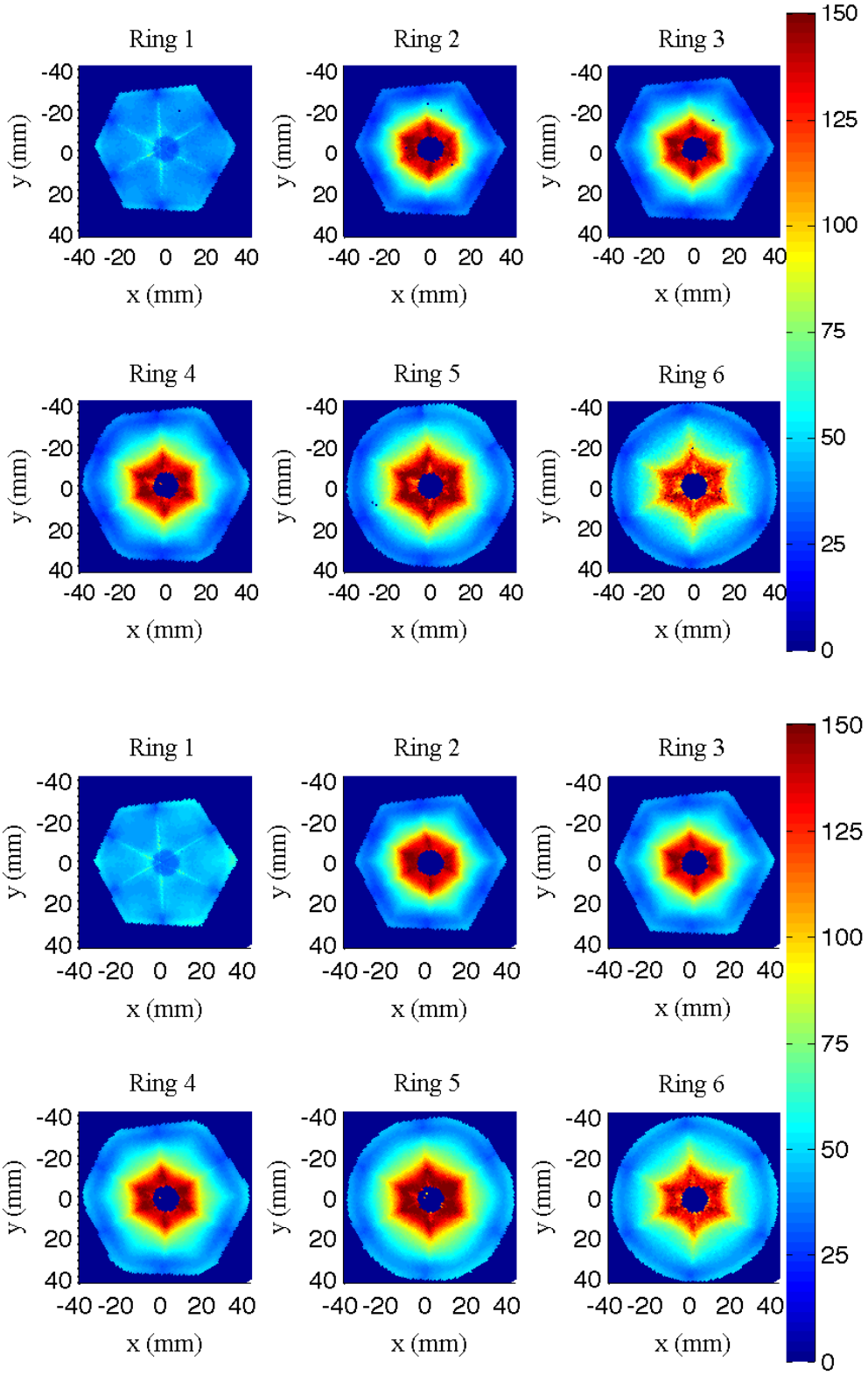

Figure A.2: A004 (top) and A006 (bottom) T30 segment risetime. The T30 segment rise times clearly illustrate the 6-fold symmetry of the detector.

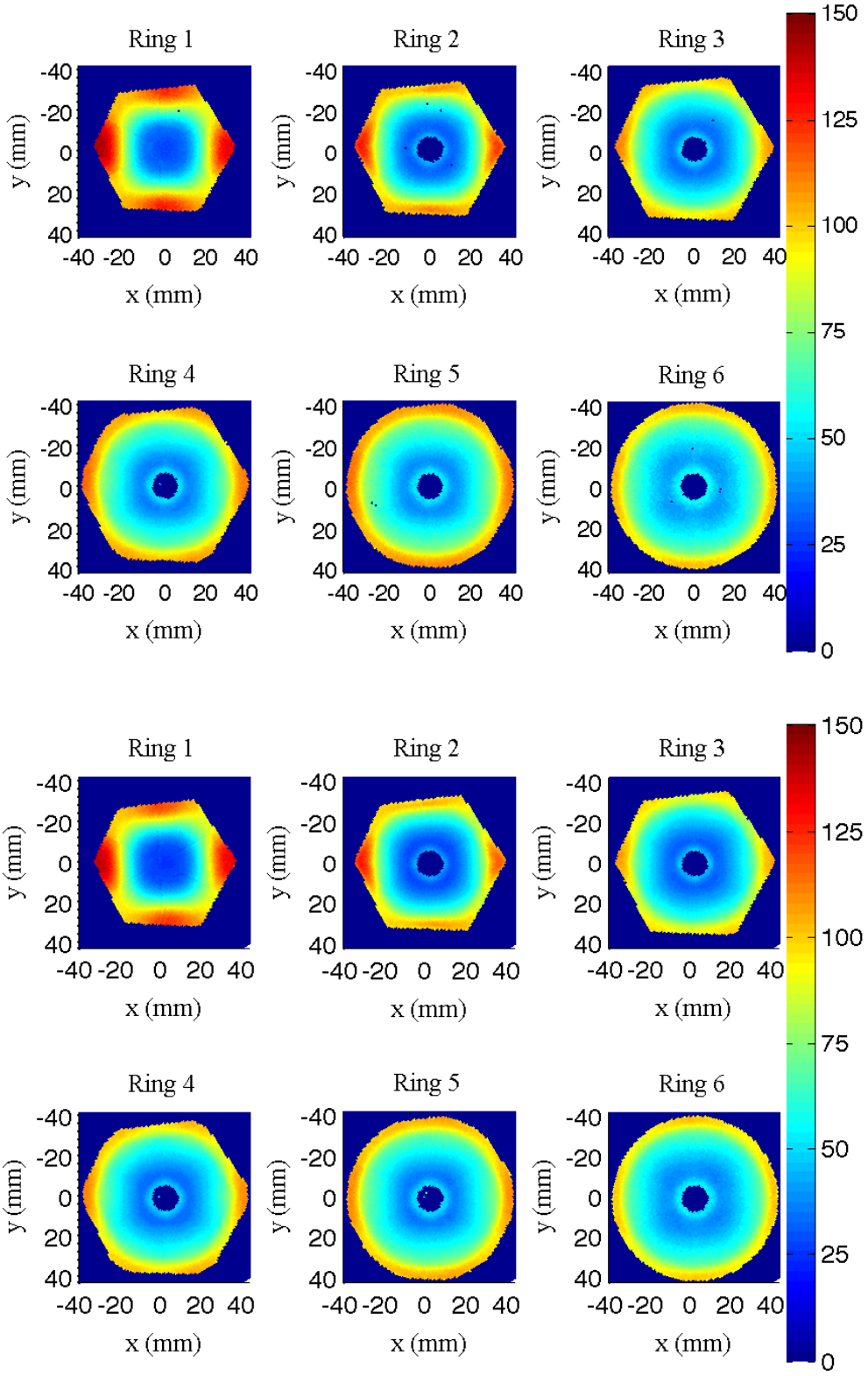

Figure A.3: A004 (top) and A006 (bottom) T30 core risetime. The T30 for every ring is shown. The 4-fold symmetry of the crystal axis is clearly observed. A more detailed discussion is included on Section 4.5

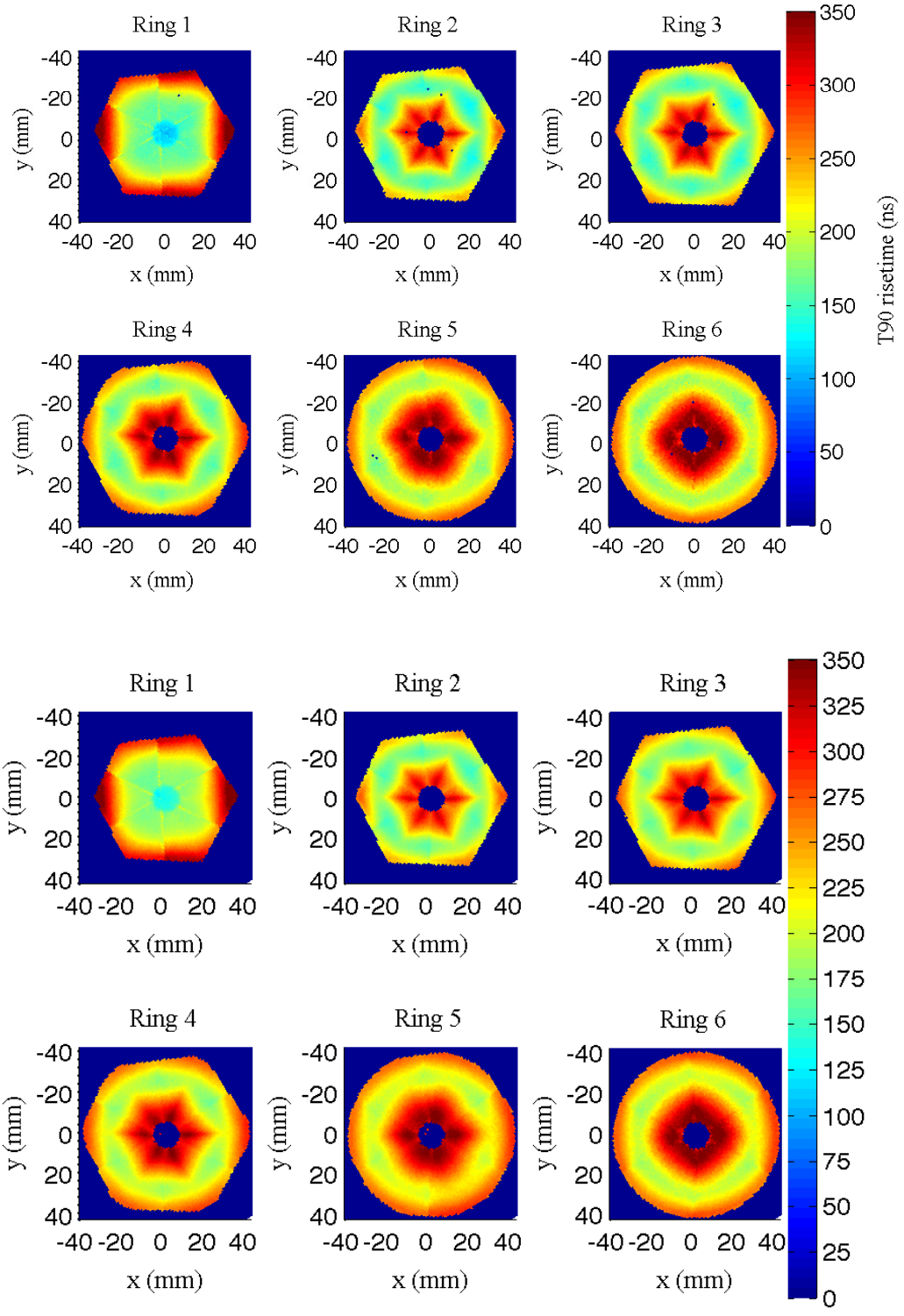

Figure A.4: A004 (top) and A006 (bottom) T90 Segment Risetime. The T90 segment risetimes illustrate the discontinuation of segmentation across the crystal due to a greater dependance of charge collection on the anisotropic drift velocity

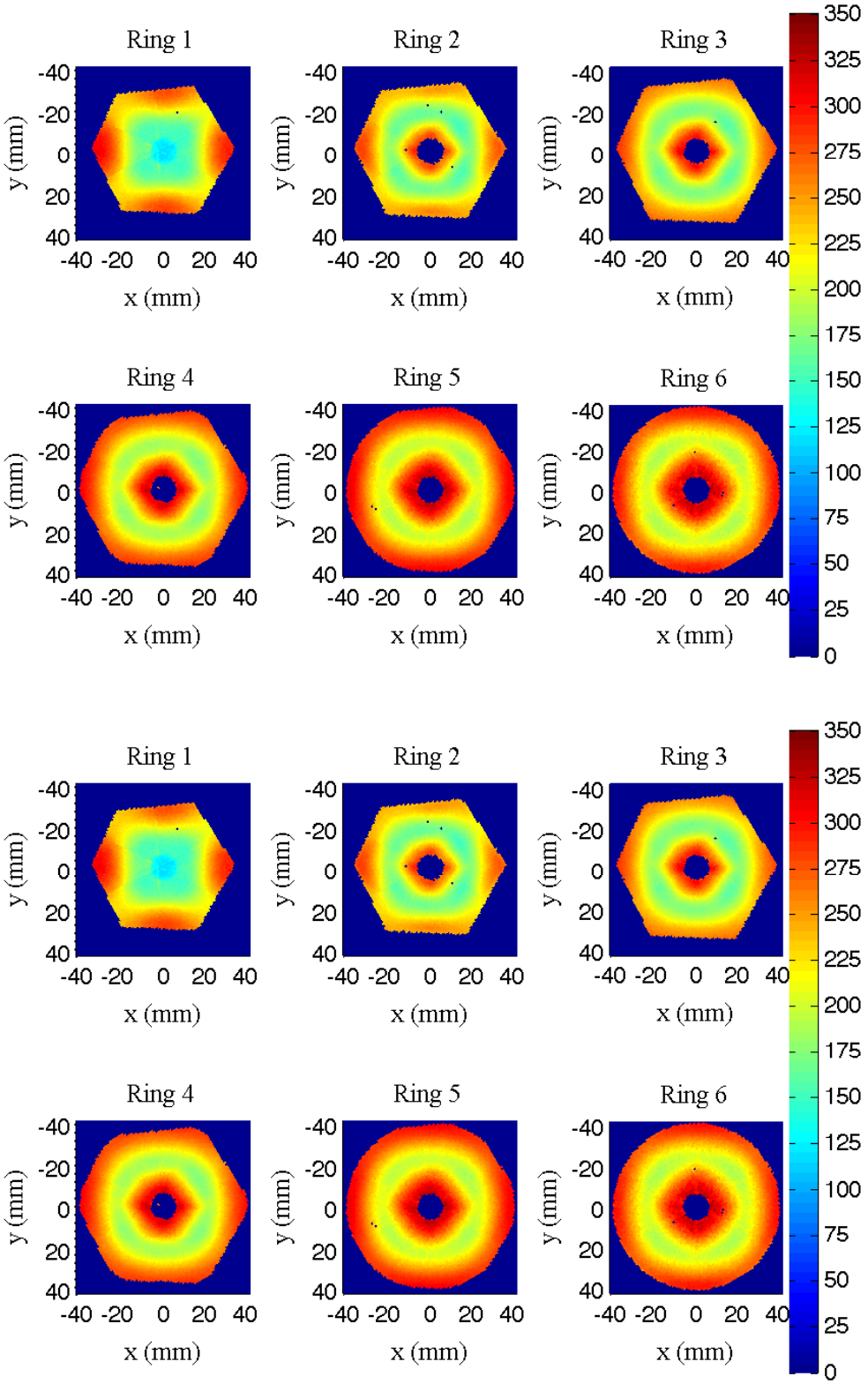

Figure A.5: A004 (top) and A006 (bottom) T90 Core Risetime. A more detailed discussion is included on Section 4.5

Appendix B

Reduced Bias Scan Images

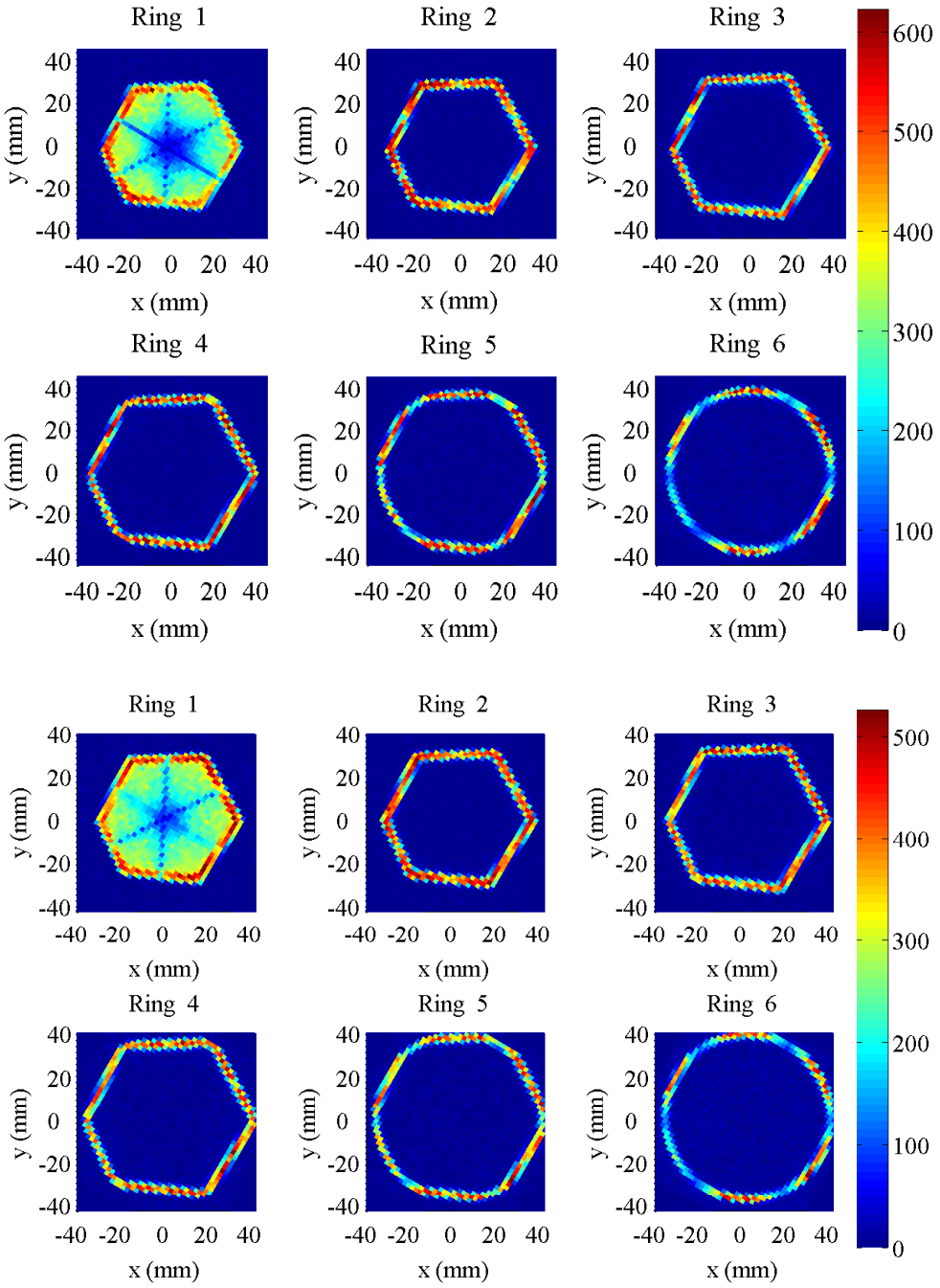

Figure B.1: A004 (top) and A006 (bottom) photopeak intensity per position at **50 V**. A more detailed discussion is included on Section 4.7.

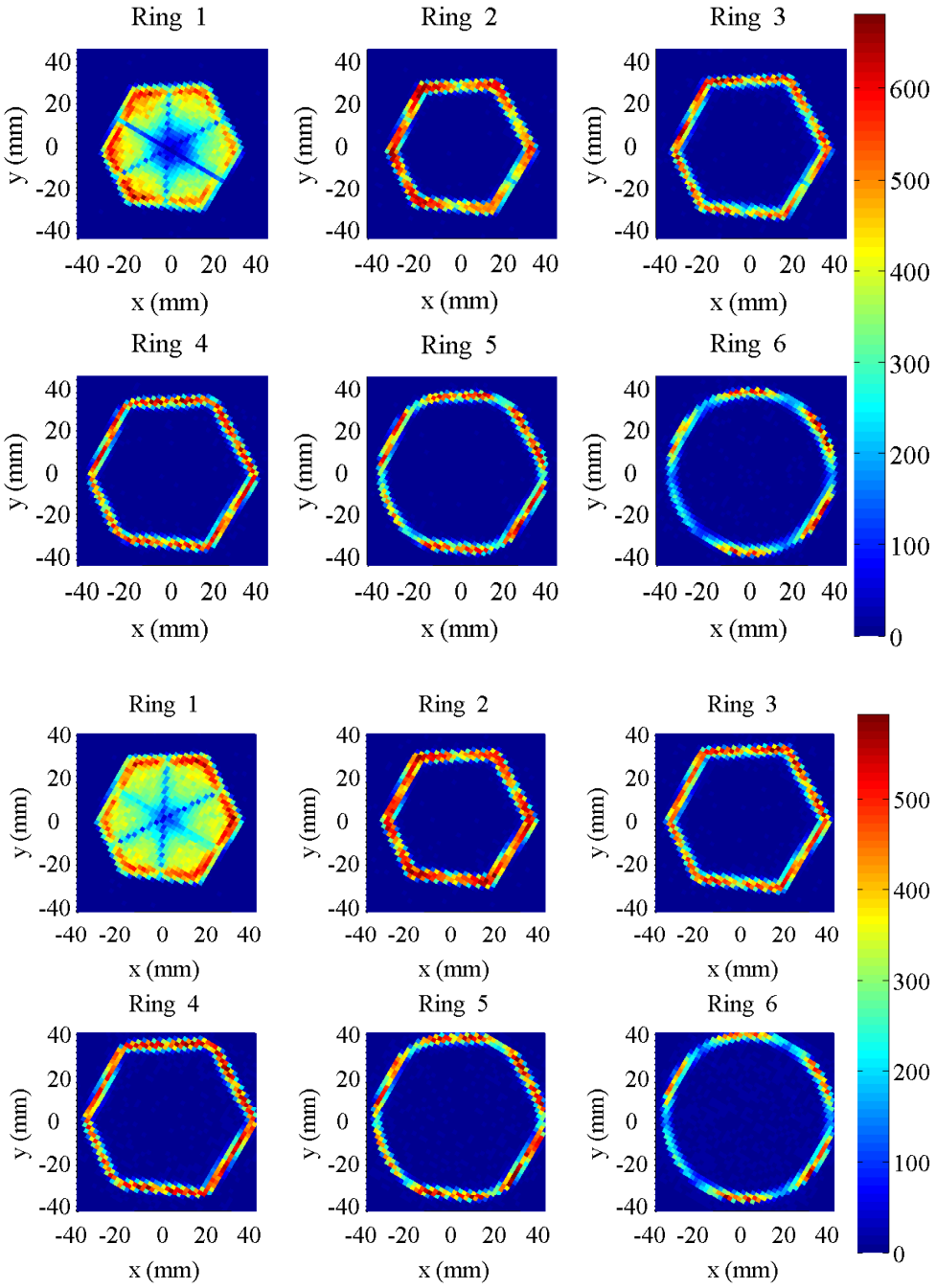

Figure B.2: A004 (top) and A006 (bottom) photopeak intensity per position at **100 V**. A more detailed discussion is included on Section 4.7.

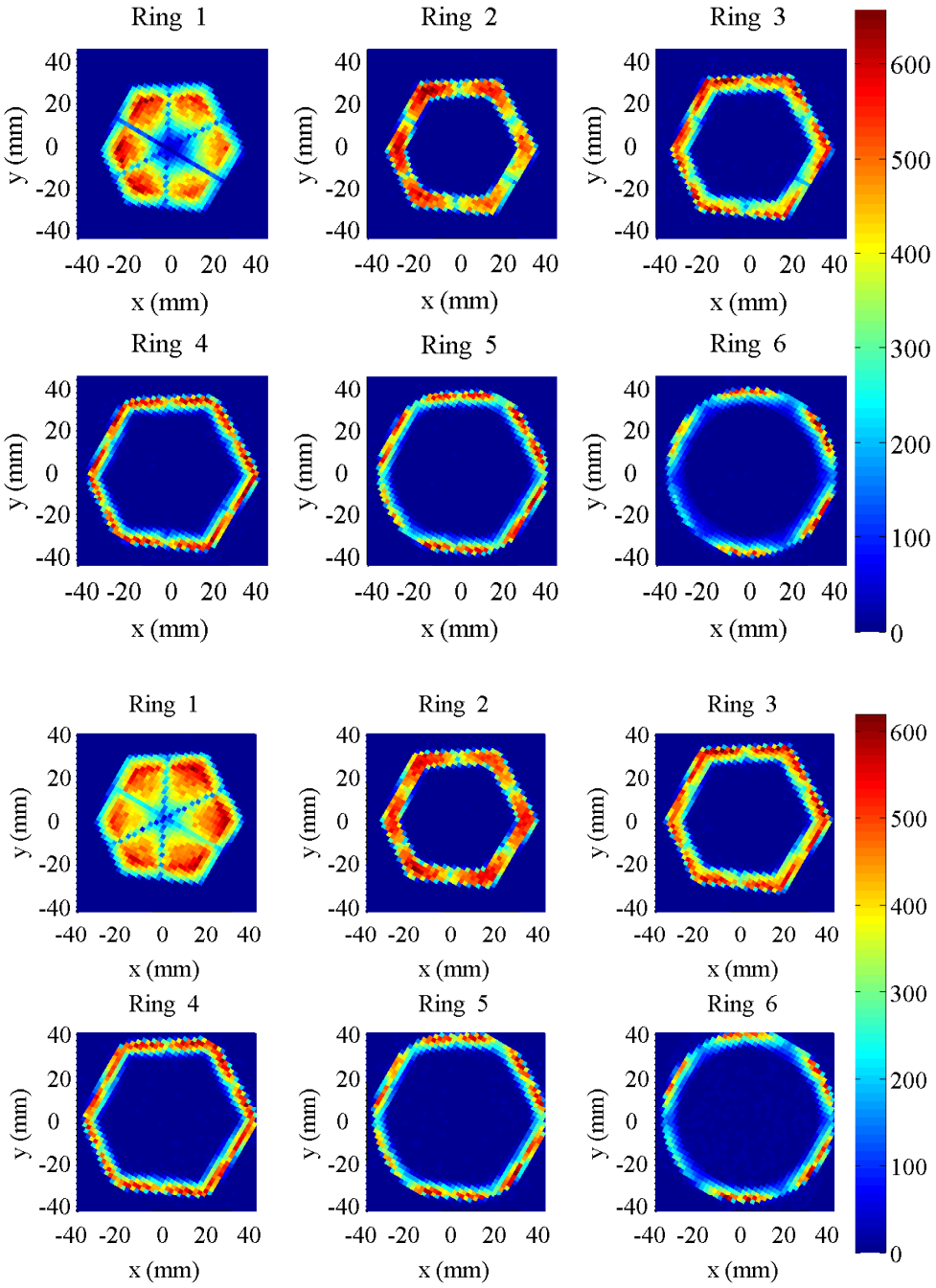

Figure B.3: A004 (top) and A006 (bottom) photopeak intensity per position at **250 V**. A more detailed discussion is included on Section 4.7.

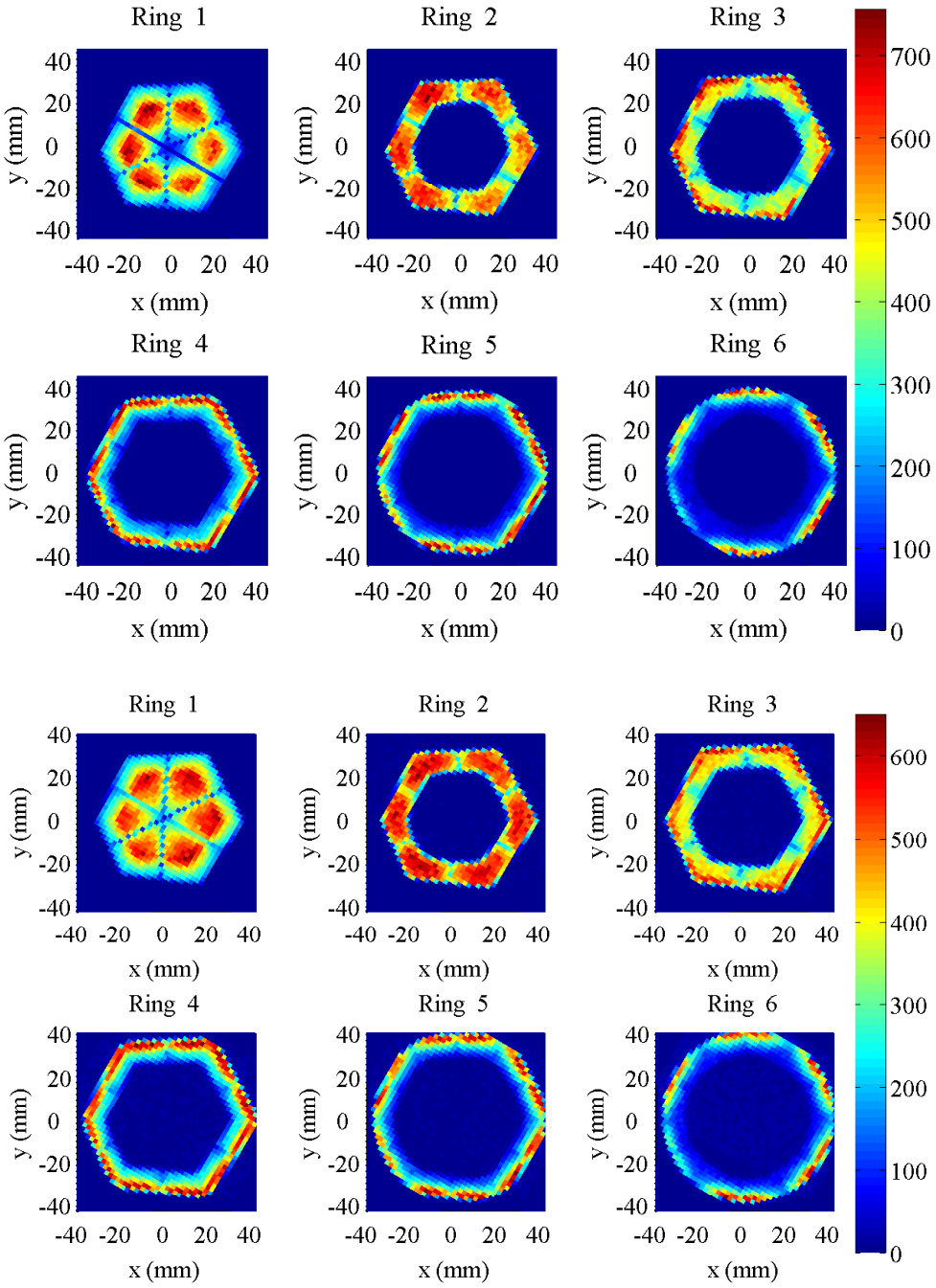

Figure B.4: A004 (top) and A006 (bottom) photopeak intensity per position at **500 V**. A more detailed discussion is included on Section 4.7.

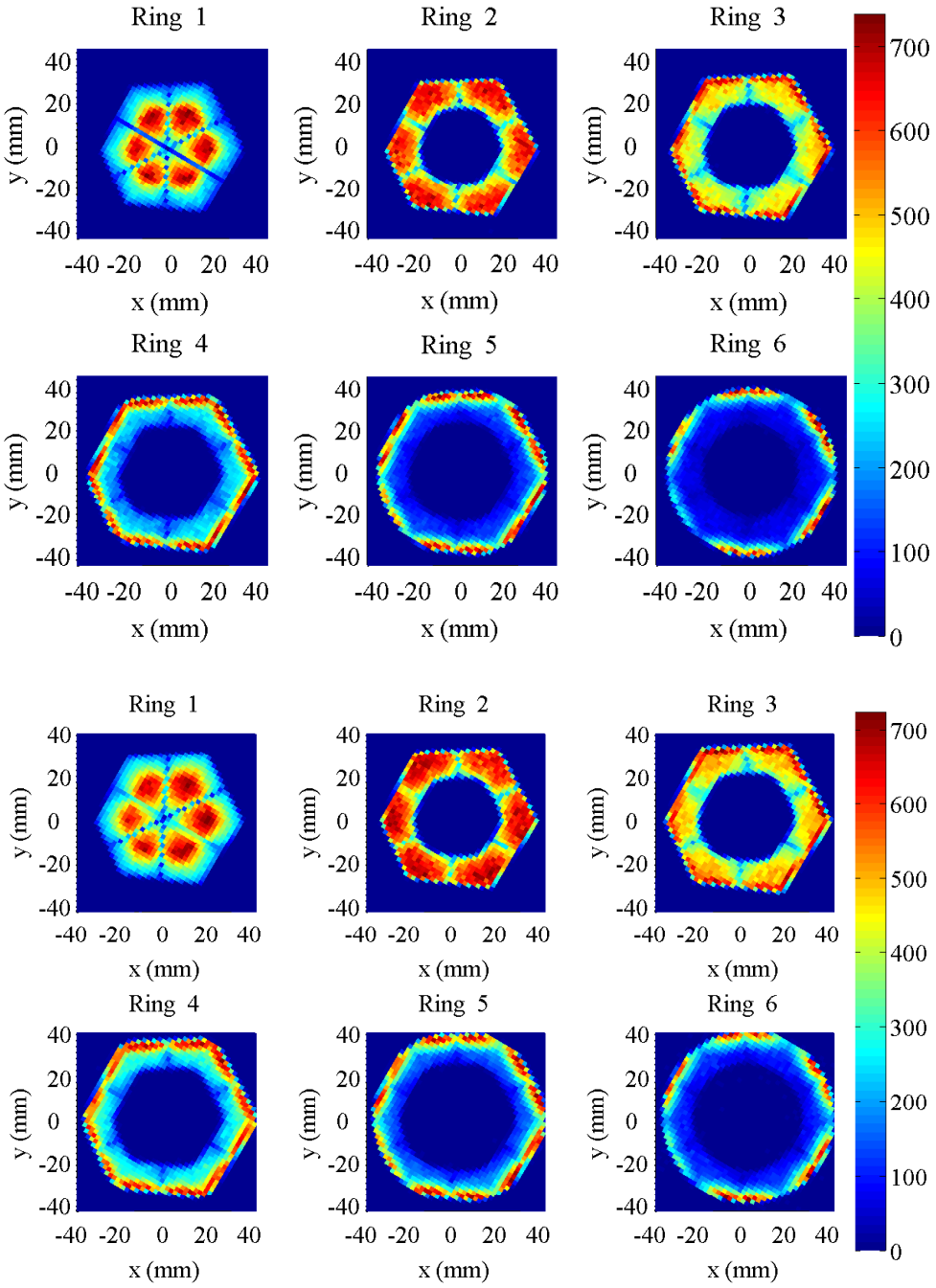

Figure B.5: A004 (top) and A006 (bottom) photopeak intensity per position at **750 V**. A more detailed discussion is included on Section 4.7.

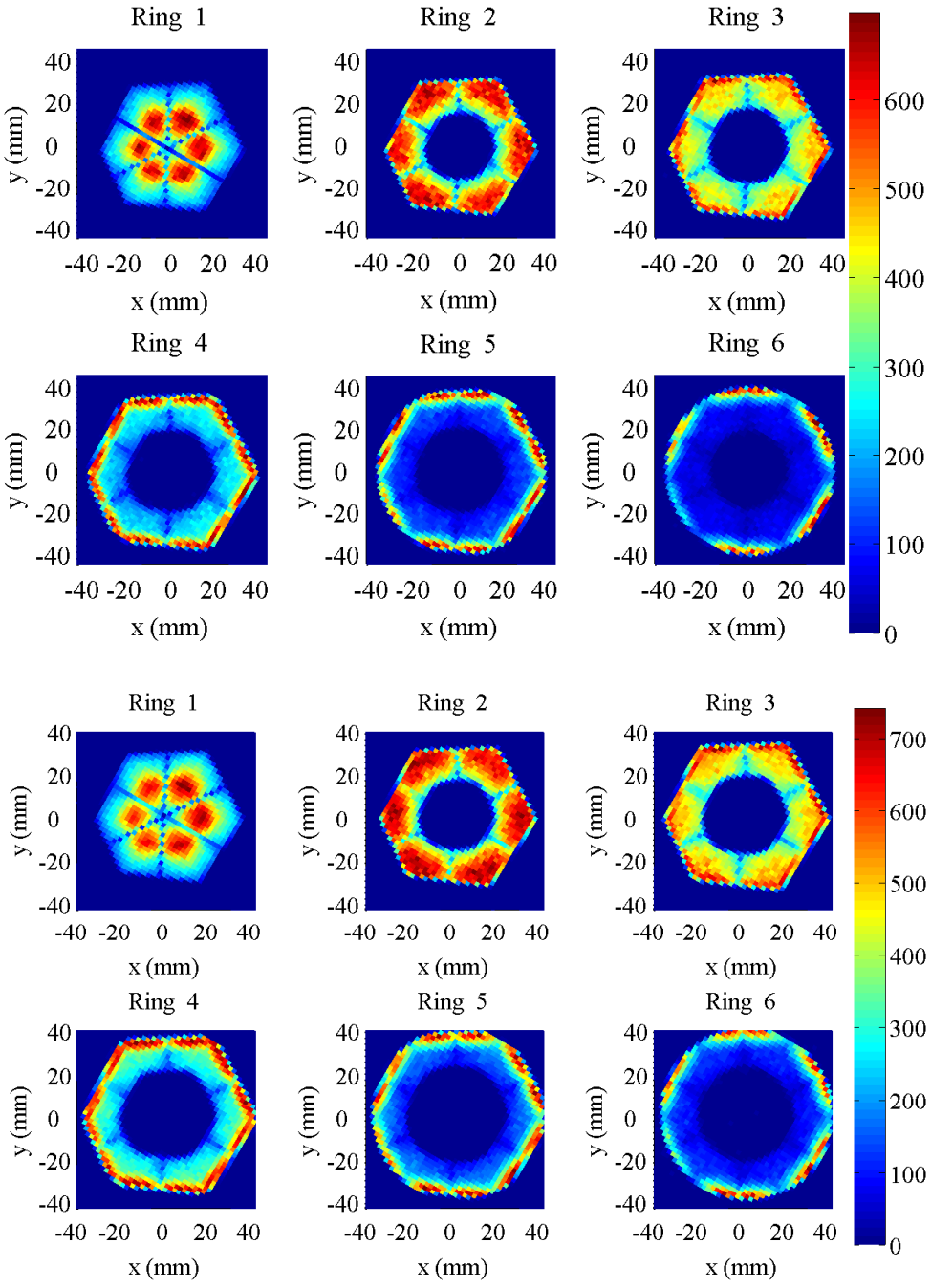

Figure B.6: A004 (top) and A006 (bottom) photopeak intensity per position at **1000 V**. A more detailed discussion is included on Section 4.7.

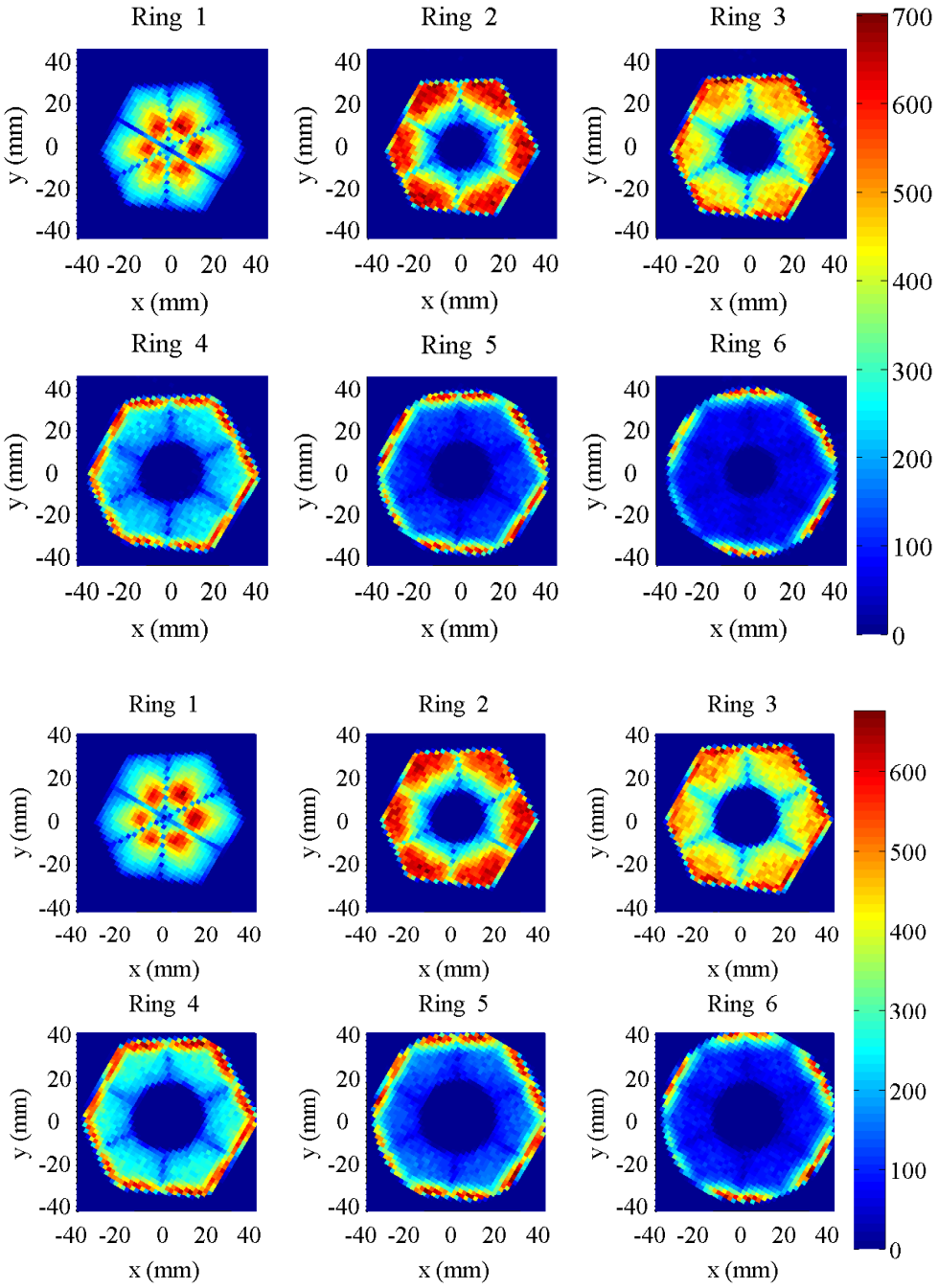

Figure B.7: A004 (top) and A006 (bottom) photopeak intensity per position at **1500 V**. A more detailed discussion is included on Section 4.7.

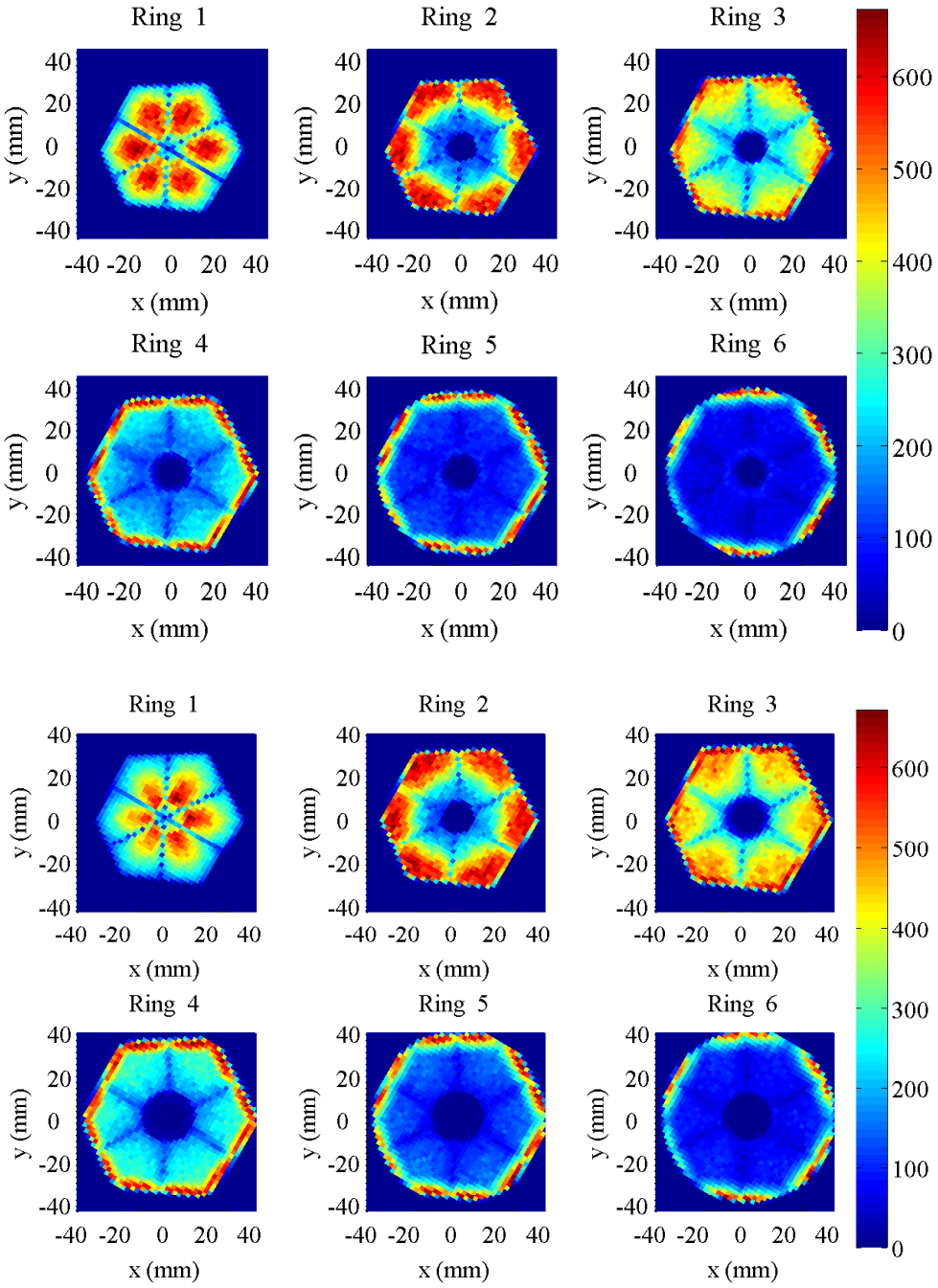

Figure B.8: A004 (top) and A006 (bottom) photopeak intensity per position at **2000 V**. A more detailed discussion is included on Section 4.7.

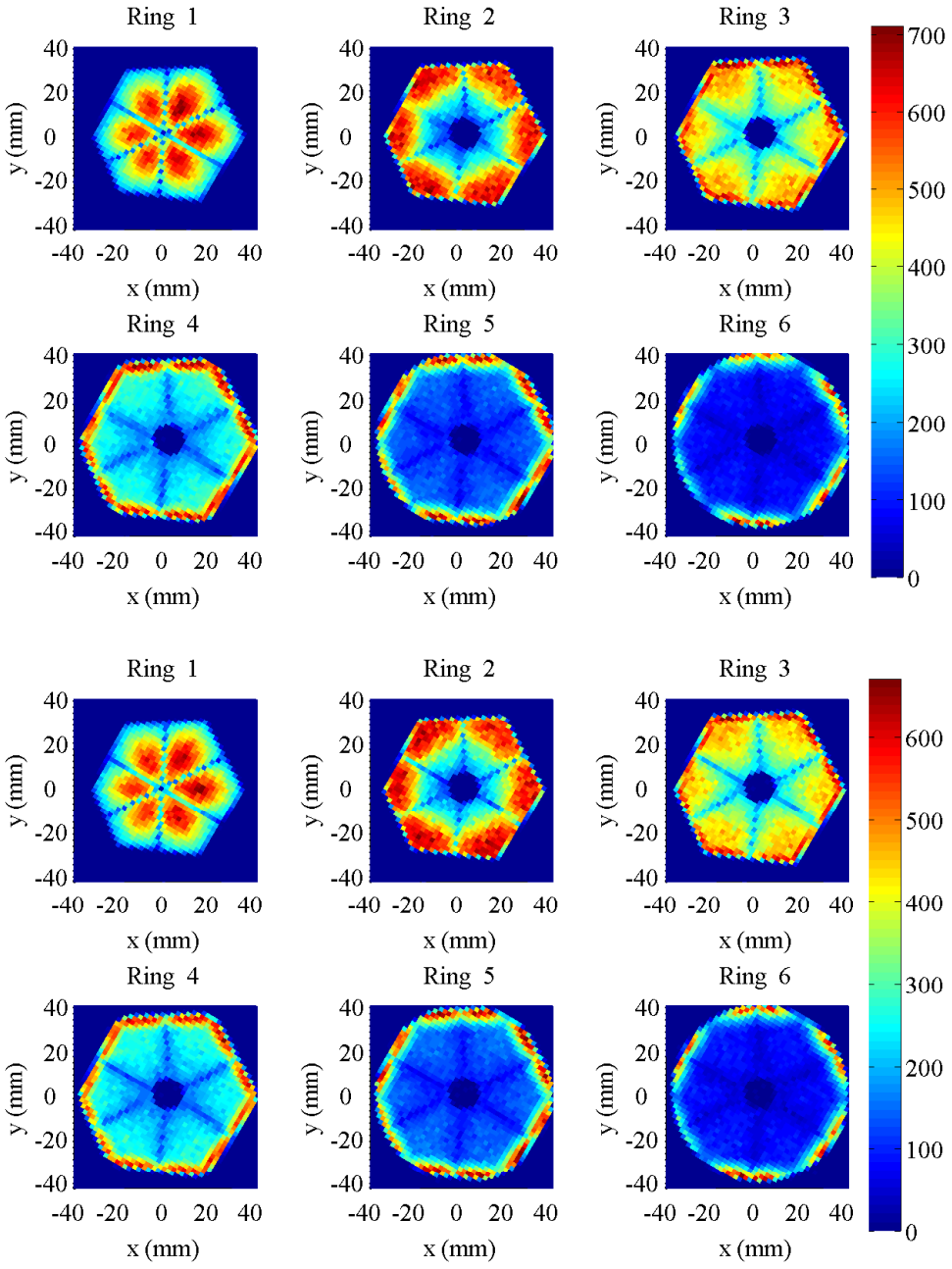

Figure B.9: A006 photopeak intensity per position at **3000V** (top) and **4000 V** (bottom). A more detailed discussion is included on Section 4.7.

Appendix C

Capsule Manual Data Sheet

Canberra has provided tested segment resolution values as well as efficiency values for each detector, which are specified below.

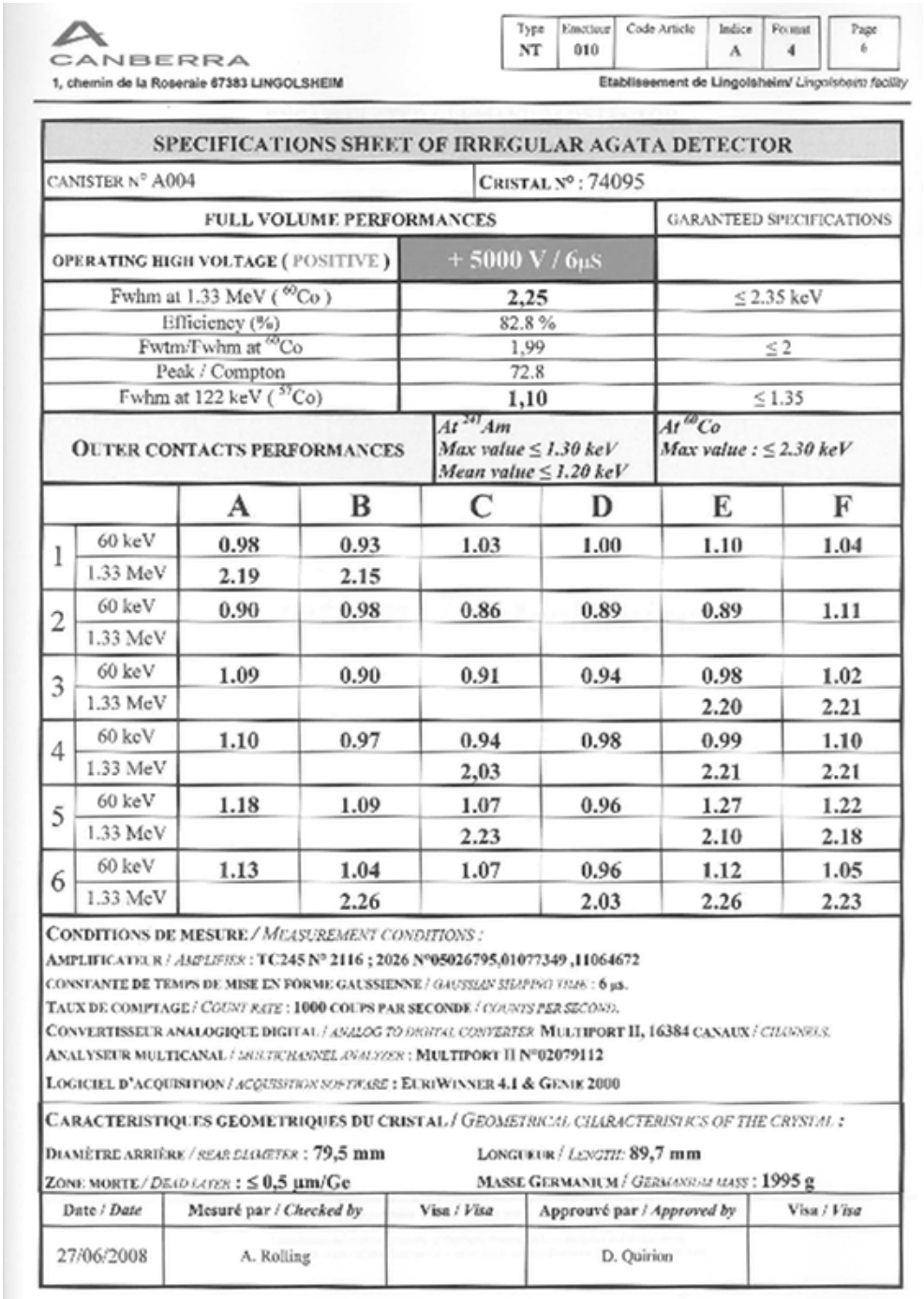

CANBERRA

1, chemin de la Roseraie 67383 LINGOLSHEIM

Type	Emetteur	Code Article	Indice	Format	Page
NT	010		A	4	6

Etablissement de Lingolsheim/ *Lingolsheim facility*

SPECIFICATIONS SHEET OF IRREGULAR AGATA DETECTOR

CANISTER N° A004 — CRISTAL N° : 74095

FULL VOLUME PERFORMANCES		GARANTEED SPECIFICATIONS
OPERATING HIGH VOLTAGE (POSITIVE)	+ 5000 V / 6µS	
Fwhm at 1.33 MeV (^{60}Co)	2,25	≤ 2.35 keV
Efficiency (%)	82.8 %	
Fwtm/Fwhm at ^{60}Co	1,99	≤ 2
Peak / Compton	72.8	
Fwhm at 122 keV (^{57}Co)	1,10	≤ 1.35

OUTER CONTACTS PERFORMANCES	*At ^{241}Am* *Max value ≤ 1.30 keV* *Mean value ≤ 1.20 keV*	*At ^{60}Co* *Max value : ≤ 2.30 keV*

		A	B	C	D	E	F
1	60 keV	0.98	0.93	1.03	1.00	1.10	1.04
	1.33 MeV	2.19	2.15				
2	60 keV	0.90	0.98	0.86	0.89	0.89	1.11
	1.33 MeV						
3	60 keV	1.09	0.90	0.91	0.94	0.98	1.02
	1.33 MeV					2.20	2.21
4	60 keV	1.10	0.97	0.94	0.98	0.99	1.10
	1.33 MeV			2,03		2.21	2.21
5	60 keV	1.18	1.09	1.07	0.96	1.27	1.22
	1.33 MeV			2.23		2.10	2.18
6	60 keV	1.13	1.04	1.07	0.96	1.12	1.05
	1.33 MeV		2.26		2.03	2.26	2.23

CONDITIONS DE MESURE / *MEASUREMENT CONDITIONS :*

AMPLIFICATEUR / *AMPLIFIER* : TC245 N° 2116 ; 2026 N°05026795,01077349 ,11064672

CONSTANTE DE TEMPS DE MISE EN FORME GAUSSIENNE / *GAUSSIAN SHAPING TIME* : 6 µs.

TAUX DE COMPTAGE / *COUNT RATE* : 1000 COUPS PAR SECONDE / *COUNTS PER SECOND.*

CONVERTISSEUR ANALOGIQUE DIGITAL / *ANALOG TO DIGITAL CONVERTER* MULTIPORT II, 16384 CANAUX / *CHANNELS.*

ANALYSEUR MULTICANAL / *MULTICHANNEL ANALYZER* : MULTIPORT II N°02079112

LOGICIEL D'ACQUISITION / *ACQUISITION SOFTWARE* : EURIWINNER 4.1 & GENIE 2000

CARACTERISTIQUES GEOMETRIQUES DU CRISTAL / *GEOMETRICAL CHARACTERISTICS OF THE CRYSTAL :*

DIAMÈTRE ARRIÈRE / *REAR DIAMETER* : 79,5 mm — LONGUEUR / *LENGTH*: 89,7 mm

ZONE MORTE / *DEAD LAYER* : ≤ 0,5 µm/Ge — MASSE GERMANIUM / *GERMANIUM MASS* : 1995 g

Date / *Date*	Mesuré par / *Checked by*	Visa / *Visa*	Approuvé par / *Approved by*	Visa / *Visa*
27/06/2008	A. Rolling		D. Quirion	

Figure C.1: A004 Canberra detector specifications. The segment labelling scheme is translated between Canberra (ABCDEF) to AGATA (AFEDCB).

CANBERRA
1, chemin de la Roseraie 67383 LINGOLSHEIM

Type	Directeur	Code Article	Indice	Format	Page
NT	010		A	4	6

Etablissement de Lingolsheim/ *Lingolsheim facility*

SPECIFICATIONS SHEET OF IRREGULAR AGATA DETECTOR

CANISTER N° A006	CRISTAL N° : 74096	
FULL VOLUME PERFORMANCES		GARANTEED SPECIFICATIONS
OPERATING HIGH VOLTAGE (POSITIVE)	+ 5000 V / 6µS	
Fwhm at 1.33 MeV (^{60}Co)	2.06	≤ 2.35 keV
Efficiency (%)	79 %	
Fwtm/Fwhm at ^{60}Co	1.88	≤ 2
Peak / Compton	78.1	
Fwhm at 122 keV (^{57}Co)	1.02	≤ 1.35
OUTER CONTACTS PERFORMANCES	*At ^{241}Am* *Max value ≤ 1.30 keV* *Mean value ≤ 1.20 keV*	*At ^{60}Co* *Max value : ≤ 2.30 keV*

		A	B	C	D	E	F
1	60 keV	1.13	0.89	0.89	0.86	1.01	1.04
	1.33 MeV		2.21	2.16			
2	60 keV	0.97	0.89	0.87	0.94	0.82	1.20
	1.33 MeV		2.05	2.06			
3	60 keV	1.14	0.86	0.87	0.94	0.84	1.20
	1.33 MeV		2.16			1.99	2.02
4	60 keV	1.08	0.90	0.89	1.08	0.82	0.92
	1.33 MeV			2,03			1,90
5	60 keV	1.15	0.92	1.00	0.89	0.96	1.16
	1.33 MeV			2.28			
6	60 keV	1.06	0.94	0.93	0.80	0.88	0,83
	1.33 MeV		2.28			2.08	

CONDITIONS DE MESURE / *MEASUREMENT CONDITIONS :*
AMPLIFICATEUR / *AMPLIFIER* : **2026** N° 01078568, 01078729, 01078569, **2025** N° 04026103.
CONSTANTE DE TEMPS DE MISE EN FORME GAUSSIENNE / *GAUSSIAN SHAPING TIME* : **6 µs.**
TAUX DE COMPTAGE / *COUNT RATE* : **1000 COUPS PAR SECONDE** / *COUNTS PER SECOND.*
CONVERTISSEUR ANALOGIQUE DIGITAL / *ANALOG TO DIGITAL CONVERTER* : **MULTIPORT II N° 11065396, 16384 CANAUX** / *CHANNELS.*
ANALYSEUR MULTICANAL / *MULTICHANNEL ANALYZER* : **MULTIPORT II N° 11065396**
LOGICIEL D'ACQUISITION / *ACQUISITION SOFTWARE* : **GENIE 2K, EURIWINNER 4.1**
CARACTERISTIQUES GEOMETRIQUES DU CRISTAL / *GEOMETRICAL CHARACTERISTICS OF THE CRYSTAL :*

DIAMETRE ARRIERE / *REAR DIAMETER* : **79,6 mm** — LONGUEUR / *LENGTH* **89,6 mm**
ZONE MORTE / *DEAD LAYER* : **≤ 0,5 µm/Ge** — MASSE GERMANIUM / *GERMANIUM MASS* : **1995 g**

Date / *Date*	Mesuré par / *Checked by*	Visa / *Visa*
27-11-2008	Mustapha ALLALI	

Figure C.2: A006 Canberra detector specifications. The segment labelling scheme is translated between Canberra (ABCDEF) to AGATA (AFEDCB)

Bibliography

[1] I. Y. Lee, M. A. Deleplanque, and K. Vetter, Rep. Prog. Phys. **66**, 1095 (2003).

[2] J. Eberth and J. Simpson, Prog. Part. Nucl. Phys. **60**, 283 (2008).

[3] P. J. Nolan for the U.K.-France EUROGAM Collaboration, Nuclear Physics A **520**, c657 (1990).

[4] F. A. Beck, Prog. Part. Nucl. Phys. **28**, 443 (1992).

[5] I. Y. Lee, Prog. Part. Nucl. Phys. **28**, 473 (1992).

[6] J. Simpson, Z Phys. **358**, 139 (1997).

[7] P.J. Nolan and F.A. Beck and D.B. Fossan, Ann. Rev. Nucl. Part. Sci **45**, 561 (1994).

[8] G.C. Ball and A. Andreyev et al., Nucl. Phys. A **787**, 118 (2007).

[9] J.Simpson et al., Acta Physica Hungarica, Heavy Ion Physics , 159 (2000).

[10] J. Eberth et al., Prog. Part. Nucl. Phys. **46**, 389 (2001).

[11] I. Y. Lee, Nucl. Inst. Meth. A **422**, 195 (1999).

[12] J. Simpson, ACTA Physics Polonica B **36** (2005).

[13] S. Akkoyun et al., Nucl. Inst. Meth. A **668**, 26 (2012).

[14] A. Lopez-Martens, K. Hauschild, A. Korichi, J. Roccaz, and J.-P. Thibaud, Nucl. Inst. Meth. A **533**, 454 (2004).

[15] E. Farnea et al., Nucl. Inst. Meth. A **621**, 331 (2010).

[16] D. Bazzacco, Nucl. Phys. A **746**, 248 (2004).

[17] E. Farnea and A. Latina, Monte carlo simulations of the agata demonstrator array coupled to the prisma magnetic spectrometer, Technical report, LNL-INFN, 2007.

[18] A. Olariu et al., IEEE Trans. Nucl. Sci **53**, 1028 (2006).

[19] W. R. Leo, *Techniques for Nuclear and Particle Physics Experiments: A How-to Approach*, Springer-Verlag, Berlin, 2nd edition, 1987.

[20] R. Evans, *The Atomic Nucleus*, McGraw-Hill, 1955.

[21] O. Klein and Y. Nishina, Z. Phys. **52**, 853 (1929).

[22] G. F. Knoll, *Radiation Detection and Measurement*, John Wiley and Sons, Inc, USA, 3rd edition, 2000.

[23] H. R. Bilger, Phys. Rev. **163**, 238 (1967).

[24] C. Kittel, *Introduction to Solid State Physics*, John Wiley and Sons, Inc, USA, 8th edition, 2005.

[25] G. Lutz, *Semiconductor Radiation Detectors: Device Physics*, Springer, Germany, 1st edition, 2007.

[26] L. Mihailescu, W. Gast, R. Lieder, H. Brands, and H. Jäager, Nucl. Inst. Meth. A **447**, 350 (2000).

[27] B. Bruyneel, P. Reiter, and G. Pascovici, Nucl. Inst. Meth. A **569**, 764 (2006).

[28] B. Bruyneel, P. Reiter, and G. Pascovici, Nucl. Inst. Meth. A **569**, 774 (2006).

[29] Z. He, Nucl. Inst. Meth. A **463**, 250 (2001).

[30] W. Shockley, J. Appl. Phys. **78**, 635 (1938).

[31] S. Ramo, Currents induced by electron motion, in *Proceedings of the I.R.E*, page 584, 1939.

[32] A. Pullia, F. Zocca, and G. Pascovici, IEEE Trans. Nucl. Sci. **53**, 2869 (2006).

[33] B. Bruyneel et al., Nucl. Inst. Meth. A **599**, 196 (2009).

[34] B. Bruyneel et al., Nucl. Inst. Meth. A **608**, 99 (2009).

[35] AGATA Collaboration, *AGATA GE Detector Specification*, 2006.

[36] E. Farnea, AGATA: Comparison of the A120, A180 Configurations, `http://agata.pd.infn.it/documents/simulations/comparison.html`.

[37] A. Wiens et al., Nucl. Inst. Meth. A **618**, 223 (2010).

[38] Canberra Eurisys S.A., Lingolsheim Facility, France, *Encapsulated Germanium Detector Operating Manual: Irregular AGATA Canister N A004*, 2005.

[39] Canberra Eurisys S.A., Lingolsheim Facility, France, *Encapsulated Germanium Detector Operating Manual: Irregular AGATA Canister N A006*, 2005.

[40] B. Birkenbach et al., Nucl. Instr. Meth. A **640**, 176 (2011).

[41] Ortec, Maestro, `http://www.ortec-online.com/Solutions/applications-software.aspx`, 2012.

[42] M. Dimmock et al., IEEE Trans. Nucl. Sci. **56**, 1593 (2009).

[43] L. Nelson et al., Nucl. Inst. Meth. A **573**, 153 (2007).

[44] R. Cooper et al., Nucl. Inst. Meth. A **573**, 72 (2007).

[45] Parker Motion and Control Technology Company, `http://www.parker.com/portal/site/PARKER`, 2008.

[46] S. Gros, *Characterisation of an EXOGAM Clover Germanium Detector.*, PhD thesis, University of Liverpool, 2005.

[47] A. Georgiev, W. Gast, and R. M. Leider, IEEE Trans. Nucl. Sci. **41**, 1116 (1994).

[48] D. Doering, J. Joseph, H. Yaver, and S. Zimmermann, GRETINA Digitiser Specification Manual, Technical report, 2006.

[49] C. Unsworth, *Characterisation of an Asymmetric AGATA Detector*, PhD thesis, University of Liverpool, 2011.

[50] CAEN V785 32 Channel Multievent Peak Sensing ADC, http://www.caen.it/csite/CaenProd.jsp?parent=11&idmod=37, 2011.

[51] W. D. Peterson, *The VMEbus Handbook*, VFEA International, 4th edition, 1997.

[52] MIDAS, Multi Instance Data Acquisition System, http://midas.psi.ch, 2008.

[53] J. R. Cresswell and J. Sampson, MTSort, Data Sorting Package, http://ns.ph.liv.ac.uk/MTsort-manual/MTsort.html.

[54] F. Crespi et al., Characterization of segmented hpge detectors using pulse shape comparison methods, in *NSS/MIC IEEE Conference Record*, pages 825 –827, 2010.

[55] P. Medina, C. Santos, and D. Villaume, IMTC Proceedings **3** (2004).

[56] M. Schlarb, *Simulation and Real-Time Analysis of Pulse Shapes from segmented HPGe-Detectors*, PhD thesis, Technischen Universität München, 2009.

[57] B. Bruyneel and B. Birkenbach, AGATA Detector simulation Library (ADL) v. 2.0, http://www.ikp.uni-koeln.de/research/agata/data/ReadMeADL.pdf.

[58] SIMION Version 8.1, http://simion.com, 2012.

[59] H. Lai, T. R. McJunkin, C. J. Miller, J. R. Scott, and J. R. Almirall, International Journal of Mass Spectrometry **276**, 1 (2008).

[60] B. Bruyneel, Geometry and field figures of AGATA capsule A006 derived from SIMION., private communication, 2012.

[61] M. Schlarb, Simulating AGATA Preamplifier Response and ADC, Technical report, MGS Workshop, 2005.

[62] D. von Seggern, *CRC Standard Curves and Surfaces with Mathematics*, CRC Press, Boca Raton, 2nd edition, 2007.

[63] K. Vetter et al., Nucl. Inst. Meth. A **452**, 223 (2000).